2012

Search for a heavy charged gauge boson decaying to a muon and a neutrino in 1 fb-1 of proton-proton collisions at sqrt(s) = 7 TeV using the ATLAS Detector

Alaettin Serhan Mete
Iowa State University

Search for a heavy charged gauge boson decaying to a muon and a neutrino in 1 fb^{-1} of proton-proton collisions at $\sqrt{s}$ = 7 TeV using the ATLAS Detector

by

Alaettin Serhan Mete

A dissertation submitted to the graduate faculty

in partial fulfillment of the requirements for the degree of

DOCTOR OF PHILOSOPHY

Major: High Energy Physics

Program of Study Committee:
James H. Cochran, Jr., Major Professor
Thomas E. Daniels
Sören Prell
Jianwei Qiu
Jörg Schmalian

Iowa State University

Ames, Iowa

2012

DEDICATION

to mom, dad, all my family and friends...

TABLE OF CONTENTS

LIST OF TABLES

LIST OF FIGURES

ACKNOWLEDGEMENTS

It is virtually impossible to thank everyone, who made this work possible, one by one, but I will try to stress those, without whom it would be impossible.

First of all I would like to thank my advisor, Jim Cochran, for his endless patience, help and support. I surely have learnt a lot from him, not only about physics but also about being a good researcher and collaborator. He has always given me freedom to work on any topic that interests me, which is of prime importance for a young researcher to find his scientific identity.

Secondly, I'd like to express my gratitude to David Adams. During the last year of my Ph.D. I had the privilege to lead the W' search at ATLAS alongside David. He is *the* person, from whom I learnt how a complete analysis is performed from A to Z. He has been a great mentor and friend, who was always there when I needed. I'd also like to thank everyone who has contributed to the W' search, which is one of the benchmark analyses within the ATLAS physics program, the whole ATLAS collaboration and LHC people for their great efforts.

Then there is my family and friends. I'm grateful to my dad, Ayhan, and mom, Serpil, for their endless love and support, which guided me my whole life. I'm also thankful to all my friends, especially Melis for always being there for me, Stephanie for helping me anytime I needed, Kostas for pushing my buttons all the time, Jake for teaching me how to juggle, Fabien for not leaving me alone in the office early mornings, Andy for gossiping, and also *çocuklar*: Kadri, Aytül, Candan, Gül, Tülin and all others whom I didn't have enough space to mention here.

There is always hope!

ABSTRACT

The ATLAS detector is used to search for high-mass states, such as heavy charged gauge bosons (W'), decaying to a muon and a neutrino. Results are presented based on the analysis of pp collisions at a center-of-mass energy of 7 TeV corresponding to an integrated luminosity of 1.04 fb^{-1}. No excess beyond standard model expectations is observed. A W' with sequential standard model couplings is excluded at 95% confidence level for masses below 1.98 TeV. Results from the muon channel are also combined with the electron channel to further extend the mass limit up to 2.15 TeV. This is the most stringent limit published to date.

CHAPTER 1. Introduction

The purpose of this chapter is to provide the reader with a concise background knowledge in particle physics. It begins with a brief summary of the historical background in section 1.1. Section 1.2 discusses the most fundamental contemporary model in this field, the standard model. It concludes with a discussion of possible models beyond the standard model that might give rise to new particles that are of interest of this study.

1.1 Historical Background

The main goal of particle physics is to answer the question "What is matter made of?" on the smallest scale of size. Even though it is fashionable and more romantic to refer all the way back to Democritus and other ancient Greek atomists when talking about the birth of this field, it is scientifically more accurate to mark the groundbreaking discovery by J. J. Thomson in 1897 as the start of this branch of physics as we know it today. He discovered that it was possible to bend cathode rays in the presence of strong magnetic field, which was suggesting that these rays were actually a stream of particles, known as electrons today.

In our current understanding, there are four fundamental forces in nature: *strong*, *weak*, *electromagnetic* and *gravitational*. These are summarized in order of decreasing strength* in Table 1.1. This table is mostly based on [1].

Force	**Strength**	**Theory**	**Mediator**
Strong	1	Chromodynamics	gluon
Electromagnetic	10^{-2}	Electrodynamics	photon
Weak	10^{-6}	Flavordynamics	W and Z
Gravitation	10^{-40}	Geometrodynamics	graviton

Table 1.1: Four fundamental forces in nature.

Gravitation is historically the first force that was discovered by mankind. It is *the* force responsible for the planetary motions, tides, and the fall of an apple from a treetop. The classical theory behind it is the law of universal gravitation that was first published by Sir Isaac Newton in 1687 [2]. Much later, in 1916, Albert Einstein published his theory of general relativity [3], which is a relativistic generalization of Newton's earlier findings. This is reflected in Table 1.1 as "Geometrodynamics", which is a more intuitive description. Despite being the first discovered force, a complete quantum description for gravitation is still missing today. Also it's hypothetical mediator, the graviton, still lacks experimental proof. Nonetheless, the general belief is that this force is too weak to play a significant role in particle physics.

* "Strength" of a force is strongly correlated to the nature of the source and topological conditions, therefore these numbers shouldn't be taken literally as they are provided for a relative comparison.

The theory behind electromagnetism is called electrodynamics and was first formulated by James C. Maxwell in 1861 [4]. The electromagnetic force manifests itself as the force that causes the interaction between electrically charged particles and the force that acts on a current-carrying wire in a magnetic field, both of which are summarized in the Lorentz' force law. In fact it is the most dominant force in our daily lives, holding atoms and molecules together, keeping our heart beating, letting us move our hands. Later in the 1940s the quantum theory of electrodynamics, *QED*, was perfected by Richard P. Feynman, Julian Schwinger and Sin-Itiro Tomonaga, winning them the Nobel Prize in 1965.

The first observation of β^- decay, dating back to the 1890s, puzzled the scientists because this phenomenon wouldn't fit into classical physics and remained unexplained until the 1930s. In 1934 Enrico Fermi presented the first theory that explains this observation [5], the first theory for the weak force, which was later refined by Tsung-Dao Lee and Chen N. Yang in the 1950s. In 1961 Sheldon J. Glashow showed that the electromagnetic and weak forces might be two different manifestations of a partially unified theory [6], which is known as the electroweak force today. Then in 1967 Abdus Salam and Steven Weinberg independently revised Glashow's theory allowing the masses for the W and Z particles, mediators of the weak force, arise through spontaneous symmetry breaking with the Higgs mechanism [7]. For their insights, Glashow, Salam and Weinberg were awarded the Nobel Prize in Physics in 1979. This discovery showed that it was indeed possible to decrease the number of forces to three: *gravitation*, *electroweak* and *strong*.

The theory behind the strong force is called quantum chromodynamics, *QCD*, which emerged in the mid-seventies. The first studies of strong force, however, were pioneered by Hideki Yukawa as early as 1934. This force is responsible for the integrity of the nucleus, the very reason why neutrons and protons stay together within it.

In today's particle physics, the electroweak and strong forces are explained within the so called standard model, *SM*. The next section is devoted to a brief discussion of this fundamental model.

1.2 The Standard Model

The standard model of particle physics is a quantum field theory that incorporates quantum electrodynamics and quantum chromodynamics, the theories behind electroweak and strong forces, respectively. As discussed in the previous section, it was shaped in the 20^{th} century as a result of many theoretical and experimental studies. According to this model, all matter, as we know it, is made of three kinds of elementary particles: *quarks*, *leptons* and *mediators*. Quarks and leptons come in three generations, and there are four different mediators, all of which are summarized in Table 1.2.

Generation	I	II	III		
Quarks	u	c	t	γ	
	d	s	b	g	Force
Leptons	e	μ	τ	Z	Carriers
	ν_e	ν_μ	ν_τ	W	

Table 1.2: Elementary particles of the standard model.

The first generation consists of two quarks: *up* and *down* and two leptons *electron* and *electron neutrino*. The up quark, also denoted simply as $\boldsymbol{u}$, carries an electric charge of $+2/3$, whereas the down quark, denoted as $\boldsymbol{d}$, has $-1/3$. Two up quarks and one down quark make a *proton*, with an electric charge of $+1$ and two down quarks with one up quark make a *neutron*, with neutral charge[†]. The most basic atom, the *hydrogen* atom, consists of only one proton and one electron. As the content gets richer, by adding more protons and electrons as well as neutrons, it is possible to get more complicated atoms. This means that the first generation of elementary particles make most of the visible matter: our bodies, planets, stars and so on. Therefore it is not a surprise that they were the first ones to be discovered.

[†]This is not strictly correct because our current understanding points that protons and neutrons consist of a *sea* of quarks and gluons, however this is a good enough simplification of the picture.

Strange, **s**, and bottom, **b**, quarks are the other two *down-type* quarks, whereas charm, **c**, and top, **t**, are *up-type*. Top was the last quark to be discovered, which happened in 1995, independently by the CDF and DØ collaborations [8; 9]. All up-type quarks carry an electric charge of +2/3, whereas the down-type quarks carry a charge of -1/3. These six "flavors" of quarks also have associated *anti-quarks*, which are commonly denoted by $\bar{q}$, i.e. $\bar{u}$, $\bar{d}$ etc., and differ from the quarks only in that some of their properties have equal magnitude but opposite sign. Within QCD, each quark and anti-quark also carries a so-called *color* charge, which can be treated as analogous to electric charge in QED. There are a total of three color charges: *red*, *green* and *blue*. This makes a total of 36 quarks and anti-quarks (six quark flavors, six anti-quark flavors - each carrying three different color charges).

As for the leptons, they don't carry color charge, but electric charge. Electrons, muons and tau leptons carry an electric charge of -1, whereas all neutrinos are neutral. The anti-leptons have some of their properties, such as electric charge, reversed, just like anti-quarks. This makes a total of 12 leptons and anti-leptons (six leptons and six anti-leptons). So, so far, a total of 48 elementary particles are counted.

Then there are the mediators. Within the standard model, each force is carried by a particle called the *mediator*. The mediator of the electromagnetic force is the *photon*, whereas the *gluon* mediates the strong force. Interestingly, the photon doesn't carry electric charge, even though it is the mediator for the electromagnetic force, however gluons carry color charge, and there are a total of eight of them. The weak force on the other hand has three mediators: $W^{\pm}$ and Z, where the last one has neutral electric charge. This makes a total of 12 distinct force carriers, increasing the total number of elementary particles to 60.

In the standard model, all force carriers are massless, except the W and Z. As briefly mentioned before, the mechanism that gives them their masses in the standard model is called the Higgs mechanism, which requires the existence of the so-called Higgs boson. So, in total, the standard model predicts at least 61 "elementary" particles, 36 quarks and anti-quarks, 12 leptons and anti-leptons, 12 force carriers and the Higgs boson. A detailed discussion of the mathematical formulation of the standard model is out of the scope of this work, however a

brief qualitative description will be given in the next few pages. Most of the discussion below is based on [1], in which an interested reader can find more detailed information.

1.2.1 Lagrangians and Gauge Invariance

In classical mechanics the *Lagrangian* is a function that summarizes the dynamics of a given system and can be defined as the potential energy, V, subtracted from the kinetic energy, T :

$$L = T - V. \tag{1.1}$$

It is a function of the so-called *generalized coordinates* q_i (i.e. $q_1 = x$, $q_2 = y$, $q_3 = z$) and their time derivatives $\dot{q}_i$ (i.e. $\dot{q}_1 = v_x$, $\dot{q}_2 = v_y$, $\dot{q}_3 = v_z$) and in the Lagrangian formulation, the fundamental law of motion is the Euler-Lagrange equation:

$$\frac{d}{dt}\left(\frac{\partial L}{\partial \dot{q}_i}\right) = \frac{\partial L}{\partial q_i} \qquad (i = 1, 2, 3). \tag{1.2}$$

It is a trivial exercise to show that in the cartesian coordinate system, the x component of Eq. 1.2 simplifies to the famous equation of Newton, $\mathbf{F} = m\mathbf{a}$ ($= -\nabla V$, where the scalar potential V is assumed to be *conservative*).

In classical mechanics one is often interested in the position of a *particle*, a *localized* entity in space, at a given time t, i.e. $q_i(t)$. This can be attained by solving Eq. 1.2 if the Lagrangian that describes the system is known. In relativistic field theory, a mathematical formulation of the behavior of subatomic particles, one appraises the concept of *fields* occupying a *region* of space instead. Then the goal is usually to obtain these fields, $\phi_i(q_i)$, which are functions of q_i where time is also included and treated on an equal footing with space, by solving a more generalized form of Eq. 1.2:

$$\partial_\mu\left(\frac{\partial \mathcal{L}}{\partial(\partial_\mu \phi_i)}\right) = \frac{\partial \mathcal{L}}{\partial \phi_i} \qquad (i = 1, 2, 3, \ldots), \tag{1.3}$$

where $\partial_\mu = \partial/\partial x^\mu$ with index $\mu = 0, 1, 2, 3$ and the full Lagrangian in Eq. 1.2 is replaced with the Lagrangian *density*, $\mathcal{L}$. One example of the field variables, ϕ_i, can be the temperature at each point in a room. As interesting as it sounds, historically the form of the Lagrangian

density describing a given system was often an ad-hoc guess. Now let's investigate one famous Lagrangian in a bit more detail.

The Dirac Lagrangian for a spin-$\frac{1}{2}$ field[‡] can be defined as:

$$\mathcal{L} = i(\hbar c)\bar{\psi}\gamma^{\mu}\partial_{\mu}\psi \ - \ mc^2\bar{\psi}\psi, \tag{1.4}$$

where i is the imaginary number such that $i^2 = -1$, $\hbar$ is the Planck's constant, c is the speed of light, γ^{μ} are the so-called gamma matrices (a set of special 4×4 matrices) and ψ is the spinor field with its adjoint spinor $\bar{\psi}$. A rigorous understanding of all these terms are out of the scope of this discussion, but if one applies Eq. 1.3 for this particular Lagrangian density, it yields:

$$\frac{\partial\mathcal{L}}{\partial(\partial_{\mu}\bar{\psi})} = 0 \qquad \frac{\partial\mathcal{L}}{\partial\bar{\psi}} = i(\hbar c)\gamma^{\mu}\partial_{\mu}\psi \ - \ mc^2\psi, \tag{1.5}$$

hence,

$$[i(\hbar c)\gamma^{\mu}\partial_{\mu} \ - \ mc^2]\psi = 0. \tag{1.6}$$

This is the famous Dirac equation that describes a particle of spin-$\frac{1}{2}$ with mass m in quantum field theory. It is also possible to obtain a similar equation for the adjoint spinor through a similar exercise.

Then assume the person wants to make a simple transformation as:

$$\psi \rightarrow e^{i\theta}\psi, \tag{1.7}$$

where e is the exponential function, and θ is any *real* number. It can easily be shown that the Lagrangian density defined in Eq. 1.4 remains unchanged since $\bar{\psi} \rightarrow e^{-i\theta}\bar{\psi}$ hence the exponential terms in $\bar{\psi}\psi$ cancel out. This is called the *global gauge invariance*. However this wouldn't hold if θ was a function of x, i.e. $\theta(x)$, due to the derivative term. This means that

[‡]Spin can be defined to be the angular momentum of a particle in its own rest frame. It is one of the *quantum numbers*, which describe values of conserved quantities in the dynamics of the quantum system. One example for a spin-$\frac{1}{2}$ particle is the ever famous electron.

the Dirac Lagrangian destiny as defined in Eq. 1.4 does not have *local gauge invariance*. A natural question at this point is : "Why is it important to have local gauge invariance?". For the time being, let's say this is desired just for the sake of it, however, the answer will be apparent soon enough. It is possible to achieve this goal by introducing an additional term to the original Lagrangian that cancels the extra piece that comes from the derivative as:

$$\mathcal{L} \rightarrow \mathcal{L} + q\bar{\psi}\gamma^{\mu}\psi\partial_{\mu}\lambda, \tag{1.8}$$

where q is the charge of the particle and $\lambda(x)$ is defined as:

$$\lambda(x) = -\frac{\hbar c}{q}\theta(x), \tag{1.9}$$

only for convenience. This means that it is possible to define a "new" Dirac Lagrangian density that is indeed invariant as:

$$\mathcal{L} = i(\hbar c)\bar{\psi}\gamma^{\mu}\partial_{\mu}\psi \ - \ mc^2\bar{\psi}\psi \ - \ q\bar{\psi}\gamma^{\mu}\psi \ A_{\mu}, \tag{1.10}$$

by introducing a "new" vector gauge field, A_{μ}, that transforms as:

$$A_{\mu} \rightarrow A_{\mu} + \partial_{\mu}\lambda. \tag{1.11}$$

In order to complete 1.10 one needs to add a free term for the new gauge field, A_{μ}, and for this let's use:

$$\frac{-1}{16\pi}F^{\mu\nu}F_{\mu\nu} + \frac{1}{8\pi}\left(\frac{m_A c}{\hbar}\right)^2 A^{\mu}A_{\mu} \tag{1.12}$$

where $F^{\mu\nu}$ is the *electromagnetic field tensor*, defined as $F^{\mu\nu} = \partial^{\mu}A^{\nu} - \partial^{\nu}A^{\mu}$ and m_A is the mass of the new field. Of course this choice is merely a coincidence. Eq 1.12 is known as the Proca Lagrangian, and it describes the electromagnetic field of a physical system in Maxwell's theory of electromagnetism. This is why it's chosen. The only issue with this choice is that the last term in Eq. 1.12 is not invariant under transformation defined in Eq. 1.11, unless one

specifically imposes $m_A = 0$. This means that the new gauge filed has to be *massless*. Then combining Eq. 1.10 with Eq. 1.12 and setting $m_A = 0$, one gets:

$$\mathcal{L} = [i(\hbar c)\bar{\psi}\gamma^{\mu}\partial_{\mu}\psi \ - \ mc^2\bar{\psi}\psi] \ + \left[\frac{-1}{16\pi}F^{\mu\nu}F_{\mu\nu}\right] \ - \ [q\bar{\psi}\gamma^{\mu}\psi \ A_{\mu}]. \tag{1.13}$$

In this last equation, the "new" field, A_μ, is actually nothing but the electromagnetic potential, with the last two terms being the so-called Maxwell Lagrangian. Eq. 1.13 not only generates all of the electrodynamics (!) but also explains the currents generated by the Dirac particles and all these are obtained by imposing local gauge invariance on the Dirac Lagrangian density defined in Eq. 1.4 and an educated guess for the extra terms needed. Surely this has an underlying importance.

In principal if a Lagrangian density has global gauge invariance, it is possible to impose local gauge invariance by adding a vector field to the partial derivatives, ∂_μ, to get the so-called *covariant derivatives*, $\mathcal{D}_\mu$, defined as:

$$\mathcal{D}_{\mu} = \partial_{\mu} + i\frac{q}{\hbar c}A_{\mu}. \tag{1.14}$$

Now let's investigate the importance of gauge invariance. A *gauge theory* in particle physics is a special type of *field theory* in which the Lagrangian is invariant under a continuous group of *local* transformations (called *gauge invariance*). The term *gauge* refers to redundant degrees of freedom in the Lagrangian. In the above example, it is the electromagnetic potential, A_μ, that is added by hand to make the initial Lagrangian invariant under the appropriate gauge transformation. Indeed it is the gauge field of quantum electrodynamics, QED, which is an abelian[§] gauge theory with the symmetry group $U(1)$. Furthermore, when such a theory is quantized, the *quanta* of the gauge fields are called *gauge bosons*. In the case of QED this is nothing but the photon.

Gauge theories are in the heart of particle physics. The standard model is a non-abelian gauge theory with the symmetry group $U(1) \times SU(2) \times SU(3)$ and has a total of twelve gauge bosons: the photon, three weak bosons and eight gluons (introduced as mediators in Table 1.1,

[§]An *abelian group*, also called *commutative group*, is a group in which for all elements a and b, the relation $a * b = b * a$ holds.

and force carriers in Table 1.2). But there is an interesting point here. Remember that the mass term in the Proca Lagrangian in Eq. 1.12 had to be set to zero to ensure local gauge invariance, which is the case for the carriers of electromagnetic and strong forces. However, this is certainly not the case for the weak force carriers. Actually, the principle of local gauge invariance works very neatly for the electromagnetic and strong forces, but surely the weak interactions need more than what was discussed above. This brings the discussion to *spontaneous symmetry breaking* and the *Higgs mechanism*.

1.2.2 Spontaneous Symmetry Breaking and the Higgs Mechanism

Let's investigate yet another Lagrangian: the Klein-Gordon Lagrangian that describes a scalar field, ϕ:

$$\mathcal{L} = \frac{1}{2}(\partial_\mu \phi)(\partial^\mu \phi) - \frac{1}{2}\left(\frac{mc}{\hbar}\right)^2 \phi^2. \tag{1.15}$$

Applying the Euler-Lagrange equation to Eq. 1.15 yields:

$$\partial_\mu \partial^\mu \phi + \left(\frac{mc}{\hbar}\right)^2 \phi = 0. \tag{1.16}$$

This is the Klein-Gordon equation describing a spin-0, i.e. *scalar*, particle with mass m. As can be seen from Eq. 1.15, the term of *second order* in the appropriate field can, in general, be identified as the "mass" term of the Lagrangian. Let's investigate a Lagrangian that is slightly different:

$$\mathcal{L} = \frac{1}{2}(\partial_\mu \phi)(\partial^\mu \phi) + \frac{1}{2}\mu^2 \phi^2 - \frac{1}{4}\lambda^2 \phi^4, \tag{1.17}$$

where μ and λ are two real constants. At first, the second term seems like the mass term, but a quick comparison between Eq. 1.15 and Eq. 1.17 reveals a subtle point. The signs of the second terms are opposite, which means that if the second term in Eq. 1.17 was to be the mass term, it would be *imaginary*! This, of course, is not physical and raises the question: How can one find the mass term for such a Lagrangian?

Recall the conventional definition of the Lagrangian in Eq. 1.1. For $T(\phi) = \frac{1}{2}(\partial_\mu \phi)(\partial^\mu \phi)$, the potential $V(\phi)$ turns out to be:

$$V(\phi) = -\frac{1}{2}\mu^2\phi^2 + \frac{1}{4}\lambda^2\phi^4, \tag{1.18}$$

with the minimum occurring at:

$$\phi = \pm\frac{\mu}{\lambda}. \tag{1.19}$$

This actually separates Eq. 1.17 from all the other Lagrangians that have been considered so far, for which the ground states (where V is minimum) were always $\phi = 0$. At this point, let's define a new field, η, so that when Eq. 1.17 is re-written in terms of it, the ground state is obtained at $\eta = 0$:

$$\eta = \phi \pm \frac{\mu}{\lambda} \tag{1.20}$$

Then Eq. 1.17 becomes:

$$\mathcal{L} = \frac{1}{2}(\partial_\mu \eta)(\partial^\mu \eta) - \mu^2\eta^2 \pm \mu\lambda\eta^3 - \frac{1}{4}\lambda^2\eta^4 + \frac{1}{4}\left(\frac{\mu^2}{\lambda}\right)^2. \tag{1.21}$$

Now as can be seen, the second order term has the correct sign, and the mass of the new field is:

$$m = \sqrt{2}\frac{\mu\hbar}{c}. \tag{1.22}$$

This last bit of mathematical gymnastics doesn't change any physical property of the system, but merely puts the Lagrangian in a form where one can identify the mass term with ease. The bottom line of this exercise is that one can identify the mass term in a Lagrangian by first finding the ground state, re-expressing it as a function of the deviation, η, from this minimum, expanding it in terms of η and locating the coefficient of the η^2 term.

One interesting difference between Eq. 1.17 and Eq. 1.21 is that the former is *even* in ϕ, it doesn't change for $\phi \to -\phi$, however the latter is not even in η. This means when

Eq. 1.17 is re-written in terms of the new field, it's symmetry is "broken". The reason is as follows. Figure 1.1 shows the potential that is defined in Eq. 1.18, which is also known as the "double-well" potential, for $\mu = 2$ and $\lambda = 2$ (arbitrarily chosen for demonstration). As found analytically in Eq. 1.19, it has two minima, $\phi = \pm 1$.

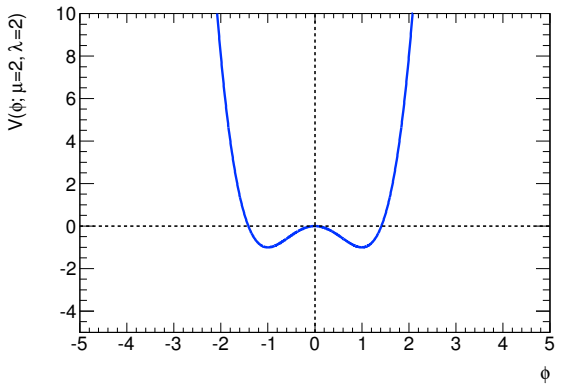

Figure 1.1: Double well potential as defined in Eq. 1.18 for $\mu = 2$ and $\lambda = 2$.

In order to express the Lagrangian in terms of η, with a minimum at $\eta = 0$, one has to choose either of these solutions, $+1$ or -1 and doing so spoils the symmetry. This phenomenon is called the *spontaneous symmetry breaking*. It is spontaneous because there is no *external* agent that causes this. Actually, the concept of symmetry breaking is not very strange to daily life. For example, when one throws a ball up in the air, it comes down, however it doesn't go back to right once it's thrown left, or vice versa. So, on earth, up-down and left-right symmetry is broken. However there is an external agent that causes this, gravity. Therefore it is not spontaneous in that sense.

To take one step closer to the Higgs mechanism, let's define a complex field as:

$$\phi = \phi_1 + i\phi_2, \tag{1.23}$$

where ϕ_1 and ϕ_2 are two real, scalar fields satisfying:

$$\phi^*\phi = (\phi_1 - i\phi_2)(\phi_1 + i\phi_2) = \phi_1^2 + \phi_2^2. \tag{1.24}$$

Then a 2 dimensional version of Eq. 1.17 can be written as:

$$\mathcal{L} = \frac{1}{2}(\partial_\mu \phi)^*(\partial^\mu \phi) + \frac{1}{2}\mu^2(\phi^*\phi) - \frac{1}{4}\lambda^2(\phi^*\phi)^2, \tag{1.25}$$

yielding the potential V:

$$\begin{aligned} V(\phi, \phi^*) &= -\frac{1}{2}\mu^2(\phi^*\phi) + \frac{1}{4}\lambda^2(\phi^*\phi)^2 \\ &= -\frac{1}{2}\mu^2(\phi_1^2 + \phi_2^2) + \frac{1}{4}\lambda^2(\phi_1^2 + \phi_2^2)^2, \end{aligned} \tag{1.26}$$

where the second line is obtained via Eq. 1.24. The ground state for this potential is then nothing but a circle in the $\phi_1 - \phi_2$ plane given by the formula:

$$\phi_{1,\min}^2 + \phi_{2,\min}^2 = \left(\frac{\mu}{\lambda}\right)^2 \tag{1.27}$$

with one possible solution as:

$$\phi_{1,\min} = \frac{\mu}{\lambda} \qquad \phi_{2,\min} = 0 \tag{1.28}$$

It is also evident that Eq. 1.25 has global invariance under the transformation $\phi \to e^{i\theta}\phi$, however, it doesn't have local gauge invariance. In order to impose this, let's make the substitution of $\partial_\mu \to \mathcal{D}_\mu$, with $\mathcal{D}_\mu$ as defined in Eq. 1.14. Then one gets:

$$\mathcal{L} = \frac{1}{2}(\mathcal{D}_\mu \phi)^*(\mathcal{D}^\mu \phi) + \frac{1}{2}\mu^2(\phi^*\phi) - \frac{1}{4}\lambda^2(\phi^*\phi)^2 - \frac{1}{16\pi}F^{\mu\nu}F_{\mu\nu}. \tag{1.29}$$

Now, as we did in Eq. 1.21, let's expand Eq. 1.29 about the ground state defined in Eq. 1.28. This means re-writing Eq. 1.29 in terms of η and ξ, where they are defined as:

$$\eta = \phi_1 - \frac{\mu}{\lambda} \qquad \xi = \phi_2. \tag{1.30}$$

Let's also pick a *particular gauge* in which the re-written Lagrangian will further be simplified and easier to put into context as:

$$\begin{aligned} \phi \rightarrow \phi' &= e^{i\theta}\phi = (cos(\theta) + isin(\theta))(\phi_1 + \phi_2) \\ &= [cos(\theta)\phi_1 - sin(\theta)\phi_2)] + i\left[sin(\theta)\phi_1 + cos(\theta)\phi_2\right]. \end{aligned} \tag{1.31}$$

Picking a particular θ so that ϕ' is real can be achieved by setting $i\left[sin(\theta)\phi_1 + cos(\theta)\phi_2\right]$ to zero. This implies that $\theta = -tan^{-1}\left(\phi_2/\phi_1\right)$, hence $\phi'_2 = 0$. Then Eq. 1.29 becomes:

$$\begin{aligned} \mathcal{L} &= \left[\frac{1}{2}(\partial_\mu\eta)(\partial^\mu\eta) - \mu^2\eta^2\right] + \left[-\frac{1}{16\pi}F^{\mu\nu}F_{\mu\nu} + \frac{1}{2}\left(\frac{q}{\hbar c}\frac{\mu}{\lambda}\right)^2 A_\mu A^\mu\right] \\ &+ \left[\frac{\mu}{\lambda}\left(\frac{q}{\hbar c}\right)^2 \eta(A_\mu A^\mu) + \frac{1}{2}\left(\frac{q}{\hbar c}\right)^2 \eta^2(A_\mu A^\mu) - \lambda\mu\eta^3 - \frac{1}{4}\lambda^2\eta^4\right] \\ &+ \left(\frac{\mu^2}{2\lambda}\right)^2. \end{aligned} \tag{1.32}$$

Now, the first line yields a scalar field, η, with the same mass given in Eq. 1.22 and a massive vector field A_μ. The prior is nothing but the famous *Higgs particle* and within the context of weak interactions, the latter gives birth to the massive gauge bosons, W and Z.

The second line holds information regarding the interactions between η and A_μ particles. These are often visualized pictorially using the so-called *Feynman diagrams*. For example the second term in line two is:

$$\frac{1}{2}\left(\frac{q}{\hbar c}\right)^2 \eta^2(A_\mu A^\mu). \tag{1.33}$$

The Feynman diagram for this interaction is shown in Fig. 1.2, and the inline representation of it can be made as $\eta + \eta \rightarrow A + A$. Eq. 1.33 is also called the *vertex factor*, since it carries information regarding the interaction vertex and can be used to define an *amplitute*, $\mathcal{M}$, which then can be used to calculate the *cross section*, σ, for the given process. The cross section is simply a measure for the probability of a given process to occur, and it is often expressed in units of *area*, mostly due to historical reasons dating back to fixed target experiments. A more

detailed discussion of these concepts is out of the scope of this study, but an interested reader can find more details in [1].

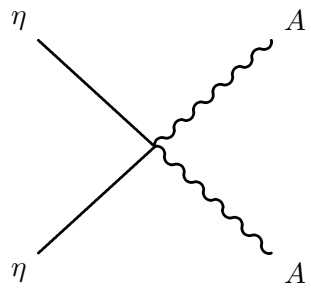

Figure 1.2: Feynman diagrams for the interaction defined in Eq. 1.33.

The last few pages demonstrated that it's possible to explain the existence of massive gauge bosons through *spontaneous symmetry breaking* and *local gauge invariance* in the existence of a Higgs boson. Actually, within the standard model, all elementary particles are massless, and it's their interactions with this hypothetical Higgs particle that creates their masses. Of course the reality is more complicated than what is discussed here. For example, the potential used in Eq. 1.26 is only educational and the "real" form of it, if it exists at all, is currently unknown. Moreover, the existence of the Higgs boson still lacks experimental confirmation. Although not discussed here, the standard model lacks neutrino masses. Therefore, it fails to explain the experimental observation of the so called neutrino oscillations. This, and other reasons hint that, even though the standard model is very successful in explaining most of the experimental observations in elementary particle physics so far, and sometimes with breath-taking precision, it is not the ultimate theory of particle physics. Therefore, it is very important to search for new physics, not only those explained by the standard model such as the Higgs but also anything beyond it, in order to head towards some answers to today's open questions in this field. The next section is devoted to the discussion of such possible extensions to the standard model that predict the existence of heavy charged gauge bosons that form the basis of the search presented in this work.

1.3 W' Models

The existence of heavy ($m_{\mathrm{V}} \gg m_{\mathrm{W/Z}}$) gauge bosons $V^{\pm}$, V^{0} is predicted by many extensions to the standard model. In this work the focus will be given to the charged ones, i.e. $V^{\pm}$, which are also commonly referred to as W'. These particles, if they exist, can be observed in the usual leptonic channels $V^{\pm} \to \ell^{\pm}\nu$ as well as $V^{\pm} \to \ell^{\pm}\nu jj$ arising from $V^{\pm} \to W^{\pm}Z$. However the most favored channel is often based on the specific model under consideration.

In some models, the leptonic mode can be very strongly suppressed or even forbidden. Among those is, for example, the right-handed charged bosons $W_{\mathrm{R}}^{\pm}$ as discussed in [10]. In this model, the leptonic channel is suppressed when the right-handed neutrino ν_{R} is too heavy for the decay $W_{\mathrm{R}} \to e\nu_{\mathrm{R}}$ to occur. Models with a strongly interacting Higgs sector, i.e. as discussed in [11], might also favor the WZ decay mode. In these models, $V^{\pm}$ bosons may be considered as resonance in the WZ channel, hence resulting in a naturally large branching fraction.

On the other hand, there are other models that favor the leptonic channels, such as the extended gauge models, i.e. [12]. In the simplest approach, the extended gauge models can be obtained by introducing extra groups to the already existing ones, i.e. the standard model. Then following a similar procedure as discussed in the previous sections, the "new" heavy gauge bosons can be obtained through the concept of symmetry breaking. The particular model considered here is the so-called sequential standard model (SSM), i.e. the extended gauge model in [12] with the W' couplings to WZ set to zero. In this model, the coupling of the W' to fermions is the same as the standard model W with the main production mechanism in pp collisions being the quark annihilation process with the associated Feynman diagram given in Fig. 1.3.

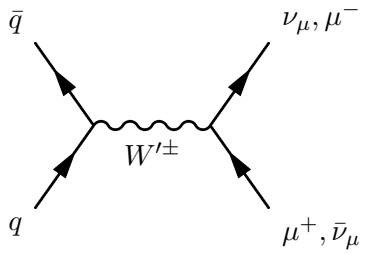

Figure 1.3: Tree level Feynman diagrams for $W'^{+} \to \mu^{+}\nu_\mu$ and $W'^{-} \to \mu^{-}\bar{\nu}_\mu$.

The decay width for $W' \to \ell\nu$ in this formalism can be written as:

$$\Gamma(W' \to \ell\nu) = \frac{\alpha}{12}\frac{M_{W'}}{sin^2\theta_W}, \tag{1.34}$$

where $\alpha = \frac{1}{128}$, $sin^2\theta_W = 0.23$, $M_{W'}$ is the mass of the W' and $\ell = e, \mu, \tau$.

As can be seen in Eq. 1.34, the decay width is linear in W' mass, with a leptonic branching fraction of 8.5%. The branching fraction for $W' \to q\bar{q}$ is actually three times larger than that for leptons, however this channel suffers from significant multi-jet background, whereas the leptonic channel is cleaner and has better signal to background separation. This is the main reason why SSM W' is most easily searched for in the leptonic channel, as has been done in this study. Fig. 1.4 shows the leading order production cross section for SSM W' times branching fraction for the muon decay channel, σB, in pp collisions at $\sqrt{s} = 7$ TeV, signifying a possible discovery could be made for masses up to about 2 TeV with the amount of data considered in this study.

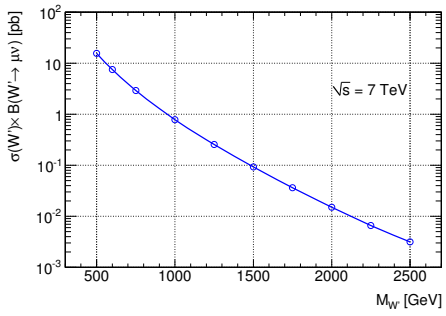

Figure 1.4: Leading Order (LO) W' production cross section times the branching fraction to a muon and a neutrino.

CHAPTER 2. Experimental Setup

This chapter is devoted to the discussion of the experimental setup and the data taking conditions. It begins with a brief introduction to CERN and the Large Hadron Collider in section 2.1, which is followed by a somewhat detailed discussion of the ATLAS experiment and detector in section 2.2. Section 2.3 will conclude the chapter with a summary of the data taking conditions that are used in the current study.

2.1 CERN and the LHC

2.1.1 CERN

The European Organization for Nuclear Research, known as *CERN*, was founded in 1954 on the Franco-Swiss border near Geneva and is currently the world's largest particle physics laboratory. The laboratory's scientific and technical staff designs and builds particle accelerators and ensures their smooth operation. They also help prepare, run, analyze and interpret the data from complex scientific experiments. Some 8000 visiting scientists, half of the world's particle physicists, come to CERN for their research. They represent 580 universities and 85 nationalities [16].

2.1.2 The LHC

The Large Hadron Collider (*LHC*) is located on the Franco-Swiss border near Geneva and is currently the world's largest and most powerful particle accelerator [17]. It is the latest addition to CERN's accelerator complex, as shown in Fig. 2.1, and mainly consists of 27 km (17 mi) ring, as much as 175 m (574 ft) beneath the surface, of superconducting magnets with a number of accelerating structures to boost the energy of the particles along the way.

The LHC is designed for two types of collisions: proton-proton and lead-lead, hence it carries the word *hadron* in it's name. The nominal energy for protons is 7 TeV with an instantaneous luminosity of 10^{34} cm^{-2} s^{-1} and the energy for lead ions is 2.76 TeV/nucleon. It uses 1232 main dipole magnets that operate at 1.9 K (-271.3 ^{o}C) to bend the particles around the ring. The protons are injected into the ring in groups called *bunches*, where each bunch has $\approx 10^{11}$ protons and the machine can hold up to 2808 bunches per beam, circulate them and collide them at four interaction points that host the experiments: ATLAS, ALICE, CMS and LHCb, as shown in Fig. 2.1.

ALICE, *A Large Ion Collider Experiment*, and LHCb, *Large Hadron Collider beauty*, are specific purpose detectors that are designed to study ion collisions and b-quark production, respectively, whereas ATLAS, *A Toroidal Large hadron collider ApparatuS*, and CMS, *Compact*

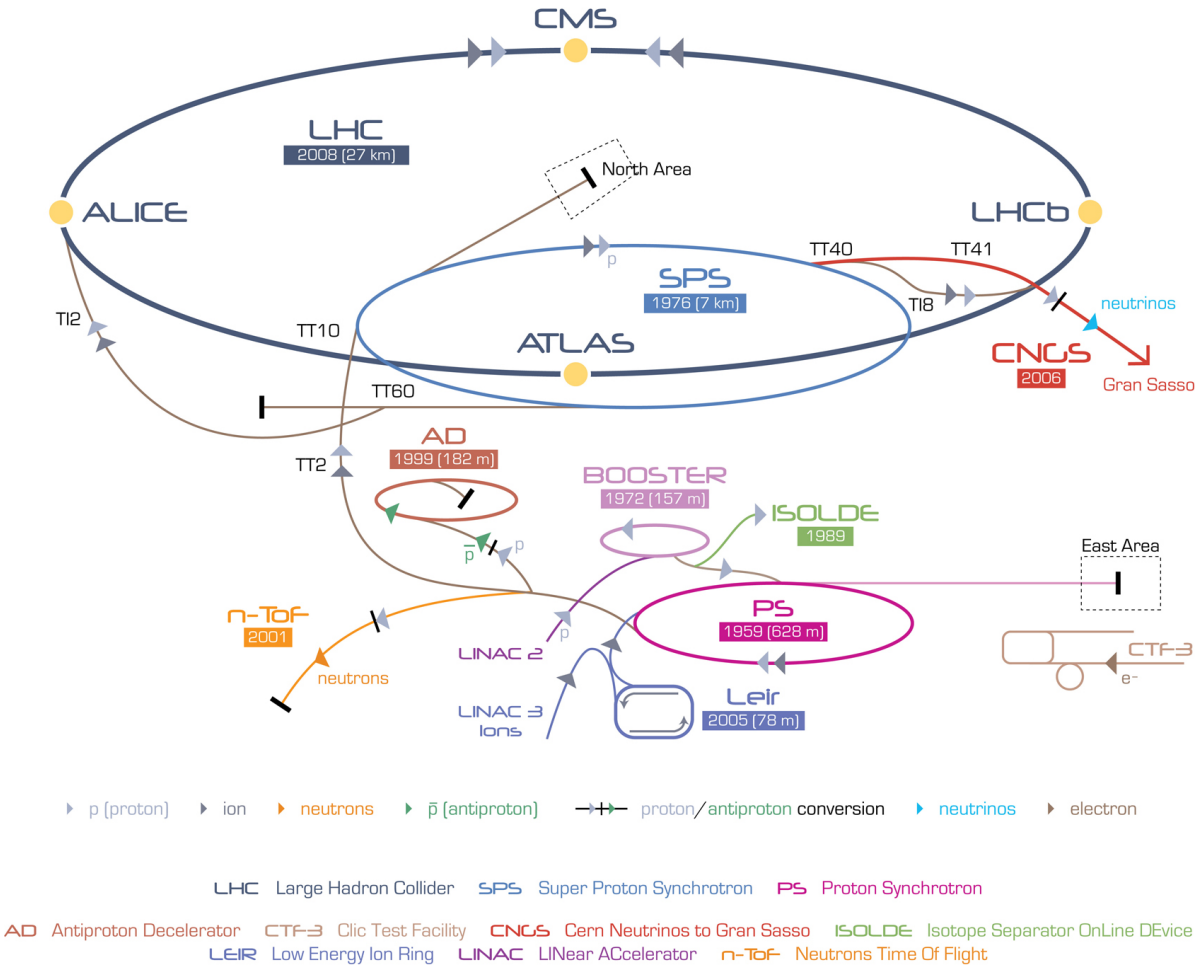

Figure 2.1: CERN accelerator complex

Muon Solenoid, are general purpose detectors designed to cover the widest possible range of physics at the LHC.

2.2 The ATLAS Experiment and Detector

The ATLAS collaboration consists of about 3000 physicists and engineers from 165 institutions in 35 countries and its aim is to search for new discoveries in the head-on collisions of protons at the LHC and learn about the basic forces that have shaped the Universe since the beginning of time and that will determine its fate [18].

The ATLAS detector is the world's largest particle detector ever built. It is 44 m long and 25 m in diameter, weighing about 7,000 tonnes (see Fig. 2.2), which makes it about half as

big as the Notre Dame Cathedral in Paris and weigh the same as the Eiffel Tower. It consists of three main parts: inner detector, calorimeter and the muon spectrometer.

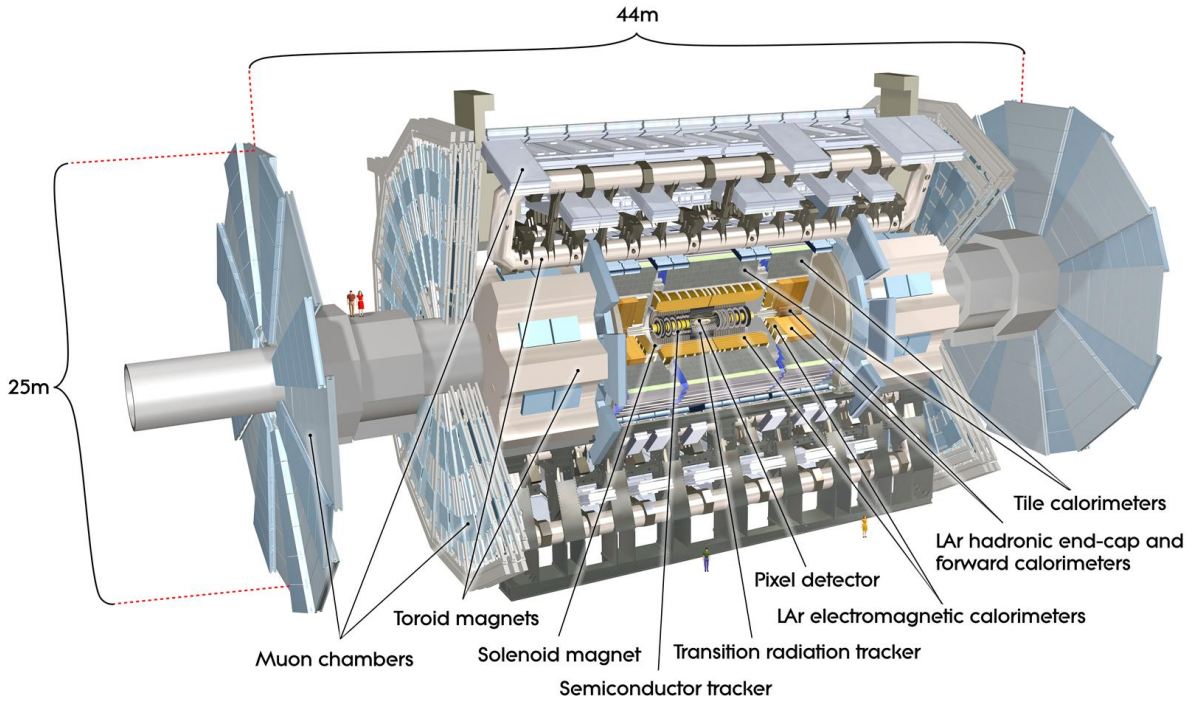

Figure 2.2: The ATLAS detector

2.2.1 Inner Detector

The inner detector (*ID*) is designed for vertex* finding and measuring the momenta of charged particles emerging from the collisions. To meet the measurement requirements imposed by the benchmark physics processes, it is designed to have pixel and silicon microstrip (*SCT*) trackers, used in conjunction with the straw tubes of the transition radiation tracker (*TRT*) [19]. A computer generated image of the inner detector can be seen in Fig. 2.3, which shows the layout of the different sub-systems. The pixel detector, the inner-most part of the ID, is composed of three layers in the barrel and three disks on each side called the *end-caps*. Just outside the pixel detector is the SCT, which has four layers in the barrel and nine disks on

*Vertices are the positions of interesting physics interactions, such as proton collisions and particle decays.

each end-cap. The outer-most part of the ID, the TRT, encloses these and is immersed in a 2 T magnetic field, generated by the central solenoid magnet, which extends over a length of 5.3 m with a diameter of 2.5 m. Fig. 2.4 shows a detailed scheme of the inner detector, and summarizes its main parameters.

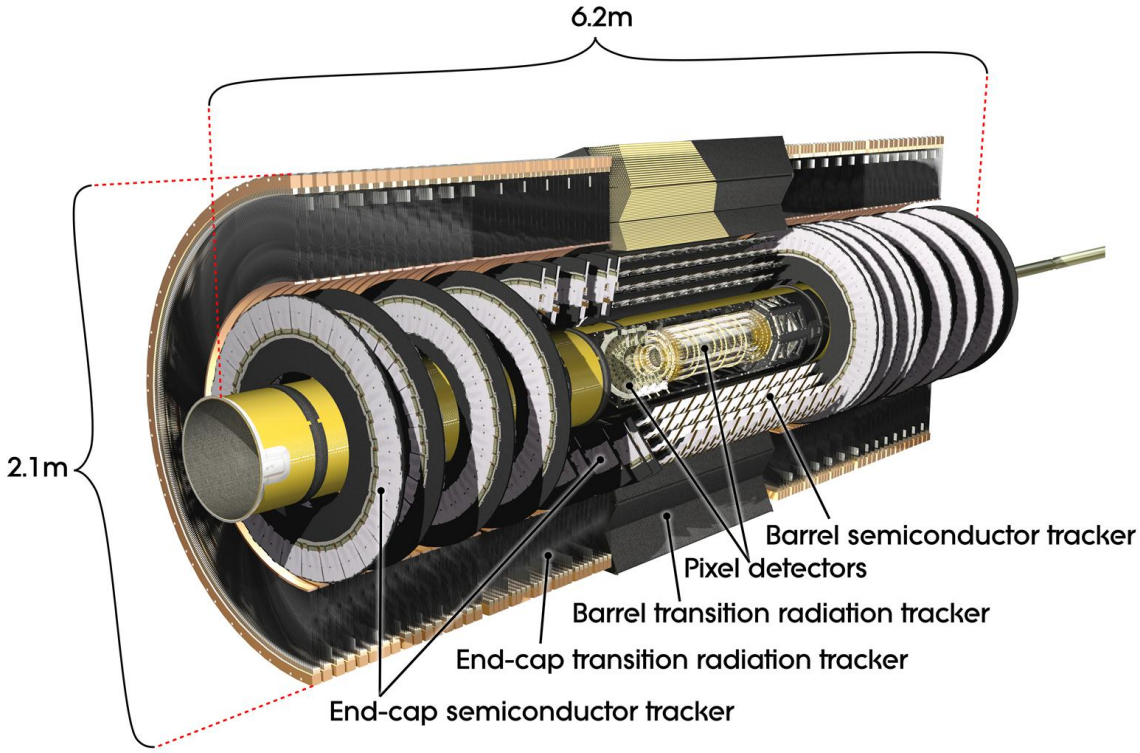

Figure 2.3: Cut-away view of the inner detector

The precision detectors (pixel and SCT) have a coverage of $|\eta^{\dagger}| < 2.5$, whereas the TRT coverage goes only up to $|\eta| = 2.0$. Intrinsic measurement accuracies and mechanical alignment tolerances for the inner detector sub-systems are summarized in Table 2.1.

The ID measures the momenta of charged particles in the following way. The trajectory of a charged particle that is created during a collision is bent due to the existence of the magnetic field as it travels through the system, and creates the so called *hits* on the layers that fall on its trajectory. Each such hit, also called a *space-point*, is fed into a complicated set

[†]Pseudorapidity, denoted by η, is a spatial coordinate describing the angle of a particle relative to the beam axis with the relation $\eta = -ln[tan(\frac{\theta}{2})]$, where θ is the angle between the particle's momentum and the beam axis.

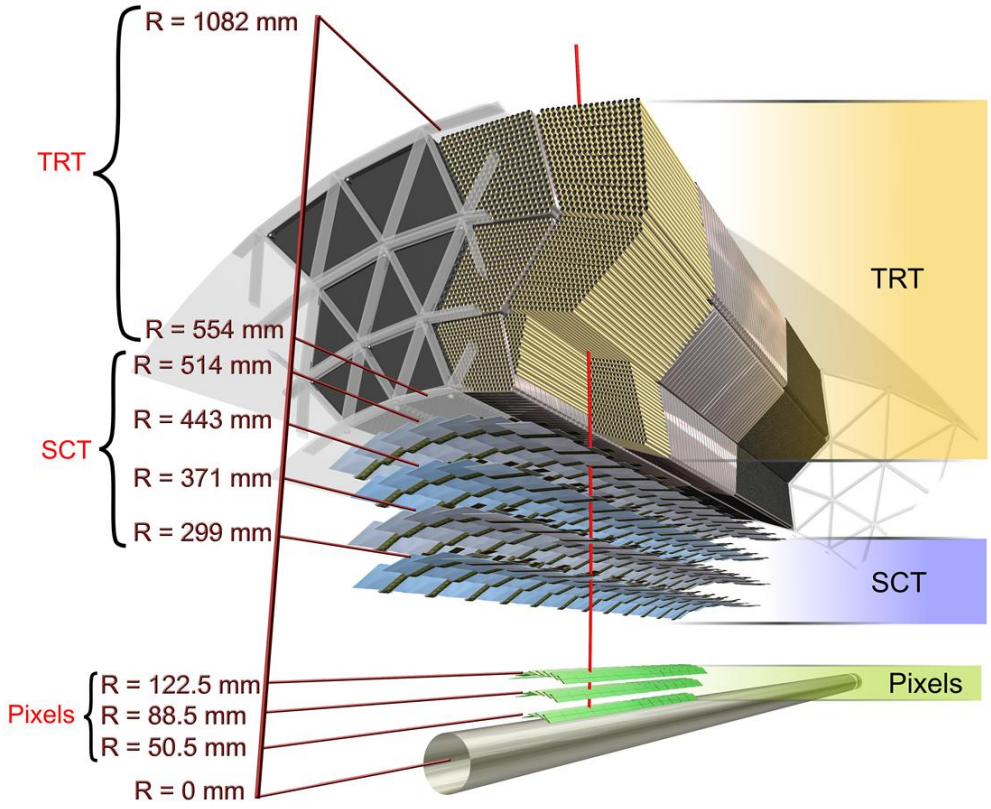

Figure 2.4: Scheme of the ATLAS inner detector barrel being crossed by one high-momentum particle (red line).

of reconstruction algorithms [20], which builds a *track* for that particle. There are five main parameters for the tracks, these are: inverse momentum (q/p), azimuthal angle (ϕ), polar angle (θ), transverse impact parameter (d_0) and longitudinal impact parameter (z_0). The resolution of a track parameter X can be expressed as a function of transverse momentum, $\mathrm{p_T}$, as:

$$\sigma_X(p_T) = \sigma_X(\infty)(1 \oplus p_X/p_T), \tag{2.1}$$

where $\sigma_X(\infty)$ is the asymptotic resolution of parameter X at infinite momentum, p_X is the constant representing the value of $\mathrm{p_T}$ where the contribution from the intrinsic resolution

Item	Intrinsic Accuracy (μm)	Allignment Tolerances (μm)		
		Radial (R)	Axial (z)	Azimuth ($R-\phi$)
Pixel				
Layer-0	10 ($R-\phi$) 115(z)	10	20	7
Layer-1&2	10 ($R-\phi$) 115(z)	20	20	7
Disks	10 ($R-\phi$) 115(z)	20	100	7
SCT				
Barrel	17 ($R-\phi$) 580(z)	100	50	12
Disks	17 ($R-\phi$) 580(z)	50	200	12
TRT				
All	130			30

Table 2.1: Intrinsic measurement accuracies and mechanical alignment tolerances for the inner detector sub-systems [19].

equals to the multiple-scattering term in the equation for parameter X. Table 2.2 summarizes the expected resolutions for the five main track parameters mentioned before in two different η regions, corresponding to barrel and end-cap. A more detailed discussion can be found in [19].

Track parameter	$0.25 < \|\eta\| < 0.50$		$1.50 < \|\eta\| < 1.75$	
	$\sigma_X(\infty)$	p_X [GeV]	$\sigma_X(\infty)$	p_X [GeV]
Inverse transverse momentum (q/p_T)	0.34 TeV^{-1}	44	0.41 TeV^{-1}	80
Azimuthal angle (ϕ)	70 μrad	39	92 μrad	49
Polar angle ($cot(\theta)$)	0.7×10^{-3}	5	1.2×10^{-3}	10
Transverse impact parameter (d_0)	10 μrad	14	12 μrad	20
Longitudinal impact parameter ($z_0 \times sin(\theta)$)	91 μrad	2.3	71 μrad	3.7

Table 2.2: Expected track-parameter resolutions at infinite transverse momentum, $\sigma_X(\infty)$, and transverse momentum, p_X, at which the multiple-scattering contribution equals to that from the detector resoultion. Momentum and angular resolutions are given for muons, and the impact parameter resolutions are given for pions.

Owing to less dead material, barrel track resolution values are better than the end-cap values as can be seen in Table 2.2. By design the charge of muons and electrons can be measured in the *ID* over the complete acceptance up to 1 TeV with misidentification probabilities on average of a few percent. In the barrel region, the reconstruction efficiency for muons with $p_T > 1$ GeV is above 98%, where this number rises to $> 99.5\%$ for high-p_T muons thanks

to the Muon Spectrometer, which will be discussed later. Electrons and pions, on the other hand, suffer from material effects resulting in reconstruction efficiencies between $70\% - 95\%$ for tracks around 5 GeV.

2.2.2 Calorimeter

The ATLAS calorimeter system is composed of two main parts: the electromagnetic (EM) and the hadronic ($HCAL$) calorimeters. The former is designed to make precision energy measurements for particles that interact mainly via electromagnetic force, such as electrons and photons, whereas the latter is designed for particles that interact strongly. The calorimeter system is divided into three cryogenic parts as one barrel and two end-caps. Liquid Argon (LAr) is used in all three parts for the EM calorimeter. The barrel part of the hadronic calorimeter consists of scintillating tiles, and hence bears the name Tile Calorimeter ($TileCal$). They are also used in the outer rings of the end-caps, whereas in the inner ring and the forward region LAr is used. A computer generated overview of the ATLAS calorimeter system can be seen in Fig. 2.5.

The ATLAS electromagnetic calorimeter is able to identify efficiently electrons and photons within a large energy range ($5\ \text{GeV} - 5\ \text{TeV}$) and measure their energies with a linearity[‡] better than 0.5%. It uses lead absorbers and liquid argon as the active material, is designed to be projective in η, and covers a range of $|\eta| < 3.2$ (barrel : $|\eta| < 1.475$, end-caps : $1.375 < |\eta| < 3.2$) [21]. However due to the fact that the ID coverage only goes up to $|\eta| = 2.5$, the precision measurements are limited to this region. The EM calorimeter is designed in a unique accordion shape in order to eliminate azimuthal cracks, and has a total thickness of greater than 22 radiation lengths (X_0) in the barrel region and $24X_0$ in the end-caps. It is composed of three layers, generally referred to as "front" (or "strips"), "middle" and "back". There is also a pre-sampler, covering $|\eta| < 1.8$, to account and correct for the energy loss upstream of the calorimeter. The granularity of these layers at $\eta = 0$ and general details can be seen in Fig 2.6.

[‡]The linearity is the ratio between the fitted mean value and the true particle energy.

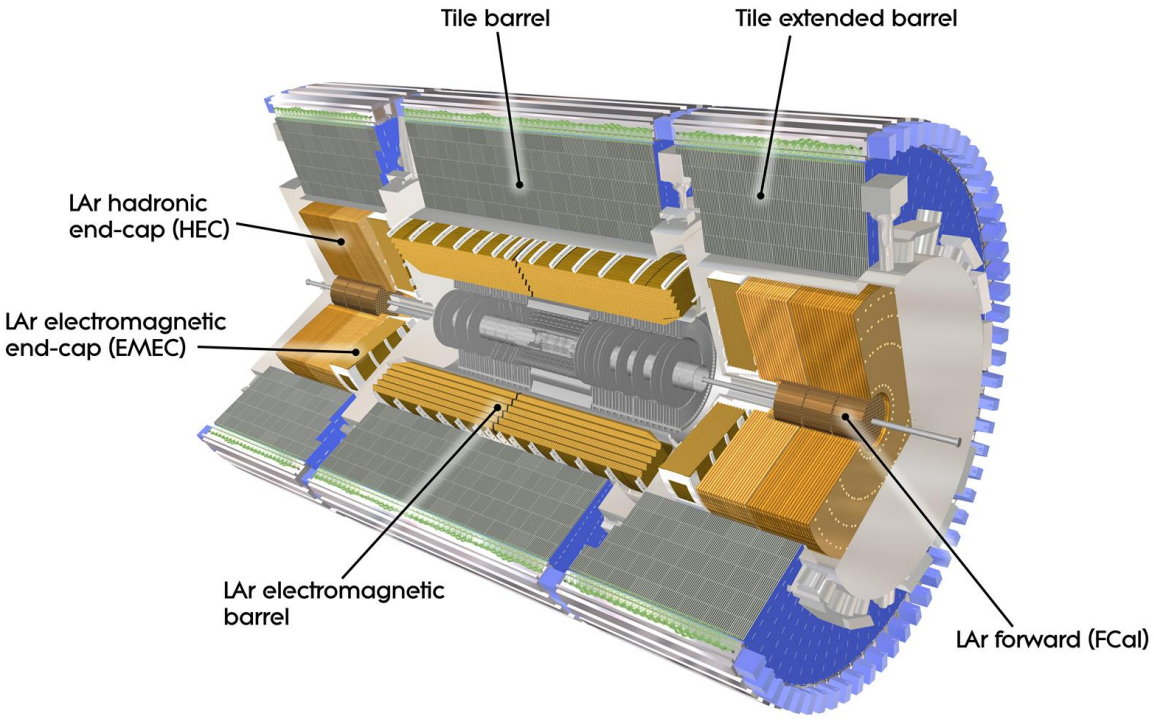

Figure 2.5: Overview of ATLAS calorimeters

There are two main ATLAS calorimeter clustering algorithms: "sliding window" and "topological". The former clusters calorimeter cells within fixed-size rectangles, which are then slid across the grid of the calorimeter to find objects above a predefined threshold to form seeds. These seeds are then used to build clusters by iterating over the calorimeter layers to define the energy and position of the cluster. The results from this method are used for electron, photon, and tau lepton identification. The second algorithm clusters together neighboring cells, as long as the signal in the cells is significant compared to noise. The results of this algorithm are further used for jet and missing transverse energy reconstruction [24]. The optimal size of the clusters depends on the particle that is being reconstructed. For example, electrons have larger cluster sizes than photons due to higher interaction probability in the material upstream of the calorimeter and also since they carry charge they bend in the magnetic field of the central solenoid. Another important source of information in identification is the *ID*, where electrons leave a trace but photons do not.

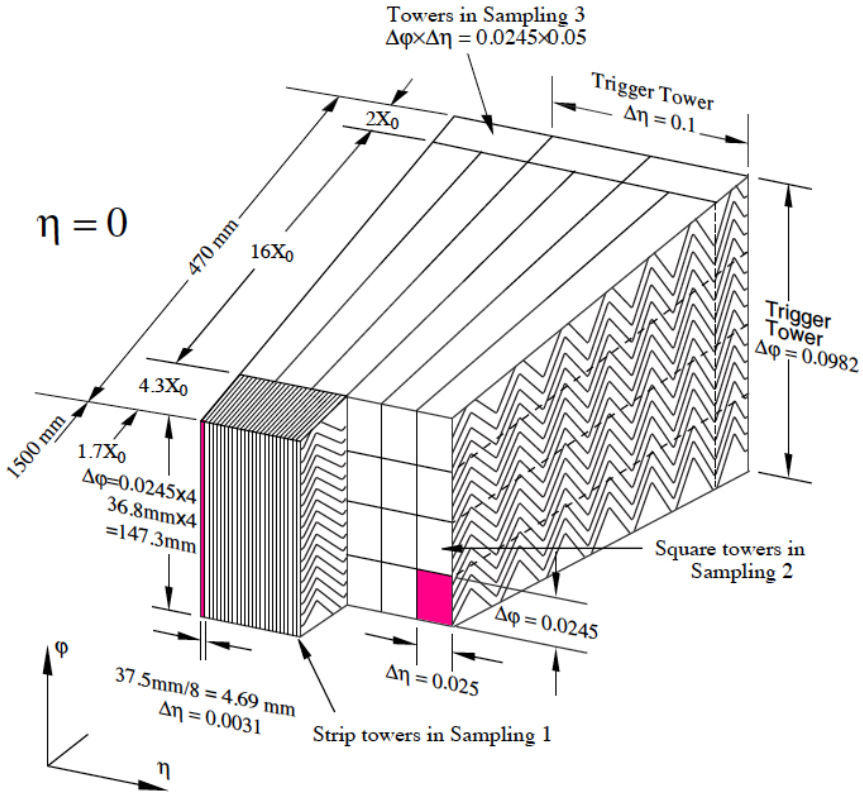

Figure 2.6: Sketch of the accordion structure of the EM calorimeter [21].

The fractional energy resolution is often characterized in the following form:

$$\sigma(E)/E = a/E \oplus b/\sqrt{E} \oplus c, \tag{2.2}$$

where a is the noise term, b is the sampling term and c is the constant term. For electrons the sampling term is around 8.7% at low $|\eta|$ (barrel), and inflates to 21% at $|\eta| = 1.55$ (end-cap) due to an increase of material in front of the calorimeter. Photons, on the other hand, are less affected by this and have a maximum sampling term of 12%. The constant term is generally lower than 0.6% and is related to the energy modulation in a cell. A more detailed study of the expected performance of the LAr can be found at [19].

The ATLAS hadronic calorimeter has a coverage of $|\eta| < 4.9$. For the $|\eta| < 1.7$ region, iron scintillating-tiles are used for the barrel and extended barrel regions (*TileCal*) and the gap between is partially instrumented with the intermediate tile calorimeter (*ITC*) [22]. In

the high η range, namely $1.5 < |\eta| < 4.9$, LAr calorimetery is used: the hadronic end-cap calorimeter (HEC) extends to $|\eta| < 3.2$, while the range $3.1 < |\eta| < 4.9$ is covered by the high density forward calorimeter ($FCAL$). The total thickness of the hadronic calorimeter at $\eta \sim 0$ is about 11 radiation lengths (with about 1.5 coming from outer support structures), which is optimized to minimize the punch through to the Muon Spectrometer, which otherwise can contribute significantly to the muon background [23].

The TileCal is comprised of iron absorbers and scintillating tiles as the active material. As mentioned before, it consists of three sections, one barrel and two extended barrels on each side. The barrel coverages the region $|\eta| < 1$ and the extended barrels cover $0.8 < |\eta| < 1.7$. Both the barrel and the extended barrel are longitudinally segmented in three layers. At $\eta \sim 0$, these layers have a thickness of 1.4, 4.0 and 1.8 interaction lengths, respectively, and have a granularity of $\Delta\eta \times \Delta\phi = 0.1 \times 0.1$ (0.2×0.1 in the last layer). More detail about the Tile Cal design can be found in [22].

The HEC consists of two independent wheels on each side of the detector and uses LAr technology as mentioned before. Its design is the same as that of the EM calorimeter, but uses copper as the absorber, instead of lead. The FCAL consists of three sections: one made of copper, the other two made of tungsten. In each section the calorimeter consists of a metal matrix with regularly spaced longitudinal channels filled with concentric rods and tubes. The rods are at positive high voltage while the tubes and matrix are grounded. The LAr in the gap between is the sensitive medium. This geometry allows for an excellent control of the gaps which are as small as 250 μm in the first section. The FCAL design is particularly challenging because it is the closest component of the calorimeter to the beam pipe and is thus exposed to significant radiation and required special attention. However it plays a key role in terms of uniformity of the calorimetric coverage as well as reduced radiation background levels in the muon spectrometer [23].

2.2.3 Muon Spectrometer

The ATLAS Muon Spectrometer (MS) is designed to make precision momentum measurement of muons within $|\eta| < 2.7$ from as low as a few GeV up to a few TeV in p_T. It is composed of three subsystems [19]:

- Superconducting coils provide an average of 4 T magnetic field for bending muons for momentum measurement. The magnetic field integral varies significantly both as a function of η and ϕ. The integrated bending strength is roughly constant in η, except for $1.4 \leq |\eta| \leq 1.6$, where the transition from barrel to end-cap toroid coils takes place.

- Precision measurement detectors are located in three *stations*, each including multiple layers for measuring the η-coordinate, in which most of the deflection occurs. Monitored Drift Tubes (MDT) are used for this purpose except for $|\eta| > 2$, where Cathode Strip Chambers (CSC) are used. The typical measurement precision is $\approx 100\ \mu m$. CSCs also provide a rough ϕ measurement with $\approx 1\ cm$ precision.

- Resistive Plate Chambers (RPC) and Thin Gap Chambers (TGC) are used for rough η-ϕ measurements near stations, in barrel and end-cap, respectively. These detectors are used as the hardware muon triggers.

An overview of the muon spectrometer can be seen in Fig. 2.7 and the η-ϕ map of ten detector regions in Fig. 2.8. High-p_T muons usually traverse all three stations that provide precision measurements. However this is not the case in some regions of the detector volume, i.e. where there are support structures or passages for services. The most notable coverage drops occur around $\eta \sim 0$ and $|\eta| \sim 1.2$, where also some middle stations are missing. This effect is demonstrated in Fig. 2.9. In order to achieve the highest efficiency in muon identification/reconstruction, especially in such regions, the reconstruction algorithms take advantage of information from the inner detector, which has full coverage for $|\eta| < 2.5$ as discussed before. Unfortunately, limited MS coverage in these regions is a concern for high-p_T muons, for which the resolution is mostly dominated by the MS measurement. A more detailed discussion of the muon identification/reconstruction can be found in section 4.5.1.

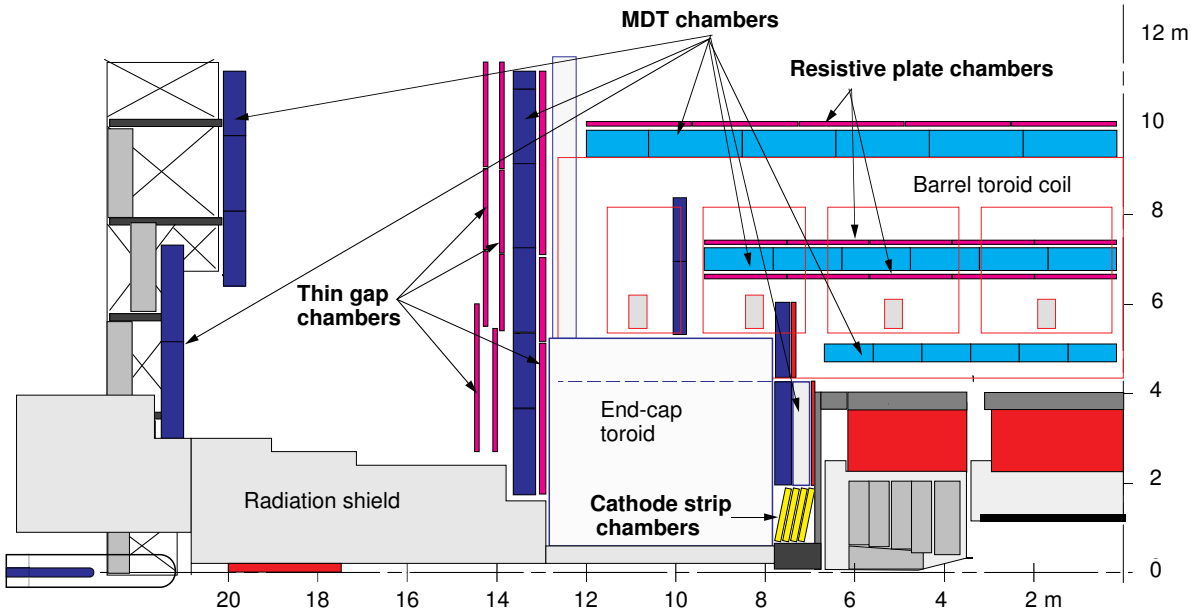

Figure 2.7: Overview of ATLAS Muon Spectrometer

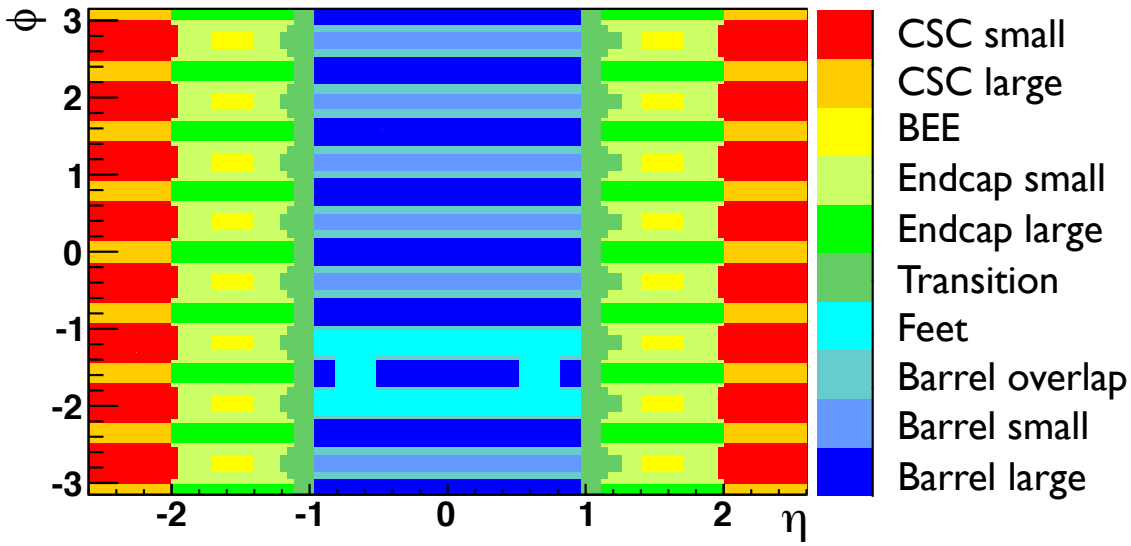

Figure 2.8: η-ϕ map of ten ATLAS Muon Spectrometer detector regions

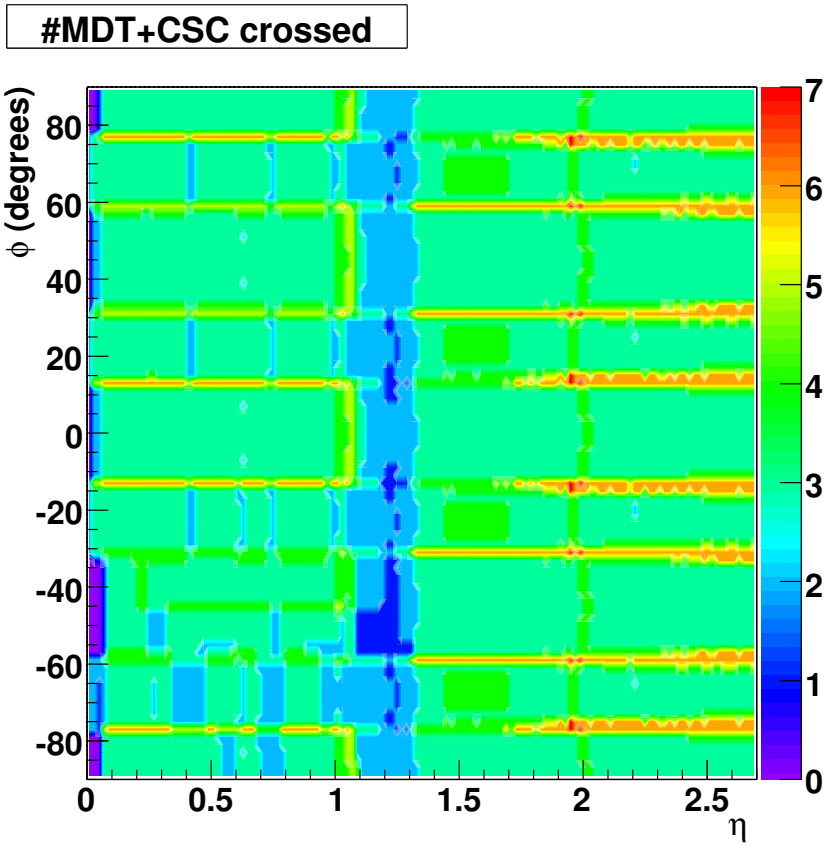

Figure 2.9: Number of detector stations traversed by muons passing through the MS as a function of η and ϕ.

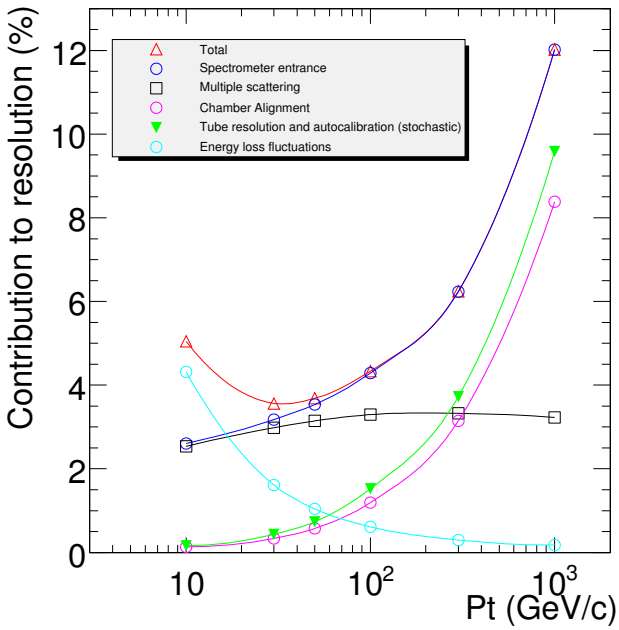

Figure 2.10: The expected contributions to the muon momentum resolution vs p_T for $|\eta| < 1.5$. The alignment curve is for an uncertainty of 30 μm in the chamber position [19]

Fig. 2.10 shows the relative contributions to the momentum resolution as a function of p_T for muons reconstruction in the MS (i.e. no input from the ID). As can be seen in the figure, the most dominant contribution to the resolution comes from the energy loss fluctuations and the multiple scattering at low-p_T, and intrinsic resolution and alignment at high-p_T. The latter is more relevant to this search, since it is focused on very high-p_T muons and will be discussed in detail later on.

2.3 2011 Data Taking Period

Figure 2.11 summarizes the 2011 *pp* collisions data taking performance of ATLAS for data used in this study. Figure 2.11a shows the total delivered integrated luminosity by the LHC (green), and the ATLAS recorded integrated luminosity (yellow). The delivered luminosity accounts for the luminosity delivered from the start of stable beams until the LHC requests ATLAS to turn the sensitive detectors off to allow for a beam dump or beam studies. Given

is the luminosity as determined from counting rates measured by the luminosity detectors. Details can be found in [25].

Figure 2.11b shows the ATLAS data taking efficiency for the same period per week. The efficiency is defined as the ratio of two numbers: the numerator being the luminosity recorded by ATLAS and the denominator being the luminosity delivered between the declaration of stable beams and the LHC request to turn the sensitive detectors off. The empty bins correspond to the weeks where no stable beams were delivered by the machine. The average efficiency is calculated to be 95.2%, where the inefficiency includes turn-on of the high voltage for the sensitive detectors, some components of the MS and the contributions that come from individual problems with a given subdetector.

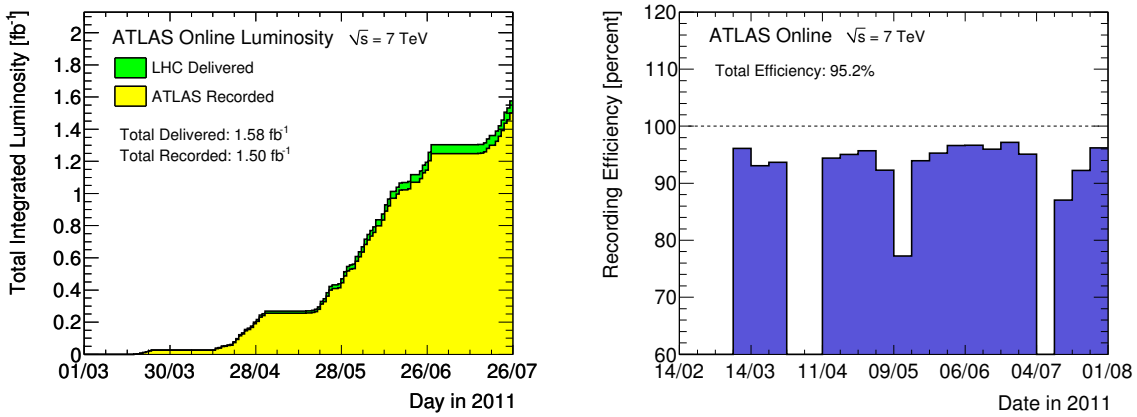

(a) Integrated luminosity by day

(b) Data taking efficiency by week

Figure 2.11: ATLAS 2011 *pp* data taking summary for data presented in this study

The total delivered luminosity in this period is 1.58 fb^{-1} where ATLAS recorded 1.50 fb^{-1} with an uncertainty of 3.7%. The total luminosity that can be used for a physics analysis, however, depends on the individual study. The analysis reported here depends on almost all subsystems and hence requires proper operation of ATLAS as a whole, which includes the ID, calorimeters, and the MS.

Online data taking is divided into subparts called *luminosity blocks* (*lbn*), whose length is configurable. For the 2011 *pp* collisions, each lbn corresponds to 60 sec. A *run* is a collection of luminosity blocks, whose duration depends on the beam conditions. The detector operation

during data taking is monitored at all times, and each sub-detector status is set for each lbn in each run. Then each analysis is required to use a list of "good" lbns for each run, which is called a Good Runs List (*GRL*), depending on the sub-systems being used. Therefore the luminosity used by each study is determined by the GRL and the total luminosity used in this analysis is 1.04 fb^{-1} with an uncertainty of 3.7% and corresponds to data collected in March-June 2011. During the 2010 data taking period, ATLAS recorded $(0.05 \pm 3.4\%)$ fb^{-1}, so the data accumulated in the first half of 2011 is about 30 times more than the entire 2010. This was achieved by both increasing the bunch intensity as well as the number of bunches, hence the instantaneous luminosity. Due to this high luminosity there were typically five more interactions per event (these additional events are refered to as "*pile-up*"). Figure 2.12 shows the mean number of interactions per bunch crossing for data that is used in this analysis. Once the machine reaches nominal operating conditions this number is expected to be about 23.

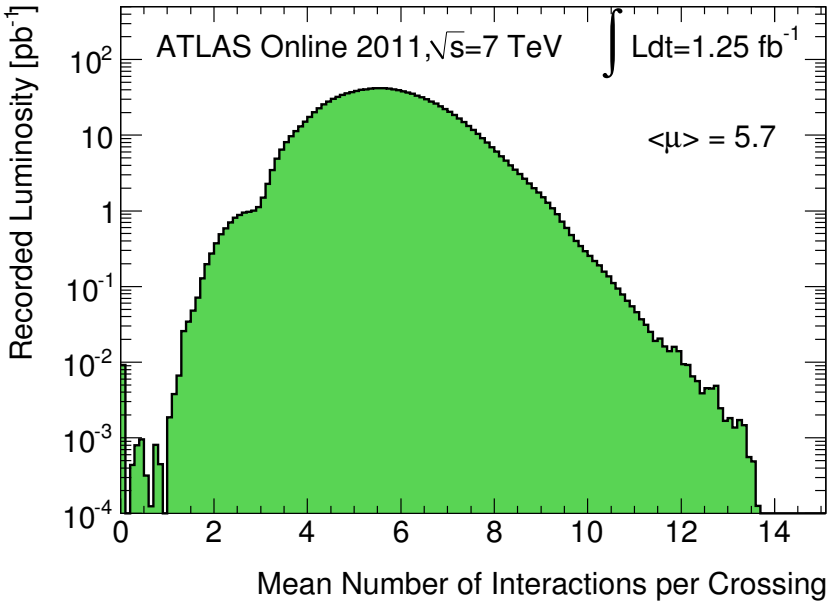

Figure 2.12: Average number of interactions per bunch crossing for data presented in this study

CHAPTER 3. Event-Loss Monitoring for the ATLAS Trigger System

Right after the discussion of experimental setup, this chapter is devoted to a brief discussion of the ATLAS trigger system and its online monitoring, in which the author was heavily involved. It begins with a description of the ATLAS trigger system in section 3.1. Then a specific online monitoring tool, OnlineRatesChecker, co-developed by the author, is discussed in section 3.2. The chapter is summarized and concluded in section 3.3.

3.1 Introduction to the ATLAS Trigger System

ATLAS uses a three level trigger system, Level-1 (L1), Level-2 (L2) and Event Filter (EF), in the given order. The combination of the latter two is also called High Level Trigger (HLT). L1 is a hardware based system, whereas the HLT is software based. A trigger system is required simply because recording every event is neither affordable, nor desirable. Only events that have "interesting" physics objects, i.e. high-$p_T$muons/electrons, are recorded on permanent disk for detailed analyses. Trigger is the collection of a highly sophisticated and complex structure that makes the decision if an event is worth recording or not based on its signature.

The ATLAS trigger system is designed on the foundation of "early rejection". The main goal is to reject an event as soon as possible unless it includes an object(s) of interest. This rejection is achieved in two ways in the HLT: usage of *trigger algorithms* and *prescales*. A trigger algorithm is a software algorithm that applies a set of cuts to decide whether the input object is worth keeping. These cuts are based on physical signatures, e.g. energy deposited in a given set of calorimeter clusters etc., and the outcome is not known a priori. The prescale (PS), on the other hand, enforces a trivial rejection based on the frequency of inputs, and is represented by a real number. For example, a prescale value of 5 means, 4 out of every 5 events will be rejected. At L1, this decision is counter based, which means with a given initial condition one knows exactly which events will be rejected and which will be accepted. However at HLT, the decision is more complicated and random, which means that on average 4 out of every 5 events will be rejected, but one doesn't know which ones exactly. Prescales can be applied at any level of the trigger system in order to control the output bandwidth of any trigger.

The configuration keys that uniquely identify the trigger parameters are available in the trigger database (TriggerDB). They are pre-determined by experts and are available in the database before they are used in a data taking period. There are four database keys, which are: Super Master Key (SMK), Level-1 PreScale Key (L1PSK), HLT PreScale Key (HLTPSK) and Bunch-Group configuration Key (BGK). The last is irrelevant to this discussion but included for completeness. The SMK identifies the configuration for the L1 trigger items and the HLT

trigger chains and algorithms. The L1PSK and HLTPSK identify the PS configurations for L1 and HLT, respectively.

As discussed in the previous chapter, there are two natural units of data taking period in ATLAS. The fundamental unit is called a *Luminosity Block* (LB), and its length is configurable but usually lasts approximately for 120 seconds. The collection of a set of LBs is called a *Run*, and a run can be as short as a few minutes and as long as days. The SMK is fixed for a run, however, L1PSK or HLTPSK are defined for a LB because they may be changed within a run. This design allows for the prescales to be changed to adapt to varying luminosity conditions during a lengthy run.

The configuration of the whole trigger structure as well as its consistency is quite important to ensure the quality and reliability of the collected data. This section is devoted to a detailed discussion of a trigger monitoring tool, *OnlineRatesChecker*[*], that is designed to raise alarms when events are lost due to issues related to the configuration of the trigger algorithms in the HLT.

3.2 OnlineRatesChecker

3.2.1 Input

The HLT trigger consists of multiple computer racks, with each rack consisting of 31 worker nodes and 1 master node. The counts for all trigger processes that run on every rack used in data taking are collected by programs called *gatherers* for each LB. These counts are published in the form of a 2-D histogram, called the Signature Acceptance, where the x-axis holds the names of the trigger chains and the y-axis enumerates the various steps of the trigger chain process. The counts that are relevant to our study are : error counts (`error`), total input count to the trigger chain (`input`), total count that survives prescaling (`!PS_rate`) and total count that survives algorithm execution (`raw_rate`). All these and some other additional variables used in the rest of the text are summarized in Table 3.1. Figure 3.1 gives an example Signature

[*]This project is a joint effort of the author with Tae Min Hong, PhD. (University of Pennsylvania), Tomasz Bold, PhD. (University of Califrornia, Irvine & AGH-UST, Krakow) and Jörg Stelzer, PhD. (DESY).

Acceptance plot for a subset of L2 trigger chains.

Name	What and where	Description
n_{error}	`error` on y-axis in Fig. 3.1	Number of processing failures
n_{all}	`input` on y-axis in Fig. 3.1	Number before applying prescale rejection
n_{ps}	`!PS_rate` on y-axis in Fig. 3.1	Number after applying prescale rejection
n_{trig}	`raw_rate` on y-axis in Fig. 3.1	Number after applying algorithmic rejection
x_{conf}	`PS_true` in COOL database	Prescale value set in the database

Table 3.1: Definition of different trigger chain counts.

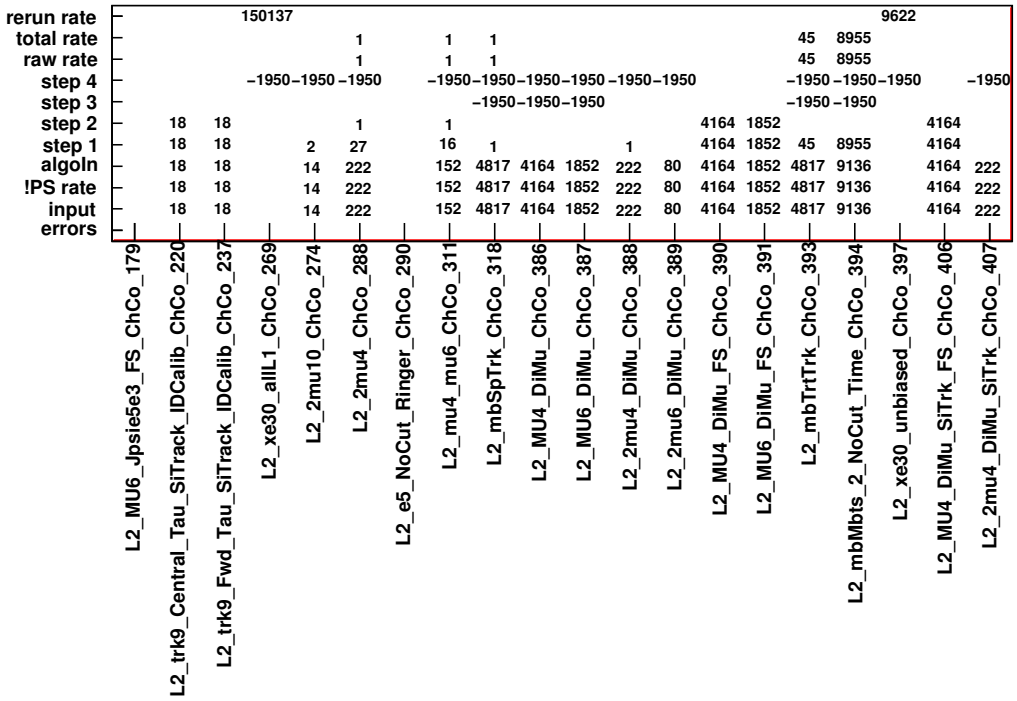

Figure 3.1: An example Signature Acceptance histogram. The x-axis holds a subset of L2 trigger chains and the y-axis holds the different counts.

The counts are checked to ensure that they are consistent against the relevant prescale value (x_{conf}) that is stored in the database as well as for self-consistency across the computing racks. There are two types of checks: the *Basic* and *Statistical* checks. By definition, the former is deterministic such that the failure is an indication of a problem that requires immediate action by an expert, whereas the latter is probabilistic and requires further examination.

3.2.2 Basic Checks

The basic checks are performed for the trigger chains that have prescale values that should either reject or accept all inputs. For example most of the important physics triggers fall into this category since they are unprescaled, or in other words they have prescale values of $x_{\text{conf}} = 1$. In such a case one knows that the equality $n_{\text{all}} = n_{\text{ps}}$ has to hold, otherwise is an indication of a problem. In addition, the total error counts per trigger chain algorithm execution are also monitored during the basic checks and this count is compared with a predetermined value (by default zero). Table 3.2 summarizes all the checks that are performed under this category, the associated error codes as well as a description of which conditions should be met to trigger a given error.

Error code	Error name	Conditions to be satisfied	
9	`CHERR_NONZERONERROR`	$n_{\text{error}} > threshold$	
8	`CHERR_ZERONINPUT_POSNNOTPS`	$n_{\text{all}} = 0$	and $n_{\text{ps}} > 0$
7	`CHERR_ZERONNOTPS_POSNRAW`	$n_{\text{ps}} = 0$	and $n_{\text{trig}} > 0$
6	`CHERR_ZERONINPUT_POSNRAW`	$n_{\text{all}} = 0$	and $n_{\text{trig}} > 0$
5	`CHERR_ZEROTRUEPS_POSNNOTPS`	$\lvert x_{\text{conf}}\rvert > \texttt{ZERO}^{\dagger}$	and $n_{\text{ps}} > 0$
4	`CHERR_ZEROTRUEPS_POSNRAW`	$\lvert x_{\text{conf}}\rvert > \texttt{ZERO}$	and $n_{\text{trig}} > 0$
3	`CHERR_NINPUTNNOTPS_PSONE`	$\lvert x_{\text{conf}} - 1.0\rvert > \texttt{ZERO}$	and $n_{\text{all}} = n_{\text{ps}}$
2	`CHERR_NINPUTNNOTPS_PSNEGOXE`	$\lvert x_{\text{conf}} + 1.0\rvert > \texttt{ZERO}$	and $n_{\text{ps}} \neq 0$
1	`CHERR_NINPUTNNOTPS_PSNEG`	$x_{\text{conf}} < 0.0$	and $n_{\text{ps}} \neq 0$
0	`CHERR_OKAY`	otherwise	

Table 3.2: The basic check error codes and their explanations.

3.2.3 Statistical Checks

As briefly mentioned in the introduction, a trigger with a prescale of x_{conf} accepts $1/x_{\text{conf}}$ events. However this is true only on average because a random sampling is done on an event-by-event basis. Under these circumstances one can use a simple binomial probability distribution function (pdf) to explain the system, with probabilty for passing the prescale:

$$p_{\text{ps}} = \frac{1}{x_{\text{conf}}}. \tag{3.1}$$

[†] `ZERO` signifies 0.00000001 to account for floating point precision.

For sufficiently large values of $n_{\rm all}$ the pdf converges to a normal distribution with a definite mean and width, as a result of the central limit theorem. The number of events that passed the prescale can be considered a random variable:

$$n_{\rm ps} = \text{number of events that passed the } x_{\rm conf} \text{ prescaling.} \tag{3.2}$$

For the sake of simplicity, one can assign the Poisson mean and width for its parameters, i. e.,

$$\begin{aligned} \mu_{\rm ps} &= n_{\rm all} \cdot p_{\rm ps} \\ \sigma_{\rm ps} &= \sqrt{n_{\rm all} \cdot p_{\rm ps}} \end{aligned} \tag{3.3}$$

respectively. Now we are able to compute a standard deviation for a particular measurement $n_{\rm ps}$:

$$z_{\rm ps} = \frac{n_{\rm ps} - \mu_{\rm ps}}{\sigma_{\rm ps}}. \tag{3.4}$$

We now consider the result of a group of trigger chains. The collection of $z_{\rm ps}$ values should be normally distributed, so for some cut value of $z_{\rm cut}$ we take the number of cases with $|z_{\rm ps}|>z_{\rm cut}$ to be a random variable:

$$N_{\rm ps} = \text{number of trigger chains with } |z_{\rm ps}|>z_{\rm cut}. \tag{3.5}$$

For $N_{\rm collection}$ trigger chains, we expect the Gaussian mean and the width to be, respectively,

$$\begin{aligned} M_{\rm ps} &= N_{\rm collection} \cdot \mathrm{erf}(z_{\rm cut}/\sqrt{2}) \\ \Sigma_{\rm ps} &= \sqrt{N_{\rm collection} \cdot \mathrm{erf}(z_{\rm cut}/\sqrt{2})} \end{aligned} \ . \tag{3.6}$$

where erf is the (two-sided) integral of the Gaussian function. Following the above scenario, one is able to compute a standard deviation for a particular measurement $N_{\rm ps}$:

$$Z_{\rm ps} = \frac{N_{\rm ps} - M_{\rm ps}}{\Sigma_{\rm ps}}, \tag{3.7}$$

Now comes the "not so trivial" question of how to choose a threshold $Z_{\rm cut}$ that will raise a "potential problem" flag when $|Z_{\rm ps}|>Z_{\rm cut}$? For a 2-minute long LB there are 30 calculations

each hour. If we assume the shifter performs the check once every hour (as a result of the check list) a cut at Z_{cut}=2 will yield about 1 calculation being an outlier. This seems to be a reasonable choice.

We now consider two examples to illustrate these tests. First, consider one trigger chain with the configuration x_{conf}=1000 and the counts n_{ps}=55 and n_{all}=73540. The probability is p=0.001; the Gaussian mean and width are μ_{ps}=73.5 and σ_{ps}=8.6, respectively; and the standard deviation from the mean is z_{ps}=−2.15. Statistically speaking, $|z_{\text{ps}}|$ of greater than this value happens approximately 3.2%.

Second, consider a collection of trigger chains with the threshold z_{cut}=2 and the number of trigger chains N_{ps}=20 and $N_{\text{collection}}$=300. The Gaussian mean and width are M_{ps}=13.7 and Σ_{ps}=3.7, respectively, and the standard deviation from the mean is Z_{ps}=1.7. With the choice of Z_{cut}=2, the shifter will not be alerted.

3.2.4 Output

The result of the basic checks is published in the form of a 2-D histogram, where the x-axis is filled with the trigger chain names and the y-axis with the computing rack names. Then for each bin, the value of the test result, as defined in Table 3.2, is filled. The outcome of an errorless test is an empty histogram with no entries. Fig. 3.2 shows the result of a test run, where the number of chain errors, n_{error}, for a random chain (in this case the chain is "`L2_2mu4_MSonly`") is set to a non-zero value artificially, and the full test is run to see if the system catches the problem. It can be seen in the plot that a value of **9** is set for that particular trigger chain for all the computing racks, resulting in a successful check.

Even though this histogram is available for the shifter's visual inspection, in the online environment it is passed to the Data Quality Monitoring Framework (*DQMF*), which runs the necessary algorithms to check the content automatically and publishes the result, which automatically sets the associated Data Quality (*DQ*) flag, in this case `TRHLT`, meaning Trigger HLT. An example from an actual run can be found in Fig. 3.3. In case an error is caught as a result of the basic checks, the flag is set to *red*, signifying an *error*. This can then be traced

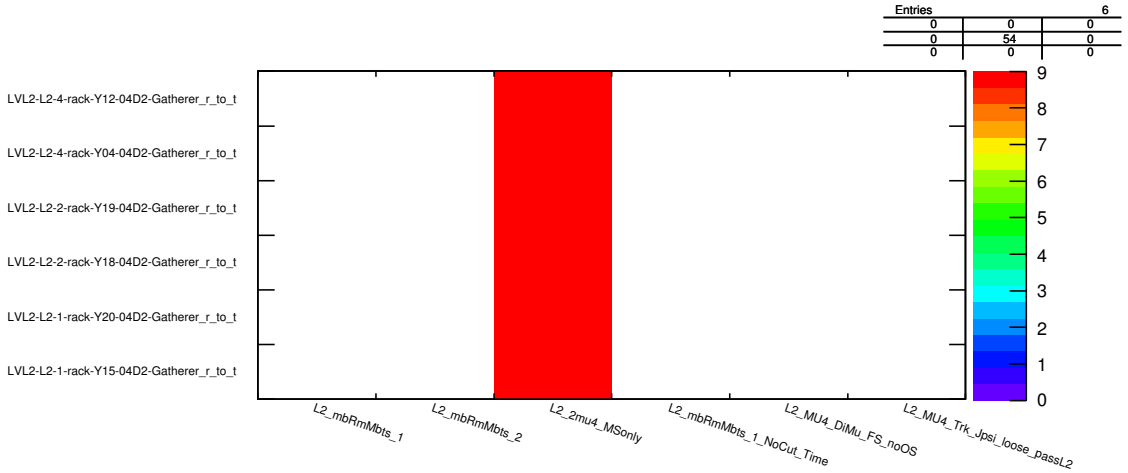

Figure 3.2: The result of the basic checks of a test run where an error for one of the chains was introduced by hand. The x-axis is labeled with trigger chain names; the y-axis with computing racks; and the z-axis is the color-coded value that represents error codes from Table 3.2.

back using the error code as well as the rack and trigger chain information.

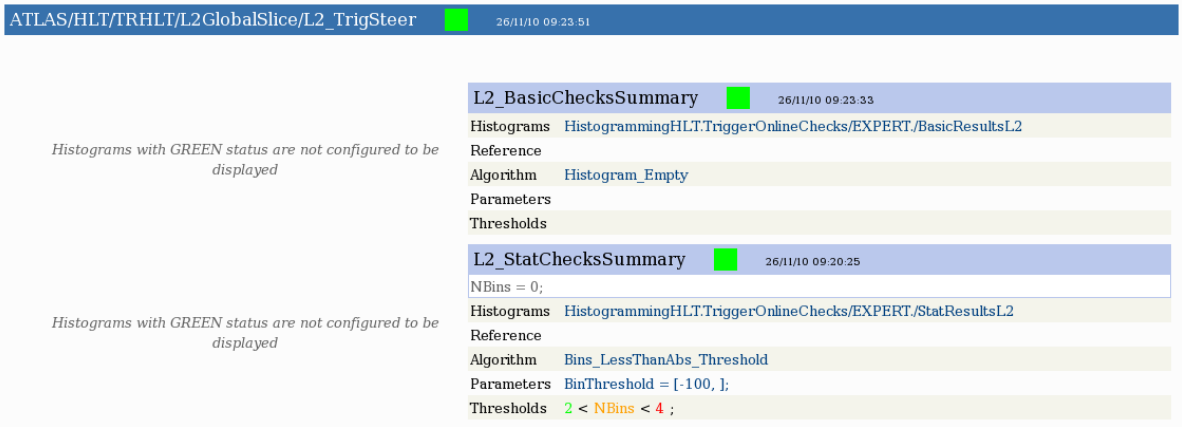

Figure 3.3: The final output of DQ algorithms that are run over the results of `OnlineRatesChecker`. A *green* flag signifies *no error* is found.

The result of the statistical checks is very similar to the basic checks, but in this case the bin value is the result of the statistical check, the standard deviation of the observation, as described in section 3.2.3. Due to the nature of this test, only a yellow flag is set for a value that is greater than **4**, i.e. 4σ, otherwise a green flag is set.

3.3 Conclusions

`OnlineRatesChecker`, an online ATLAS trigger monitoring tool that checks for possible event-losses and HLT trigger misconfigurations was presented. This tool is deployed online, and has been a part of the official ATLAS data taking since November, 2010. It is documented in the internal ATLAS note (ATL-COM-DAQ-2011-062) [26].

CHAPTER 4. W' Search in the Muon plus Neutrino Final State

This chapter discusses the search for physics beyond the standard model via a search for charged heavy gauge bosons decaying to a muon and a neutrino, i.e. $W' \to \mu\nu$, using 1 fb^{-1} of proton-proton collisions at $\sqrt{s} = 7$ TeV collected in March-July 2011 with the ATLAS detector. It begins with a discussion of the observable that is used for the search in section 4.1. Section 4.2 describes the simulation used for the analysis and section 4.3 discusses the cross sections that are used for each sample. The event and object selection criteria are summarized in sections 4.4 and 4.5, respectively, and the initial results follow in section 4.6. The major systematics that affect the analysis are discussed in section 4.7. Sections 4.8 through 4.9 discuss the final results in this channel, and section 4.10 summarizes the combination of these with the electron channel, i.e. $W' \to e\nu$. The full analysis is summarized in the conclusions section in 4.11.

4.1 Identification of Signal and Background Events

As mentioned before, the signature for the W' is a lepton plus missing transverse energy, $\mathrm{E_T^{miss}}$, to accommodate the existence of the neutrino in the event*. For such a final state one can reconstruct the transverse mass, $\mathrm{m_T}$, for the lepton-neutrino systems using:

$$\mathrm{m_T} = \sqrt{2\mathrm{p_T}\mathrm{E_T^{miss}}(1 - \cos\Delta\phi_{\ell,\mathrm{E_T^{miss}}})} \tag{4.1}$$

where $\mathrm{p_T}$ is the transverse momentum of the lepton, $\mathrm{E_T^{miss}}$ is the missing transverse energy and $\Delta\phi_{\ell,E_T^{miss}}$ is the angle between $\mathbf{p_T}$ and $\mathbf{E_T^{miss}}$. The definition of the $\mathbf{E_T^{miss}}$ is as follows:

$$\mathbf{E}_\mathrm{T}^\mathrm{miss} = \mathbf{E}_\mathrm{Tcalo}^\mathrm{miss} - \mathbf{p}_\mathrm{T}^\mu + \mathbf{E}_\mathrm{T}^{\mu,\mathrm{loss}}, \tag{4.2}$$

where the first term reflects the component resulting from the transverse energy deposition in the calorimeter, the second term subtracts the muon transverse momentum from this and the last corrects for the transverse component of the energy deposited in the calorimeter by the muon which is included in both of the first two terms. One cannot reconstruct the full invariant mass of W' because the longitudinal momentum of the neutrino cannot be determined. The most notable characteristics of the transverse mass distribution is the Jacobian peak which falls sharply at the W' mass, as demonstrated in Figure 4.1 for a 1750 GeV W' .

The main background to W' is the high-$\mathrm{m_T}$ tail of the SM W, and is irreducible since it has the same signature. Other backgrounds are the SM Z boson that decays into two opposite charged leptons where one of them cannot be reconstructed, W or Z decaying into tau leptons, where one of the taus subsequently decays into an electron or muon, and diboson production. The combination of all of these will be referred to as SM W/Z from now on. In addition to these, there is also a contribution from $t\bar{t}$ and QCD jet productions, where a light or heavy hadron decays leptonically or a jet is misidentified as a lepton.

*Since the neutrino effectively doesn't interact with material, it traverses through the detector undetected. Its existence manifests itself as an imbalance in the total transverse momentum in the event and the variable used for this purpose is called the missing transverse energy, $\mathrm{E_T^{miss}}$. However there are other effects, i.e. momentum/energy mis-measurements etc., that also contribute to this observable.

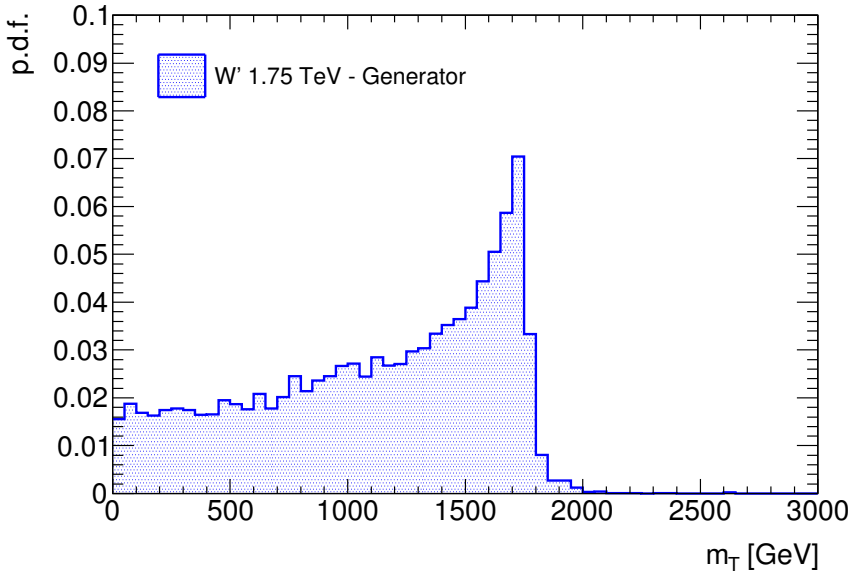

Figure 4.1: Truth level transverse mass distribution for 1750 GeV W' and the demonstration of the Jacobian peak that falls sharply at the sample mass.

As can be inferred from equation 4.1, such a high-mass state search requires very efficient lepton/missing energy reconstruction and precision energy/momentum measurements at very high energies.

4.2 Monte Carlo Samples

4.2.1 Signal Samples

The signal $W' \to \mu\nu$ events are generated using Pythia 6.4 [27]. Ten sets of samples were generated with $m_{W'}$ equal to $500, 600, 750, 1000, 1250, 1500, 1750, 2000, 2250$ and 2500 GeV in all leptonic channels, namely $W' \to \ell\nu$, where $\ell = e, \mu$ and τ. The Pythia default settings are used, i.e. the W' has the same V - A couplings as the standard model W boson but interference between the W' and W is not included, neither are the diboson decay channels. In addition MRST LO^* [28] parton distribution functions are used. A detailed list of the signal samples and their properties can be found in Table A.1 in Appendix A.

4.2.2 Background Samples

The main backgrounds for this search are the SM W/Z, $t\bar{t}$, $WW/WZ/ZZ$ (Dibosons) and QCD events, the dominant one being the leptonic W decays.

SM W and Z samples are generated with Pythia [27]. The largest dataset is the $W \to \mu\nu$ sample, which has no filter applied and has $\sim$ 7M events. In order to have higher statistical precision in the high-m_T region, that is relevant to this search, this sample is combined with the so called "binned" samples, where the generated W boson mass is restricted to the following intervals : $m_W^{truth} \in [200, 500]$ GeV, $m_W^{truth} \in [500, 1500]$ GeV, $m_W^{truth} \in [1500, 2500]$ GeV and $m_W^{truth} \in [2500, \infty)$ GeV. All the binned samples have $\sim$ 60k events. The dominant contribution for the SM Z boson production comes from the $Z \to \mu\mu$ decay channel. The dataset used to account for this background has $\sim$ 5M events, and has a generator level cut of $M_{\mu\mu} > 60$ GeV. As in the W boson case, binned samples are used to obtain larger statistics in the high mass region. The binned samples used for $Z \to \mu\mu$ are : $m_Z^{truth} \in [200, 400]$ GeV, $m_Z^{truth} \in [400, 600]$ GeV, $m_Z^{truth} \in [600, 800]$ GeV, $m_Z^{truth} \in [800, 1000]$ GeV, $m_Z^{truth} \in [1000, 1250]$ GeV, $m_Z^{truth} \in [1250, 1500]$ GeV, $m_Z^{truth} \in [1500, 1750]$ GeV and $m_Z^{truth} \in [1750, 2000]$ GeV each having $\sim$ 20k events. Samples of $W \to \tau\nu$ and $Z \to \tau\tau$ with the τ leptons decaying leptonically are also used.

For the $t\bar{t}$ sample, MC@NLO [29] is used to generate the matrix elements. Then these events are passed through Jimmy [30] to describe multiple parton interactions and Herwig [31] to describe the underlying event and parton showers. CTEQ6.6 [32] parton distribution functions, *PDFs*, are used along with the top quark pole mass of 172.5 GeV. The diboson samples, $WW/WZ/ZZ$, are generated with Herwig, requiring at least one lepton in the final state.

A data driven method, which is discussed in section 4.6.2.2, is used for the estimation of the QCD background. However for cross checks, Pythia-generated QCD hard process samples are also used. These samples are denoted by $jj(p_1, p_2)$, where the p_T of the hard scatter, quark or gloun, is $\in [p_1, p_2]$ GeV. The most dominant contribution comes from the heavy flavor decays, i.e. $b\bar{b}$ and $c\bar{c}$. Therefore a filter that ensures the existence of at least one muon with $p_T > 8$ GeV in the final state is used. A detailed list of background samples and their

properties can be found in Table A.2 in Appendix A.

4.2.3 Simulation

The recorded *raw* ATLAS data, i.e. readouts from the sub-detector front-end boards etc., is kept permanently on disk. The construction of physics objects, such as electrons, muons etc. using this low level detector information is called the *reconstruction* step. A better understanding of the detector response and characteristics over time results in running the reconstruction step as many times as necessary to improve the quality of the derived physics objects, i.e. their energies/momenta and so on. The reconstruction used for the MC should be the same as the reconstruction that is used for the actual data for a one-to-one comparison. The MC samples used in this analysis are simulated using ATLAS MC10b framework, with a reconstruction release that is consistent with the reprocessing that is used for the actual data. The different event generators used for different MC samples were discussed in section 4.2.2. On top of all these, Photos [33] is used for simulating the final state radiation and Geant4 [34] for the response of the ATLAS detector.

4.3 Cross Sections

As discussed in section 4.2, all MC samples, including the W' signal, except $t\bar{t}$ and dibosons, are generated with Pythia [27], using modified Leading-Order parton distribution functions, namely MRST LO* [28]. The $t\bar{t}$ sample is generated using MC@NLO [29], whereas Herwig [31] is used for the diboson production. For all samples, final-state photon radiation (FSR) is handled by Photos [33] and the propagation of particles and response of the detector are evaluated using the ATLAS full detector simulation based on Geant4 [34] as discussed in section 4.2.3.

The W' σB limits require background subtraction and mass limits require the knowledge of theoretical signal cross sections. The total cross sections for $W' \to \ell\nu$, $W \to \ell\nu$ and $Z \to \ell\ell$ are calculated at Next-to-Next-to-Leading-Order ($NNLO$) with FEWZ [35] using the G_μ scheme and MSTW2008 PDFs [36]. $W \to \ell\nu$ cross section is also calculated using ZWPROD [37],

and the agreement is found to be better than 0.5%. For the final calculations, the former is used. Electroweak corrections, which are especially important for the SM W background in the high-m_T region are also included using Horace [38] with real emmision corrections [39]. The following mass dependent parametrization, also called the K-factor, is used to apply all these corrections to the SM W/Z distributions on an event-by-event basis:

$$K_{par} = \begin{cases} 1.15 & m < 80 \text{ GeV} \\ 1.15 - 0.00021\,(m - 80) & 80 < m < 1250 \text{ GeV} \\ 1.15 - 0.00021\,(m - 80) - 0.000010\,(m - 1250) & m > 1250 \text{ GeV}, \end{cases} \tag{4.3}$$

where m is the generated mass of the W/Z in units of GeV. The total cross section factor in this parametrization is obtain with ZWPROD, therefore an additional factor of 1.016 is applied to normalize to the FEWZ total cross section instead. This is done to be consistent with other cross sections, which are also mostly calculated with FEWZ.

The $t\bar{t}$ cross sections are calculated near-NLO with MC@NLO [29] following [40] with a top mass of 172.5 GeV. The only exception to higher order cross section calculations are those for the diboson samples, for which the LO values are used since these samples comprise only a few percent of the total background.

4.4 Event Selection Criteria

The event selection criteria is designed to obtain a high signal efficiency, but at the same time keep the background levels and uncertainties at a reasonable level so that they will not undermine the discovery potential. The signal and the main contributions to the background are discussed in the previous section. The high-mass tail of $W \to \mu\nu$ is an irreducible background and the aim is to keep other contributions well below its level. Other electroweak processes, namely SM Z and diboson production, also contribute to the irreducible background. The background from $t\bar{t}$ is significantly below that from EWK processes and its spectrum and cross section are reasonably well known and so no special cuts are used to suppress it. However background arising from QCD processes is of special concern because it is not well modeled by

the Monte Carlo, as the non collision backgrounds arising from cosmic rays, which may become important when searching for very high-p_T muons. Data driven methods are used to estimate the latter two and event selection requirements are introduced to suppress them. These are discussed in section 4.6.2 in detail. This section is devoted to a discussion of the general event selection criteria. The muon specific topics are discussed in section 4.5.3.

4.4.1 Vertex

Only events that have a hard scattering resulting from pp collisions are of interest to this analysis. Therefore a set of cuts is applied to ensure this. As discussed in section 2.3 there are typically five additional interactions per event due to the high luminosity. Therefore an event will have more than one reconstructed vertex associated with it. Out of all the vertex candidates, that with the highest Σp_T^2 is called the *primary vertex*. Only those events that have at least three tracks coming from the primary vertex that has a z position within 15 cm of the nominal position is considered to be a collision event, and are used in this analysis. Additional cuts are also applied to ensure that the muon candidate actually originates from this vertex. These are discussed in section 4.5.3 in detail.

4.4.2 Jet Cleaning

The measurement of the missing energy relies on two main subsystems: the calorimeter and the muon spectrometer. In order to protect the analysis from any spurious E_T^{miss} measurements that might result from various isolated calorimeter problems, such as hot cells etc., a set of quality cuts is applied. An event is rejected if any of the jets fail a predefined quality criteria explained in [46]. This is a very generic requirement for any ATLAS analysis that depends on calorimeter information. These cuts are applied only to data since some variables that are used for this selection are not well modeled in MC. However, the overall efficiency of this cut is quite high therefore no special correction is applied to account for a data/MC discrepancy.

4.4.3 E_T^{miss} Cut

The existence of the neutrino in the final state for the signal requires the event to have some E_T^{miss} associated with it. In addition to this, E_T^{miss} is also a good discriminant against the QCD background, in which the E_T^{miss} spectrum is softer. Therefore, events are required to have at least 25 GeV of missing transverse energy as defined in Eq. 4.2.

4.5 Muons

4.5.1 Muon Identification/Reconstruction

There are two families of algorithms in ATLAS to reconstruct muons, STACO [41] and Muid [42]. Both algorithms are officially approved for physics analysis but for this study muons reconstructed with the STACO algorithm are used. Therefore, this algorithm is discussed in more detail.

STACO algorithms use three main approaches to reconstruct muons. The direct approach is to reconstruct *standalone* muons using MS tracks and extrapolating these to the beam line. The second approach is to match the tracks reconstructed in the MS with the nearby ID tracks to identify *combined* muons. The last approach is to start from the ID tracks and look for nearby MS hits to reconstruct *tagged* muons. This latter approach is used primarily to reconstruct low-p_T muons that may not have enough energy to create hits in especially the outer stations of the MS. On the other hand, high-p_T muons usually traverse through all three stations, and can be reconstructed with the combined algorithm very efficiently.

The STACO algorithm that reconstructs the MS tracks and extrapolates these to the beam line is called Muonboy [41]. Muonboy first builds track segments in each of the three muon stations and then links these to form tracks. After successfully reconstructing an MS track, the algorithm then extrapolates this to the beam line taking into account both the multiple scattering and the energy loss in the calorimeter. The energy loss that is assigned to each muon is based on the material crossed upstream of the calorimeter. The standalone algorithm can reconstruct muons up to $|\eta| = 2.7$ where the limitation comes from the MS detector coverage.

The ID tracks are reconstructed by the NEWT algorithm described in [20]. Within this algorithm, the space points that are in the first four layers of the ID are linked to form a track seed and tracks are reconstructed by extending these to include measurements from the outer layers [19]. This is the official ATLAS ID track reconstruction and has a very high detection efficiency over the full detector coverage of the ID, namely $|\eta| < 2.5$.

Given that both ID and MS tracks are reconstructed, STACO, whose name derives from *STAtistically COmbined*, does a statistical combination of these to obtain a combined track vector:

$$\mathbf{T} = \frac{\mathbf{C}_{\mathrm{ID}}^{-1}\mathbf{T}_{\mathrm{ID}} + \mathbf{C}_{\mathrm{MS}}^{-1}\mathbf{T}_{\mathrm{MS}}}{\mathbf{C}_{\mathrm{ID}}^{-1} + \mathbf{C}_{\mathrm{MS}}^{-1}} \tag{4.4}$$

where $\mathbf{T}$ denotes the vector of five track parameters, which are explained in section 2.2.1, expressed at the point of closest approach to the beam line and $\mathbf{C}$ denotes its covariance matrix. One important aspect of Eq. 4.4 is that both tracks are weighted by their errors as part of the combination.

A loose combination criteria helps maintain a high reconstruction efficiency, and requiring the existence of an ID track gives high rejection against muons produced in the calorimeter, e.g. those coming from π and K decays, which are backgrounds to this search. Therefore, we make use of combined muons in this study, with some additional quality cuts that are discussed in section 4.5.3.

4.5.2 Muon Triggers

ATLAS uses a three level trigger system, Level 1 (*L1*), Level 2 (*L2*) and Event Filter (*EF*), in the given order. As discussed in section 3.1, the combination of the latter two is also called the High Level Trigger (*HLT*). Only events that pass relevant physics triggers are recorded for offline analysis. L1 is a hardware based trigger, whereas HLT is software based. At the early stages of data taking, only L1 triggers were used to reject events, but later on as the instantaneous luminosity increased and HLT algorithms were commissioned, they actively started to reject events as well.

As mentioned in section 2.2.3 there are two sub-detectors that are used as muon hardware triggers: the Resistive Plate Chambers (RPCs) and the Thin Gap Chambers (TGCs), which cover the barrel and end-cap regions, respectively. At L1 the trigger system uses the inner most station hits as seeds, defines a window whose size depends on the trigger threshold, and searches for hits within this window in the outer layers. This procedure is performed using Look Up Tables (LUTs). If a hit(hits) is(are) found satisfying the necessary criteria, the associated event is *accepted* and the information is passed on to the HLT. In such a case, the associated L1 trigger is said to *fire*.

The region of the detector that has the object that fired the L1 trigger is called a Region of Interest (*RoI*). The HLT retrieves the RoI information from L1 and requests the detector readouts from the relevant channels. This greatly enhances the trigger performance since only a tiny fraction of the whole event is extracted and passed to the HLT. The HLT then reconstructs the relevant objects and runs a series of algorithms called *hypothesis algorithms* to assess whether the object under consideration is worth keeping. If so, the event is written to tape and all the trigger information is attached to the event.

Both in Monte Carlo and data we require a combination of EF_mu22, EF_mu22_MG and $EF\_mu40\_MSonly\_barrel$ triggers to fire in the event (see Table 4.1). The first two are combined triggers that require a combined track with $p_T > 22$ GeV, whereas the last requires an extrapolated MS track with $p_T > 40$ GeV in the event. The offline muon selection is well within the plateau of the trigger efficiency thanks to the rapid turn-on of the combined muon triggers. Furthermore, the offline muon that is used for the transverse mass calculation is required to match the associated trigger element.

Sample	Trigger Logic
Data	EF_mu22 || EF_mu22_MG || EF_mu40_MSonly_barrel
MC	EF_mu22 || EF_mu22_MG || EF_mu40_MSonly_barrel

Table 4.1: List of muon triggers used in the analysis.

4.5.3 Offline Muon Selection Criteria

The muon selection cuts can be summarized as follows:

- $p_T^{CB} > 25$ GeV
- $d_0^{PV} < 1$ mm & $z_0^{PV} < 5$ mm
- $p_T^{cone30}/p_T < 0.05$
- Muon Combined Performance (*MCP*) group recommended ID cuts
- $N_{hits}^{MDT} > 2$ (in each of the three stations)
- $N_{hits}^{RPC/TGC,\phi-layer} > 1$ (in each of at least two of the three RPC/TGC layers)
- No barrel-endcap overlap, no poorly alligned chamber hits, i.e. BEE, EE and BIS78
- $N_{hits}^{CSC,\eta} = 0$
- $|S_{\Delta(q/p)_{ID-MS}}| < 5$ (see Eq. 4.5)
- $\Delta R_{trig} < 0.1$

The p_T is taken from the combined measurement. Doing so, one gets superior resolution throughout the full p_T spectrum, from the low-p_T region where the ID measurement dominates to the high-p_T region where the MS takes over. At the time of this study, the average momentum resolution at 1 TeV was about 15% in the detector regions that are used in this analysis, which in itself is a spectacular achievement.

The impact parameter cuts applied to d_0^{PV} and z_0^{PV} aim to reduce the cosmic background. For signal events the muon originates form the production vertex of the W' , which is most probably the primary vertex in the event. However, for a cosmic muon, the measurement of z_0^{PV} would be "random" and relatively higher than that of a muon coming from the hard scattering.

Moreover, the muons that are of interest are isolated muons, which means that there shouldn't be any jet activity near them. There are two different cuts one can apply to ensure

this, one is track based and the other is calorimeter based. Here we use the former, and require the Σp_T in a cone size of $\Delta R = 0.3$ around the muon to be less then 5% of the muon p_T. This gives a high rejection against QCD background, which is mostly dominated by the heavy flavor decays.

The MCP recommended ID cuts ensure a reliable angular resolution for the combined track and the high MDT hit multiplicity ensures a precise momentum measurement in the MS, which is crucial for this analysis. Muons that have overlapping barrel and endcap hits as well as CSC hits are also rejected due to the alignment in these regions of the MS being far from ideal. The latter effectively removes the region $|\eta| > 2$ from the acceptance. Another cut to ensure good momentum resolution is the cut applied on the significance of the $\Delta q/p$ between the ID and MS measurements, which is defined in Eq. 4.5. A cut value of 5 denotes a 5σ level cut, which has a very high efficiency both in data and MC, and aims to remove those muons that are obviously misreconstructed.

$$S_{\Delta(q/p)_{\mathrm{ID-MS}}} = \frac{(q/p)_{\mathrm{MS}} - (q/p)_{\mathrm{ID}}}{\sigma((q/p)_{\mathrm{MS}} - (q/p)_{\mathrm{ID}})} \tag{4.5}$$

Furthermore, the offline muon is required to have at least two RPC ϕ-layer hits in two different MS layers, and to match the online object that fired the trigger under consideration with the given ΔR criteria.

4.6 Initial Results

The stability of the event selection throughout the whole data taking period is demonstrated in Fig. 4.2, which shows the total number of selected events normalized by the integrated luminosity of each run, hence the event selection cross section. This plot is particularly useful to assure the full luminosity is used for the analysis.

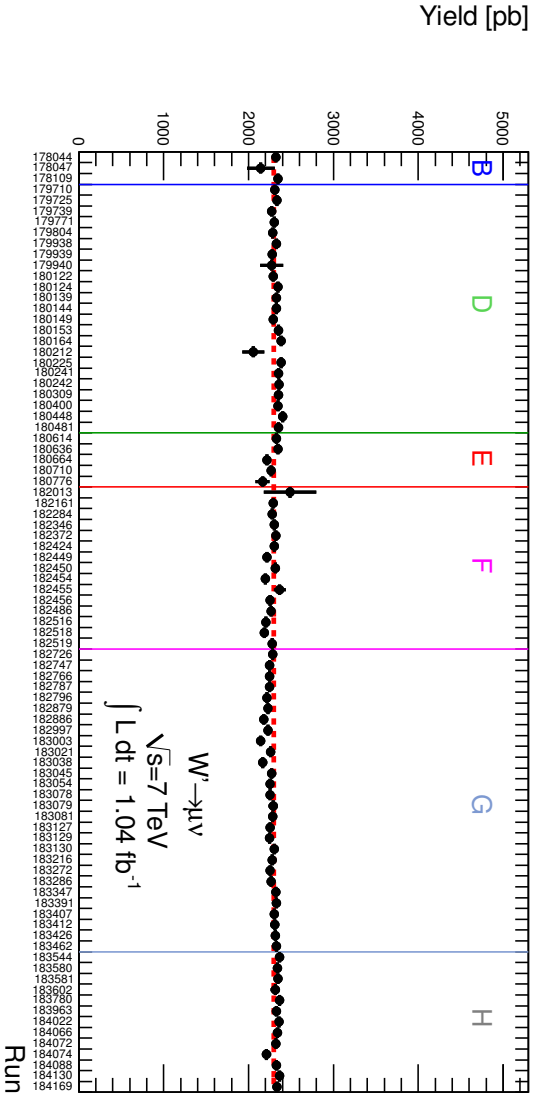

Figure 4.2: Event selection cross section (N_{sel}/L_{int}) for each run. Each letter corresponds to a different data taking period.

The muon p_T, η and ϕ spectrums are shown in Fig. 4.3. In these and all the other kinematical plots, the points represent data and the filled histograms show the stacked backgrounds. The open histograms are $W' \to \mu\nu$ signals added to the background with masses in GeV as indicated in parentheses in the legend. The QCD background estimated from data, as discussed in detail in section 4.6.2.2, is also shown. The signal and other background samples are normalized using the integrated luminosity of the data and the NNLO (approximate-NNLO for $t\bar{t}$) cross sections listed in Table A.2. In all three distributions, the data and MC agreement is good. The slight deficit in data in one side of the barrel is due to a L1 trigger issue, which is well understood and covered by the trigger efficiency measurement uncertainty, as explained in section 4.7.5. The slight fluctuation in the negative side of the ϕ distribution is due to the feet of the detector, which is difficult to simulate perfectly.

The missing transverse energy is calculated using the calorimetric missing transverse energy, the muon momentum and the transverse energy loss of the muon, as given in Eq. 4.2. These distributions are demonstrated in Fig. 4.4. As a result of careful modeling of pile-up in the MC, the data and MC agreement is remarkably good, especially for the E_T^{miss}distribution. The slight deficit at the higher end of the muon E_{Tloss} is not well understood but doesn't have any effect on the final result.

Finally the observable that is used to search for new physics, namely the transverse mass spectrum, is shown in Fig 4.5. As can be seen, like the rest of the distributions, the data and MC agreement is good, unfortunately also in the tail of the spectrum giving not much hope for a hint of new physics. The most dominant background is the SM W production as expected and the Z background is well below that, thanks to a lower production cross section as well as a looser second muon veto. The $t\bar{t}$ and diboson contributions are also low and the QCD contamination is negligible in the high-m_T region that is relevant to this search.

The extraction of signal efficiencies and background expectations, which are used in the final calculation, are discussed in the following sections, namely 4.6.1 and 4.6.2, respectively.

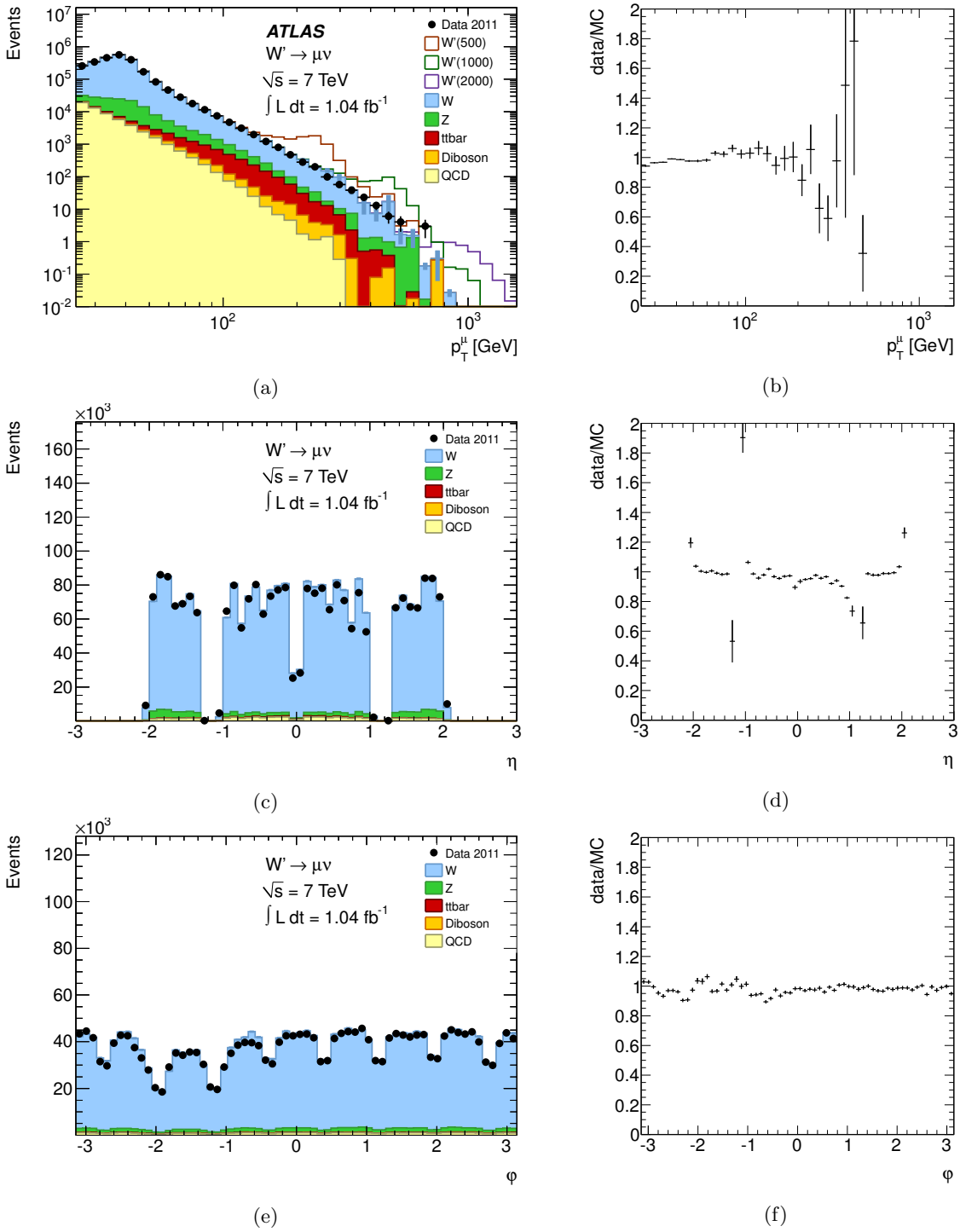

(a) (b) (c) (d) (e) (f)

Figure 4.3: Muon p_T, η and ϕ distributions after all selection cuts, as well as data/MC ratios for each. The QCD (i.e. multi-jet) background is taken from the data driven estimate. The data/MC ratio plots only include the data and the expected background processes.

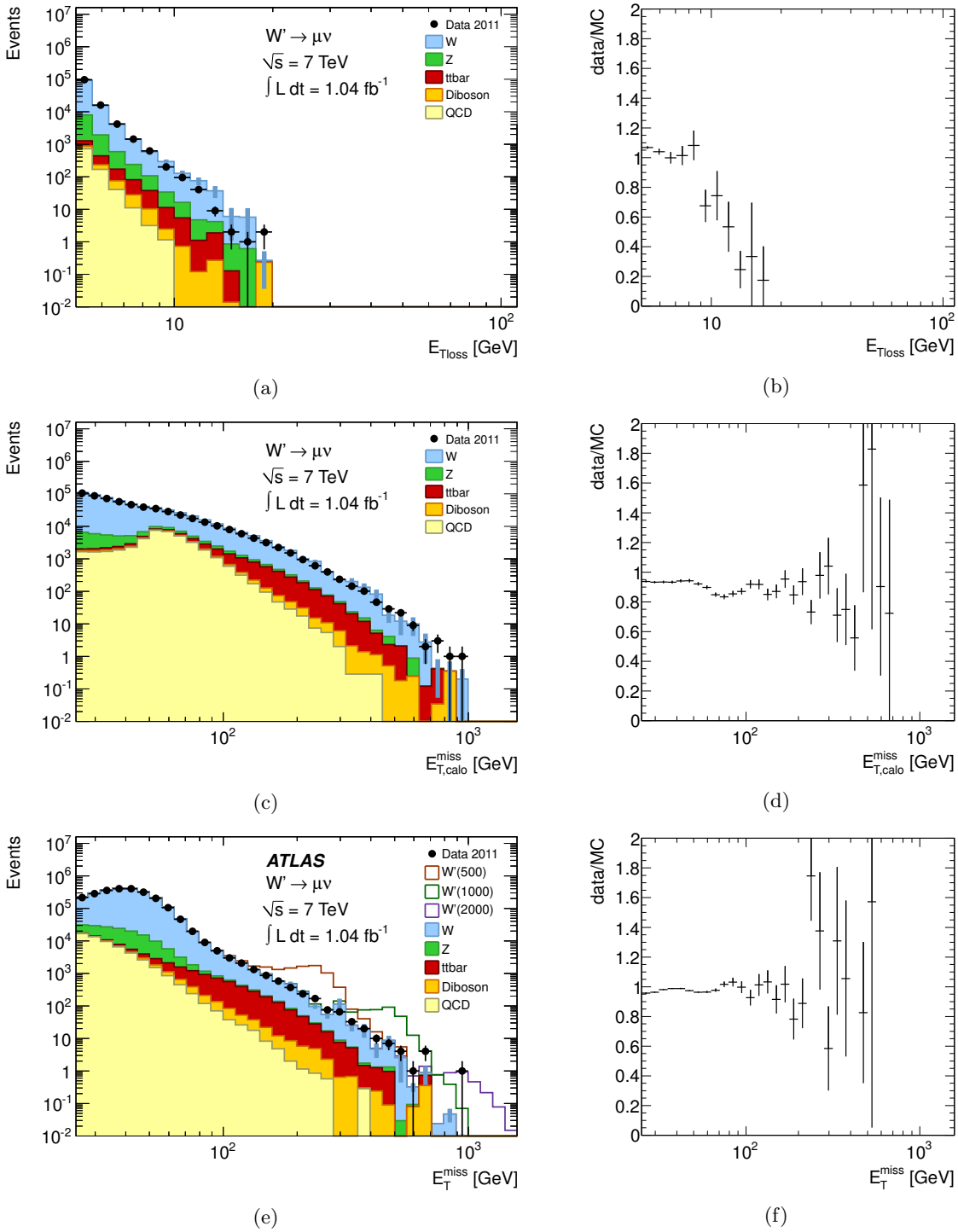

Figure 4.4: Muon E_{Tloss}, $E_{\mathrm{T,calo}}^{\mathrm{miss}}$ and $E_{\mathrm{T}}^{\mathrm{miss}}$ distributions after all selection cuts. The QCD (i.e. multi-jet) background is taken from the data driven estimate. The data/MC ratio plots only include the data and the expected background processes.

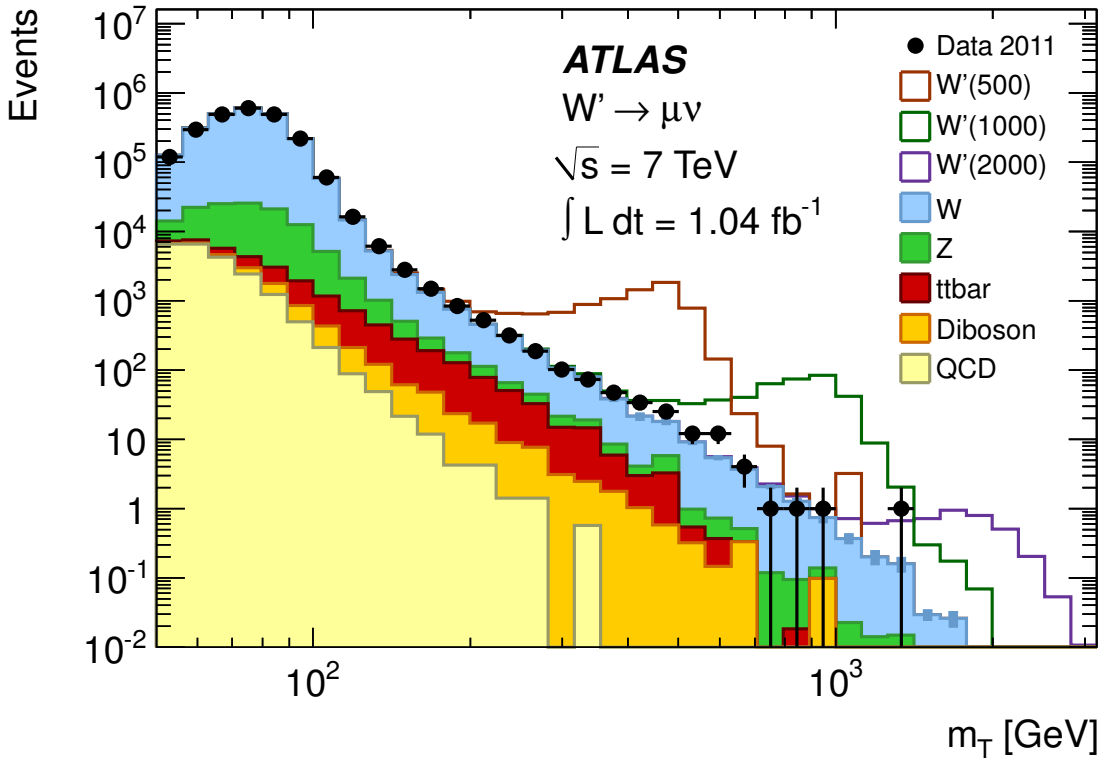

(a)

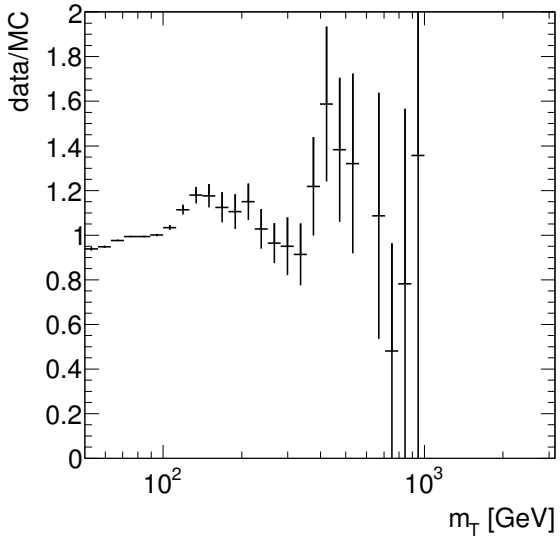

(b)

Figure 4.5: m_T distribution after all selection cuts. The QCD (i.e. multi-jet) background is taken from the data driven estimate. The data/MC ratio plot only includes the data and the expected background processes.

4.6.1 Signal Efficiencies

Table 4.2 summarizes the event selection efficiencies, namely $\epsilon_{\text{sig}}^{\text{MC}}$, for different signal samples of $W' \to \mu\nu$. These are the fractions of events that pass all the selection cuts as well as the m_{Tmin} cut. Note that some mass points use the same m_{Tmin} thresholds. The expected number of events for each sample for the total integrated luminosity are also shown.

$m_{W'}$ [GeV]	m_{Tmin} [GeV]	$\epsilon_{\text{sig}}^{\text{MC}}$	N_{exp}
500	398	$0.235 \pm 2.6\%$	4200
600	447	$0.269 \pm 2.7\%$	2300
750	562	$0.279 \pm 2.4\%$	923
1000	708	$0.311 \pm 2.3\%$	269
1250	794	$0.355 \pm 2.7\%$	95.8
1500	891	$0.359 \pm 3.1\%$	33.0
1750	1000	$0.324 \pm 3.2\%$	10.9
2000	1122	$0.314 \pm 3.3\%$	4.09
2250	1122	$0.295 \pm 2.6\%$	1.61
2500	1122	$0.246 \pm 3.7\%$	0.597

Table 4.2: Uncorrected signal selection efficiencies for each of the Monte Carlo signal samples. The efficiency is for the final selection plus $m_{\text{T}} > m_{\text{Tmin}}$. The last column is the expected number of events for the total integrated luminosity used in this analysis.

4.6.2 Background Estimations

Except for the cosmics and QCD, the expected background levels are evaluated using simulated samples and normalized using the cross sections discussed in section 4.3 and the integrated luminosity of the data. The same reconstruction and event selection are applied to both data and simulated samples. Data driven methods are used to estimate cosmic and QCD backgrounds as discussed in sections 4.6.2.1 and 4.6.2.2 respectively. Both are found to be negligible, hence neglected in the final calculation. These discussions are followed by a summary of the total background expectations in section 4.6.2.3.

4.6.2.1 Cosmic Background Estimation

Background from cosmic ray muons is suppressed via the impact parameter cuts : $d_0^{\mathrm{PV}} <$ 1 mm and $z_0^{\mathrm{PV}} < 5$ mm. Since this background is not well modeled by MC, a data driven approach is used to set an upper limit on its contribution to the total background. For this estimation, the full analysis is run over all data with inverted impact parameter cuts, namely $d_0^{\mathrm{PV}} > 1$ mm and $z_0^{\mathrm{PV}} > 5$ mm. A total of 126 events passed all the selection cuts for about 1 fb^{-1}, and the d_0 vs z_0 distribution of these events is shown in Fig. 4.6.

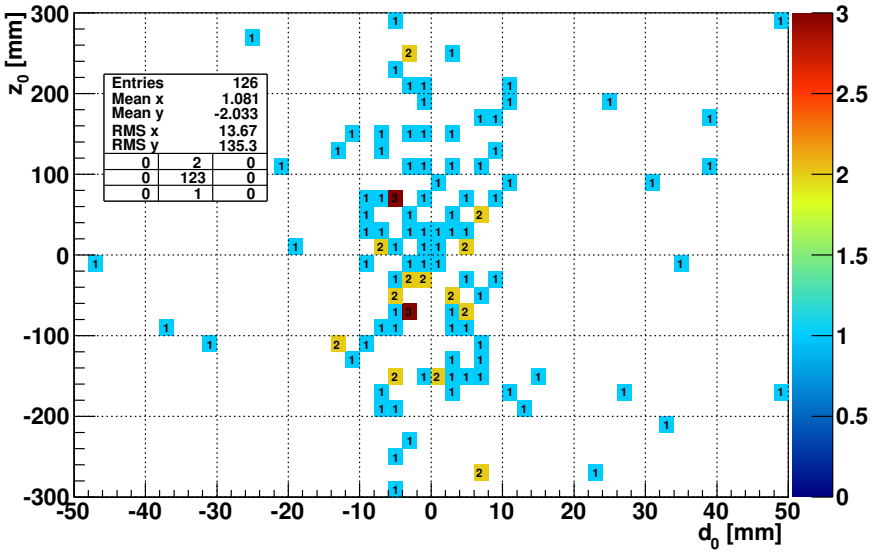

Figure 4.6: Distribution of d_0 vs z_0 with inverted impact parameter cuts.

Four d_0-z_0 regions are used to evaluate the expected cosmic background spectrum normalized to the relative areas of the selection and evaluation regions. These estimates are summarized in Table 4.3. As can be seen, all four measurements are consistent with each other and in light of these the cosmic background after all cuts except the $\mathrm{m_{Tmin}}$ is estimated to be $0.17 \pm 0.03(\mathrm{stat}) \pm 0.05(\mathrm{sys})$, which is negligible compared to the other background sources and is therefore ignored in the final calculation.

Region	$N_{observed}$	$N_{calculated}$
2 mm $< \lvert d_0^{PV} \rvert <$ 15 mm & $\lvert z_0^{PV} \rvert <$ 150 mm	64	0.16 ± 0.02
5 mm $< \lvert d_0^{PV} \rvert <$ 15 mm & $\lvert z_0^{PV} \rvert <$ 150 mm	36	0.12 ± 0.02
2 mm $< \lvert d_0^{PV} \rvert <$ 15 mm & 50 mm $< \lvert z_0^{PV} \rvert <$ 150 mm	44	0.17 ± 0.03
5 mm $< \lvert d_0^{PV} \rvert <$ 15 mm & 50 mm $< \lvert z_0^{PV} \rvert <$ 150 mm	26	0.13 ± 0.03

Table 4.3: The cosmic background estimates in different regions. The region parameters are given in the first column. The second column gives the total number of observed events in each region, and the third gives the extrapolated number of events into the signal region.

4.6.2.2 QCD Background Estimation

Due to limited statistics, relatively high theoretical cross section uncertainties and imperfect fragmentation/hadronization models, it is not preferable to use MC predictions for the QCD background estimation. Therefore this analysis adopts a data driven estimation for this background. In this method, events are selected as described in sections 4.4 and 4.5.3 but with the exclusion of the muon isolation cut. The main QCD contamination in the muon channel is from heavy flavor decays, i.e. $b\bar{b}$ and $c\bar{c}$ production, where one of the quarks decays into a muon and an energy mis-measurement gives rise to some missing transverse energy. This combination can mimic the signal. In such events, the muon is mostly expected to be very close to a jet, or in other words not isolated. Hence, in order to obtain a QCD-enriched data sample, the isolation cut is reversed, so that only events that have $0.2 < p_T^{cone30}/p_T < 0.4$ are considered. These events are then assumed to have the same kinematical distributions in the signal region, apart from a scale factor, which is separately determined by fitting templates of the E_T^{miss} distribution to the E_T^{miss} spectrum in data. More details on this method can be found in [45].

One caveat to this method is the lack of data in the high-m_T region, where the $W' \to \mu\nu$ limit is set. To obtain an estimate of the background in this region, a power law fit and extrapolation technique is used, as shown in Figure 4.7. In order not to bias the fit due to absence of data in the region of interest, we performed an unbinned likelihood fit using the pdf form:

$$f(\mathrm{m_T}; C, a) = C\mathrm{m_T}^a \tag{4.6}$$

where a determines the slope, and C determines the normalization of the fit. The expected contamination from the SM W into the QCD enriched sample in the fit region is estimated to be $\sim 5\%$, and has marginal effect on the measurement. Therefore, we did not attempt to perform any background subtraction. One important aspect of such a fit is to assess the response of the expected number of events to varying the fit ranges. To quantify this effect the fit is performed in three different $\mathrm{m_T}$ regions. The corresponding expected number of QCD events are quoted in Table 4.4.

$\mathrm{m_{Tmin}}$ [GeV]	$\mathrm{m_T} > 160$ GeV	$\mathrm{m_T} > 165$ GeV	$\mathrm{m_T} > 170$ GeV
398	$0.32^{+0.23}_{-0.14}$	$0.32^{+0.23}_{-0.14}$	$0.26^{+0.22}_{-0.13}$
447	$0.21^{+0.17}_{-0.10}$	$0.21^{+0.17}_{-0.10}$	$0.16^{+0.16}_{-0.09}$
562	$0.09^{+0.09}_{-0.05}$	$0.09^{+0.09}_{-0.05}$	$0.07^{+0.09}_{-0.04}$
794	$0.02^{+0.03}_{-0.02}$	$0.02^{+0.03}_{-0.01}$	$0.02^{+0.03}_{-0.01}$
891	$0.01^{+0.02}_{-0.01}$	$0.02^{+0.02}_{-0.01}$	$0.01^{+0.02}_{-0.01}$
1000	$0.01^{+0.02}_{-0.01}$	$0.01^{+0.02}_{-0.01}$	$0.01^{+0.02}_{-0.01}$
1122	$0.01^{+0.01}_{-0.00}$	$0.01^{+0.01}_{-0.00}$	$0.00^{+0.01}_{-0.00}$

Table 4.4: QCD background estimates in different fit regions.

Figure 4.7 shows that, especially in the high-$\mathrm{m_T}$ region, the major contribution to the overall uncertainty is coming from the slope, with a relative uncertainty of $\sim 20\%$. In principal the slope is the only free parameter in the fit since the normalization is determined by the fact that the integral of the pdf over the full range of the variable should equal unity. However, to be more conservative we further assigned a fractional error of $1/\sqrt{N}$ to the overall normalization, motivated by the counting error on N itself. Table 4.4 shows that the expectations derived using different fit regions agree within their uncertainties. As in the cosmic background case, the contribution of QCD to the total background is found to be negligible. Hence not used in the final limit calculation.

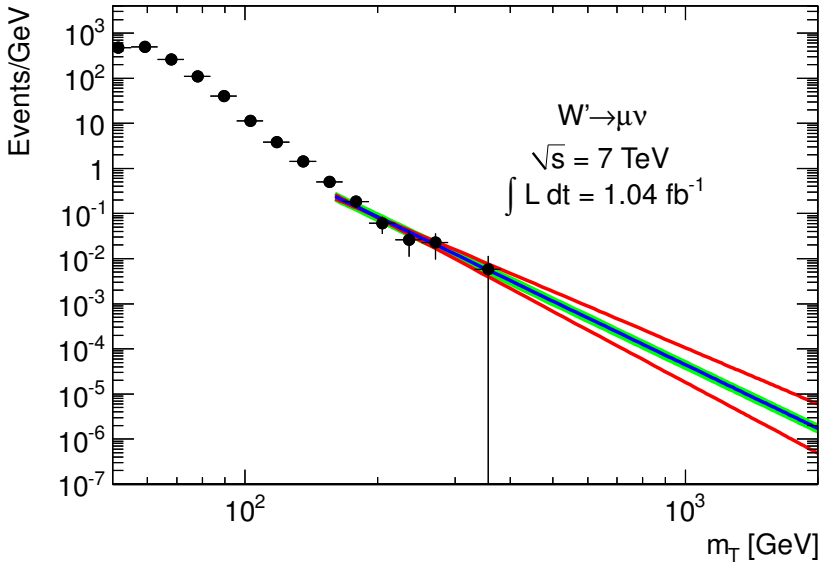

(a)

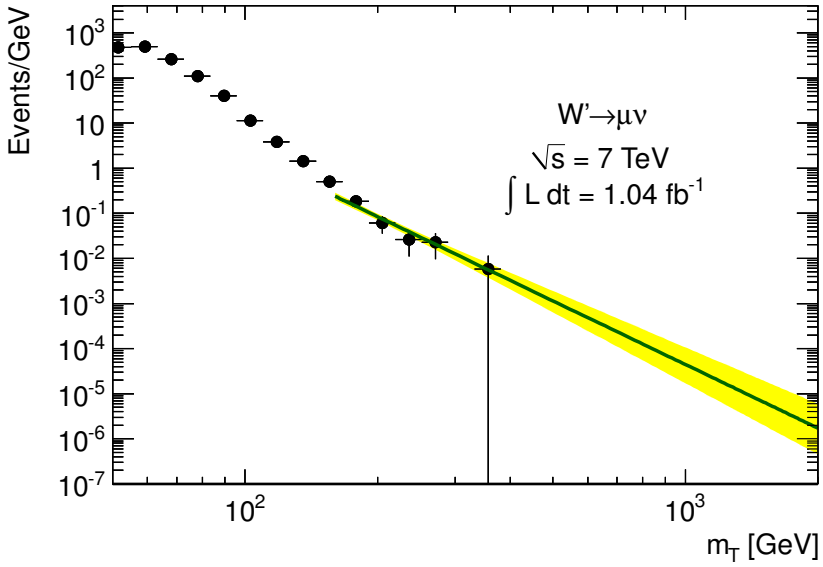

(b)

Figure 4.7: QCD background estimates in the muon channel as described in the text, as a function of m_T. (a) shows the different error components, where the red curves represent the effect of varying the slope by its error, and the green curves for varying the overall normalization by a fractional error of $1/\sqrt{N}$. (b) has the error band for the combination of these in quadrature.

4.6.2.3 Total Background Estimation

Table 4.5 summarizes the total number of expected background events for the full luminosity and the individual contributions from each background process. As can be seen, the $t\bar{t}$ sample runs out of statistics in the highest search bins, but this does not affect the final results as the major contribution comes form the other EWK processes. In the low mass bins, i.e. 398 GeV, there is an observed excess in data, which is also visible in the transverse mass spectrum in Fig. 4.5. This excess manifests itself in three out of the first four bins, but there is good agreement in the high end tail of the m_T distribution. The probability that this is a statistical fluctuation will be discussed in section 4.9. The event display for the highest-m_T candidate is shown in Fig. 4.8 and a more detailed cut flow chart for data is presented in section 4.6.3.

m_{Tmin} [GeV]	N_W	N_Z	$N_{diboson}$	$N_{t\bar{t}}$	N_{BG}	N_{obs}
398	50.1 ± 3.4	4.89 ± 0.96	2.52 ± 0.60	5.1 ± 1.3	62.6 ± 3.8	91
447	32.7 ± 2.0	3.80 ± 0.96	1.49 ± 0.44	3.16 ± 1.01	41.2 ± 2.4	57
562	12.37 ± 0.41	0.834 ± 0.055	0.59 ± 0.28	0.23 ± 0.39	14.03 ± 0.64	20
708	4.49 ± 0.24	0.288 ± 0.016	0.114 ± 0.083	0.0106 ± 0.0106	4.90 ± 0.26	4
794	2.53 ± 0.18	0.1689 ± 0.0096	0.114 ± 0.083	0.0106 ± 0.0106	2.82 ± 0.20	3
891	1.342 ± 0.128	0.0931 ± 0.0048	0.106 ± 0.082	0.0 ± 0.0	1.541 ± 0.152	2
1000	0.745 ± 0.091	0.0512 ± 0.0026	0.0079 ± 0.0079	0.0 ± 0.0	0.804 ± 0.092	1
1122	0.397 ± 0.064	0.0284 ± 0.0016	0.0079 ± 0.0079	0.0 ± 0.0	0.433 ± 0.065	1

Table 4.5: Uncorrected background event counts with $L_{int} = 1.04\ fb^{-1}$ for each of the Monte Carlo background samples (W, Z, diboson and $t\bar{t}$), and their sum. The last column gives the number of events observed in data.

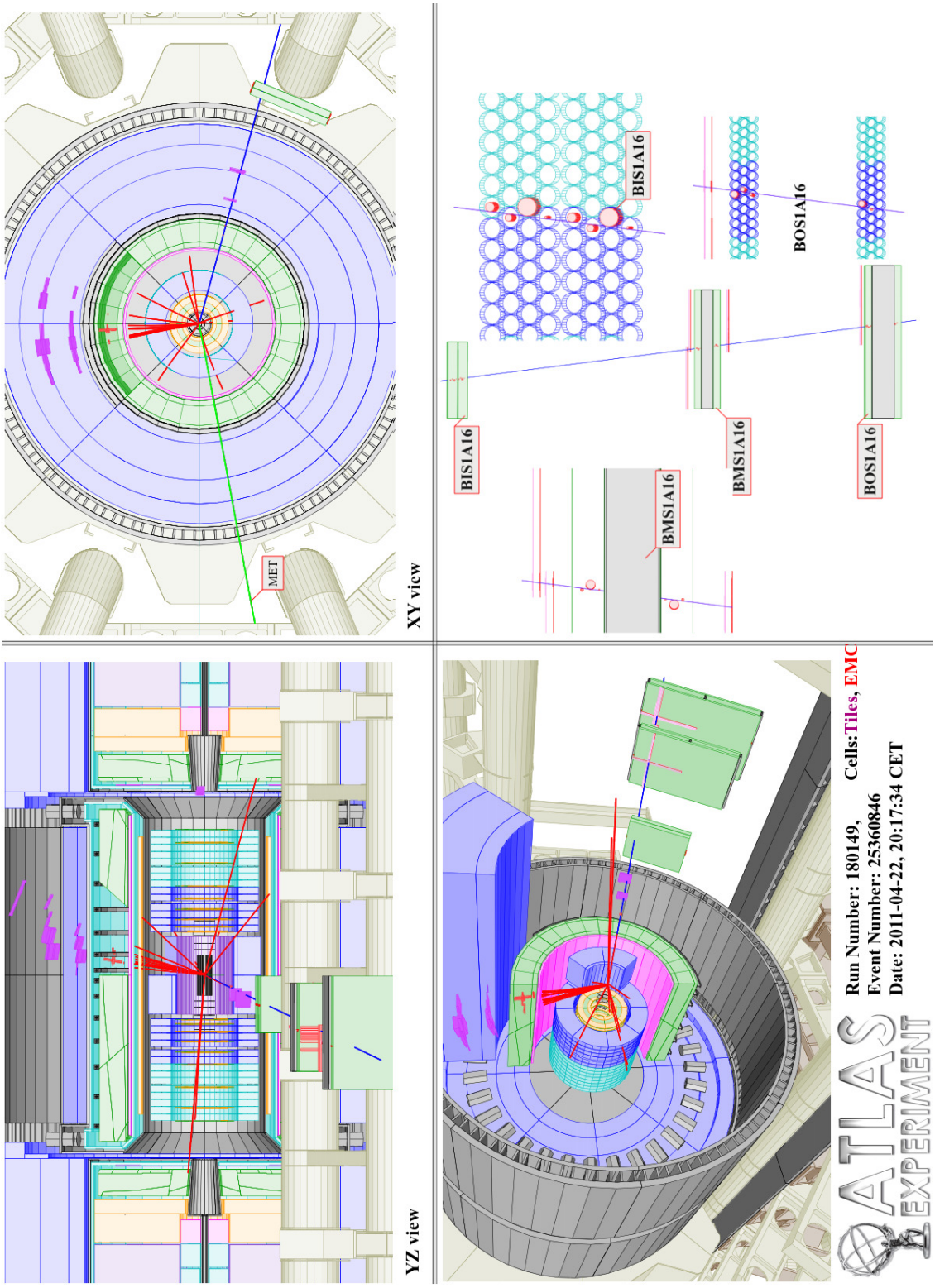

Figure 4.8: Highest-m_T event (m_T = 1350 GeV) observed in data. Side (top left), end (top right) and three-dimensional (bottom left) views are shown. The muon (blue) has $p_T = 695$ GeV and the E_T^{miss} (green) is 680 GeV. The recoiling jet has $p_T = 330$ GeV. The bottom right detail shows the muon has all the expected hits.

4.6.3 Data Cut Flow

Table 4.6 summarizes the cut flow of event/object selection in data.

Cut	Number of events	Cut Efficiency (Relative)	Selection Efficiency (Cumulative)
Total	136,709,631	$(100.0 \pm 0.0)\%$	$(100.0 \pm 0.0)\%$
Skim/Slim	30,039,843	$(22.0 \pm 0.0)\%$	$(22.0 \pm 0.0)\%$
GRL	25,230,064	$(84.0 \pm 0.0)\%$	$(18.5 \pm 0.0)\%$
Trigger	20,094,343	$(79.6 \pm 0.0)\%$	$(14.7 \pm 0.0)\%$
Vertex cut	20,057,091	$(99.8 \pm 0.0)\%$	$(14.7 \pm 0.0)\%$
CB Muon p_T >25 GeV	12,271,519	$(61.2 \pm 0.0)\%$	$(8.98 \pm 0.00)\%$
ID hits	12,088,969	$(98.5 \pm 0.0)\%$	$(8.84 \pm 0.00)\%$
Impact par. cuts	12,002,619	$(99.3 \pm 0.0)\%$	$(8.78 \pm 0.00)\%$
MS hits	8,332,392	$(69.4 \pm 0.0)\%$	$(6.09 \pm 0.00)\%$
Trigger match	8,228,920	$(98.8 \pm 0.0)\%$	$(6.02 \pm 0.00)\%$
Isolation	3,584,030	$(43.6 \pm 0.0)\%$	$(2.62 \pm 0.00)\%$
Exactly 1 μ	3,472,720	$(96.9 \pm 0.1)\%$	$(2.54 \pm 0.00)\%$
Looser 2^{nd} μ veto	3,284,223	$(94.6 \pm 0.1)\%$	$(2.40 \pm 0.00)\%$
Jet cleaning	3,270,692	$(99.6 \pm 0.1)\%$	$(2.39 \pm 0.00)\%$
E_T^{miss}> 25 GeV	2,416,512	$(73.9 \pm 0.0)\%$	$(1.77 \pm 0.00)\%$
$\lvert S_{\Delta(q/p)_{ID-MS}} \rvert < 5$	2,383,254	$(98.6 \pm 0.1)\%$	$(1.74 \pm 0.00)\%$

Table 4.6: Muon cut flow for the data, as well as the relative and cumulative selection efficiencies for all the cuts.

Table 4.6 gives the detailed cut flow summary for the entire dataset that corresponds to $L_{int} = 1.04\ fb^{-1}$. The first step, called "Skim/Slim", is the process where the data is skimmed and slimmed by requiring at least one combined STACO muon with $p_T > 10$ GeV in order to reduce the file sizes so that the computation can be made faster. This is a necessary step as the analysis has to be repeated many times. These events are collected in special data streams called *physics* streams, where the sampling is based on primary physics triggers. However, during online data taking, if an event has an error such as a timeout while running the trigger algorithms, etc., it is recorded in a special stream called the *debug* stream. These events are then re-analyzed in the offline environment to spot and possibly fix the problem(s). It is essential to run the full analysis chain over this stream as well as the physics stream to make

sure we do not miss any signal-like events. Only one event passing all the selection cuts is found in the debug stream and an event display for this event can be seen in Fig. 4.9. The m_T in this event is $\sim$ 70 GeV and is consistent with a SM W. It therefore has no effect on the search.

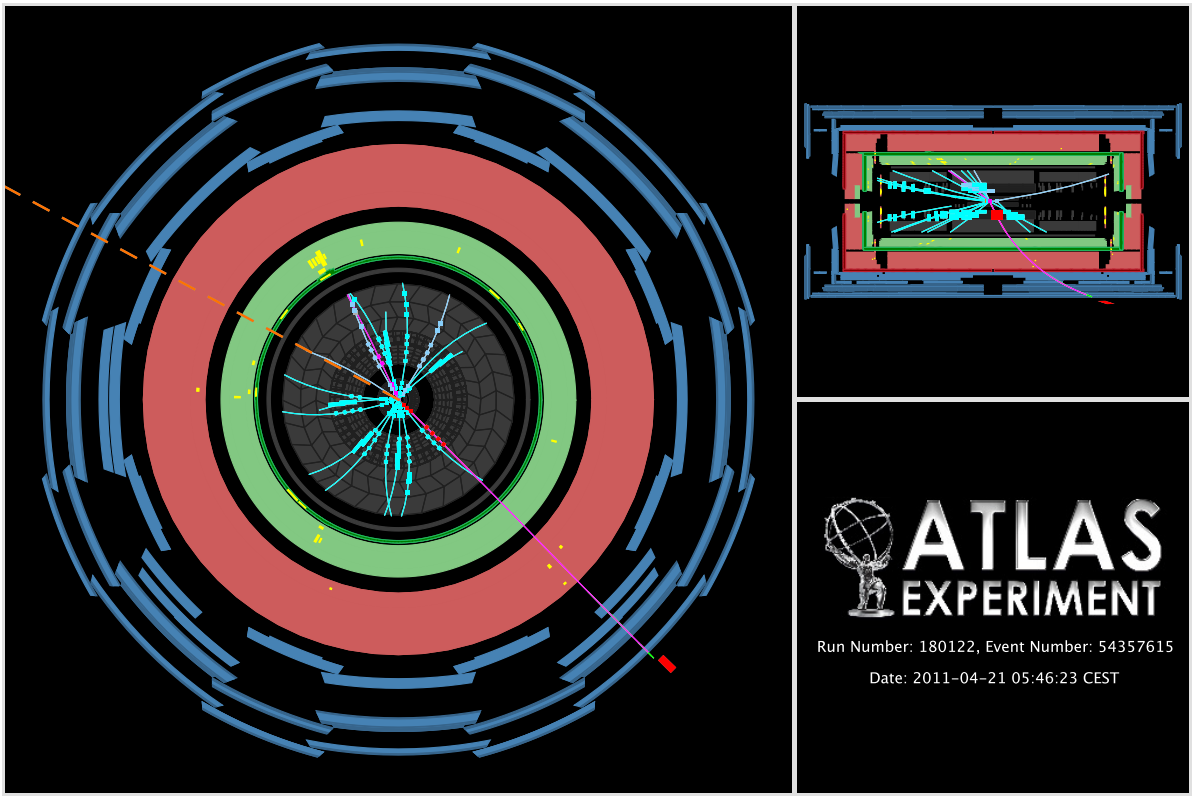

Figure 4.9: Event display for the only event ($m_T = 70$ GeV) found in the debug stream passing all the selection cuts. End (left) and side (top right) views of the event are shown. The muon (purple) has $p_T = 46$ GeV and the E_T^{miss} (dashed) is 30 GeV. Inner detector tracks with $p_T > 1$ GeV are shown.

Also, 91 events that pass the lowest threshold cut for the limit calculation, which can be seen in Table 4.5, are also cross checked for possible double counting and no such occurrence is found. A detailed list of these events can be found in Table B.1 in the appendix.

4.7 Systematic Corrections and Uncertainties

The discovery significance as well as the limit extraction depends on the signal selection efficiencies and background estimates which are discussed in sections 4.6.1 and 4.6.2, respectively. This section shall:

- Assess the factors that correct for biases in MC with respect to data
- Evaluate sources of systematic uncertainties in the measurements and propagate those to uncertainties on the selection efficiency and background level

Only those uncertainties that have a significant effect are discussed. Among those that are not explicitly discussed below are: the efficiencies to pass the vertex identification, impact parameter and $S_{\Delta(q/p)_{\mathrm{ID-MS}}}$ selection criteria. In all cases, the efficiency in Monte Carlo is over 99% and is expected to be similar in data, as demonstrated in Table 4.6. So the associated systematic uncertainty would be well under 1% and is thus negligible. The reader should also recall that the QCD and cosmic backgrounds are neglected since they are greatly suppressed compared to other background sources.

4.7.1 Muon Identification Efficiency

The measurement of the muon identification efficiency is divided into three parts as: combined muon reconstruction efficiency, inner detector muon efficiency and muon hit efficiency. These are then combined with the muon isolation efficiency to obtain a total muon selection efficiency, as discussed in section 4.7.3. In order to have an unbiased sample for these measurements, a method called Tag&Probe is used. According to this method, events are examined to first find a *tag* and *probe* combination. In case of success, the probe is examined to see if it satisfies a set of predefined requirements. The definitions of tags and probes, as well as the requirements that the probe has to meet are specific to the measurement and will be explained in each subsection.

The efficiency, namely the probability that a probe meets the requirements, is defined as:

$$\epsilon = \frac{\text{\# of successes}}{\text{\# of trials}}. \tag{4.7}$$

It should be noted that in this case, the number of trials is the total number of tag-probe combinations, and a success is a case where the probe under consideration meets the necessary criteria. By construction, an object can be a tag and a probe, and an event can be double counted. Taking this into account is very important so as to not bias the measurement. Each measurement is also assigned a binomial statistical error.

All three efficiencies mentioned above are calculated both in MC and data, then a correction factor, $C_X^{\mu} = \frac{\epsilon_X(\text{Data})}{\epsilon_X(\text{MC})}$, is calculated for each. These are then combined to get an overall MC to data correction factor for the muon identification. This is discussed in section 4.7.1.4.

4.7.1.1 Combined Muon Reconstruction Efficiency

For the combined muon reconstruction efficiency, the tag is a muon candidate that satisfies all the offline muon selection criteria explained in section 4.5.3. A probe, on the other hand, is an ID track satisfying the following criteria:

- $\mathrm{p_T} > 25$ GeV
- $|\eta| < 2.5$
- $\mathrm{d_0^{PV}} < 1$ mm & $\mathrm{z_0^{PV}} < 5$ mm
- $\mathrm{p_T^{cone30}}/\mathrm{p_T} < 0.05$

Moreover, in order to select an enriched $Z \to \mu\mu$ sample and reject QCD, the following cuts are also applied to the tag-probe system:

- $\mathrm{q}_{\mu} = -\mathrm{q}_{\mathrm{track}}$
- $|\Delta\phi_{\mu-\mathrm{track}}| \geq 2$
- $\mathrm{p_T^{\mu-track}} \leq 65$ GeV

- $75\ \text{GeV} \leq \text{M}_{\mu-\text{track}} \leq 105\ \text{GeV}$
- $\text{E}_{\text{T}}^{\text{miss}} \leq 35\ \text{GeV}$

Then for each tag-probe combination that fulfills the requirements, all possible combined muons in the event are analyzed to see if at least one of them matches the probe. The matching criteria requires a combined muon satisfying $\Delta R_{\text{probe}-\text{CB }\mu} < 0.01$.

In MC the efficiency is measured to be $(96.7 \pm 0.0)\%$, and in data to be $(94.5 \pm 0.1)\%$, where errors are statistical only. Figure 4.10 shows the combined muon reconstruction efficiency as a function of the muon p_{T} and η. The high efficiency loss around $\eta \approx 0$ and ± 1.2 is due to limited detector coverage.

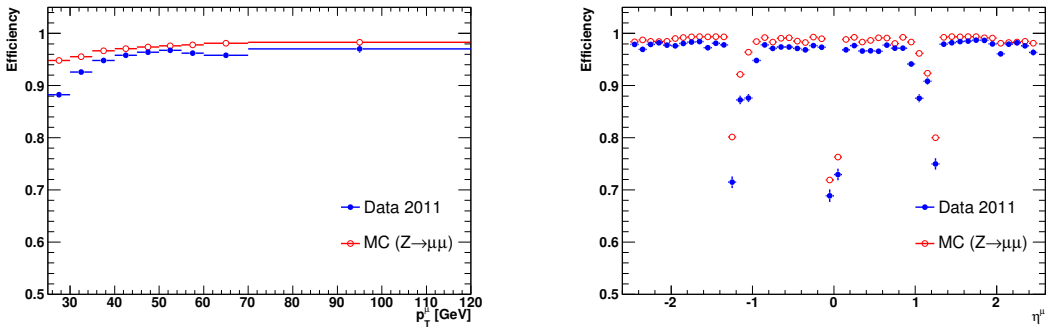

(a) (b)

Figure 4.10: Combined muon reconstruction efficiency as a function of muon p_{T} and η.

The uncertainty is estimated by varying the Z mass window cut, and the results are quoted in Table 4.7. The measured correction is $C_{\text{CB}}^{\mu} = 0.978 \pm 0.001(\text{stat}) \pm 0.004(\text{sys})$.

Invariant Mass Window	ϵ_{CB}(Data)	ϵ_{CB}(MC)	Ratio
$[70, 100]$ GeV	$(94.94 \pm 0.08)\%$	$(96.73 \pm 0.01)\%$	0.981 ± 0.001
$[75, 105]$ GeV	$(94.54 \pm 0.08)\%$	$(96.67 \pm 0.01)\%$	0.978 ± 0.001
$[80, 100]$ GeV	$(94.14 \pm 0.08)\%$	$(96.61 \pm 0.01)\%$	0.974 ± 0.001

Table 4.7: ϵ_{CB} and the correction factor, C_{CB}^{μ}, measurements for different mass windows.

4.7.1.2 Inner Detector Muon Efficiency

The definition of tag objects for this measurement is exactly the same as in the combined muon reconstruction efficiency measurement. The probe, however, is a MS track extrapolated to the beam line that satisfies the following criteria:

- $p_T > 25$ GeV
- $N_{hits}^{MDT} > 2$ (in each of the three stations)
- $N_{hits}^{RPC/TGC,\phi-layer} > 1$ (in each of at least two of the three RPC/TGC layers)
- No barrel-endcap overlap, no poorly alligned chamber hits, i.e. BEE, EE and BIS78
- $N_{hits}^{CSC,\eta} = 0$

Moreover, as for the combined muon reconstruction efficiency measurement, in order to select an enriched $Z \to \mu\mu$ sample, the following cuts are also applied to the tag-probe system:

- $q_\mu = -q_{MS}$
- $|\Delta\phi_{\mu-MS}| \geq 2$
- $p_T^{\mu-MS} \leq 65$ GeV
- 75 GeV $\leq M_{\mu-MS} \leq 105$ GeV

Then for each tag-probe combination, all possible ID tracks in the event are analyzed to determine whether at least one of them matches the probe. The matching criteria selects an ID track that satisfies $\Delta R_{\text{probe}-\text{ID track}} < 0.01$ that also matches to a combined muon. The efficiency in MC is measured to be $(100.0 \pm 0.0)\%$, and $(99.9 \pm 0.0)\%$ in data. In order to quantify the systematic fluctuations, the measurement is performed for different matching cones (0.005, 0.01, 0.02) and different run periods. The variations are found to be $\leq 0.3\%$ both in MC and data. Finally, the corresponding correction factor between data and MC is found to be $C_{ID}^{\mu} = 0.999 \pm 0.000(\text{stat}) \pm 0.003(\text{sys})$.

4.7.1.3 Muon Hit Efficiency

The tag definition for this measurement is identical to the previous two. A probe, on the other hand, is a combined muon that satisfies all criteria explained in section 4.5.3 except for the ID and MS hit requirements. In order the reject background as much as possible, as in the previous cases, the tag and probe are required to have opposite charge, be within the Z mass window of $[75, 105]$ GeV, and be back to back by requiring $|\Delta\phi_{\mathrm{tag-probe}}| \geq 2$, and $\mathrm{p_T^{tag-probe}} \leq 65$ GeV.

Given that all these criteria are satisfied, the ID and MS hit requirements explained in section 4.5.3 are then imposed on the probe and the probability of it passing these additional criteria is measured. This efficiency is measured to be $(69.4 \pm 0.0)\%$ in MC and $(69.7 \pm 0.2)\%$ in data. The $\mathrm{p_T}$, η and ϕ dependences are shown in Fig. 4.12. As can be seen, the MC can reproduce the data with good accuracy. Most of the efficiency loss is coming from:

- $|\eta| \approx 0$ and 1.2, due to missing stations
- $|\eta| > 2$, due to not using the CSC region
- $\phi \approx -1$ and -2, due to the feet of the detector

Fig. 4.11 shows the η-ϕ distribution of muons for events that pass all the selection criteria, except the $\mathrm{m_{Tmin}}$ cut, and demonstrates the acceptance of the MS hit selection criteria.

The uncertainty is estimated by varying the Z mass window cut, and the results are quoted in Table 4.8. The measured correction factor is $C^{\mu}_{\mathrm{Hit}} = 1.005 \pm 0.002(\mathrm{stat}) \pm 0.009(\mathrm{sys})$.

Invariant Mass Window	ϵ_{Hit}(Data)	ϵ_{Hit}(MC)	Ratio
$[65, 115]$ GeV	$(69.05 \pm 0.18)\%$	$(69.36 \pm 0.04)\%$	0.996 ± 0.002
$[75, 105]$ GeV	$(69.71 \pm 0.19)\%$	$(69.35 \pm 0.04)\%$	1.005 ± 0.002
$[80, 100]$ GeV	$(70.53 \pm 0.20)\%$	$(69.92 \pm 0.04)\%$	1.009 ± 0.002

Table 4.8: ϵ_{Hit} and the correction factor C^{μ}_{Hit} measurements for different mass windows.

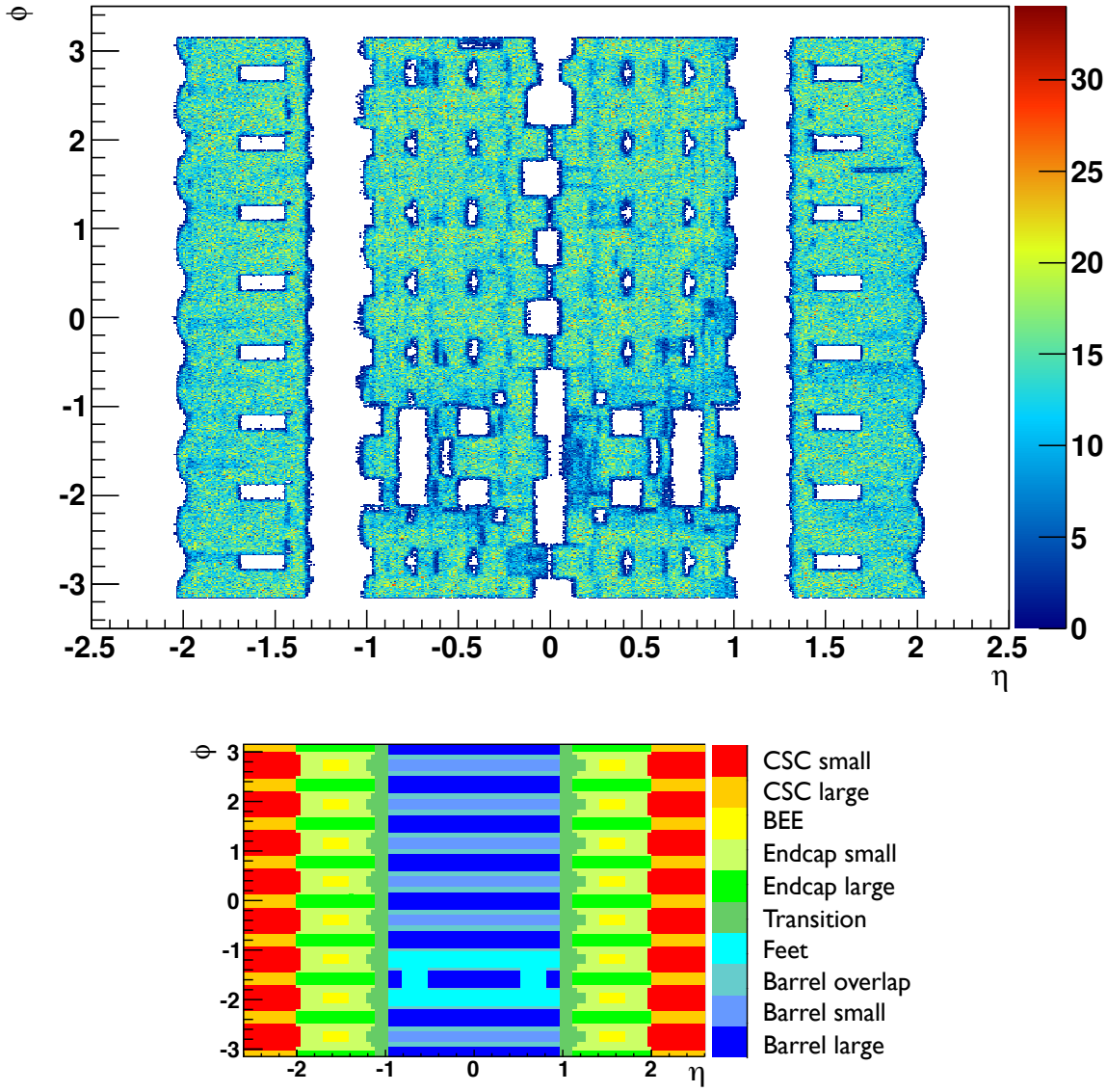

Figure 4.11: Above is the η-ϕ distribution of muons for events that pass all selection cuts, except $m_{T\min}$, in the data. Below is the summary of ten different MS detector regions as shown in Fig. 2.8.

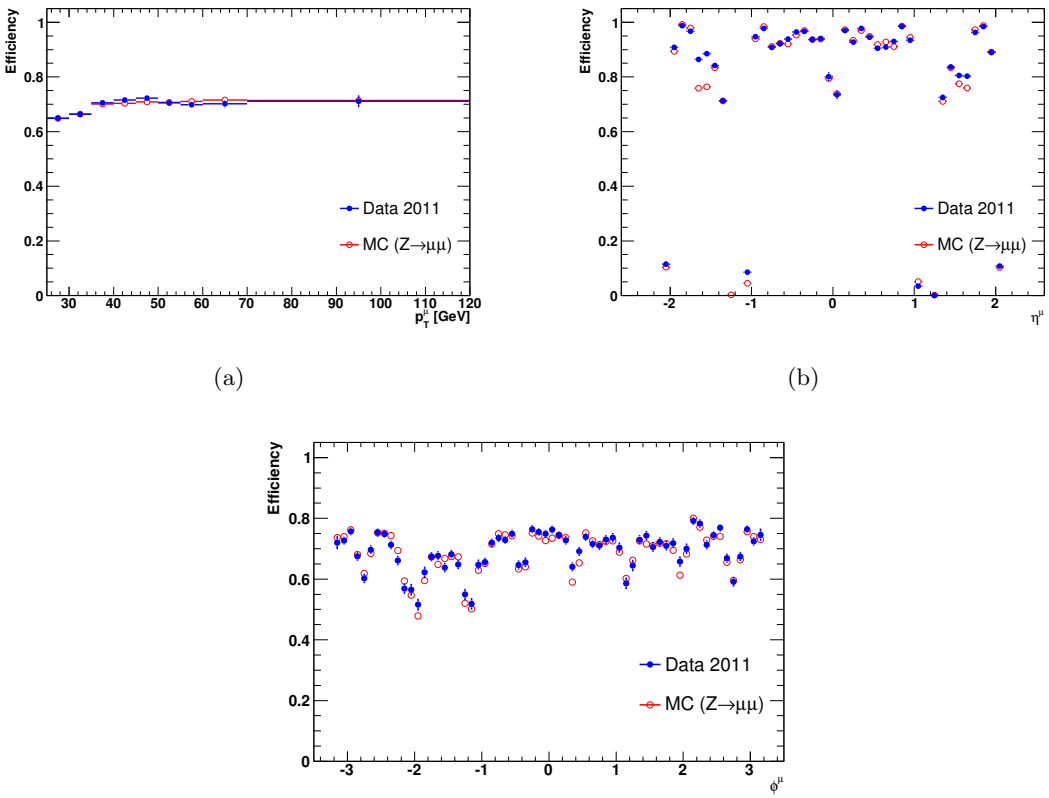

(a)

(b)

(c)

Figure 4.12: Muon hit efficiency as a function of muon p_T, η and ϕ.

4.7.1.4 Total Muon Identification Efficiency

The overall muon identification efficiency is calculated according to the following equation:

$$C^{\mu}_{\text{reco}} = C^{\mu}_{\text{CB}} \times C^{\mu}_{\text{ID}} \times C^{\mu}_{\text{Hit}} \tag{4.8}$$

Table 4.9 summarizes the contributions from each individual measurement as well as the overall correction factor. The measurements are assumed to be uncorrelated and therefore the errors are added in quadrature.

Source	Correction Factor
CB	$0.978 \pm 0.001(\text{stat}) \pm 0.004(\text{sys})$
ID	$0.999 \pm 0.000(\text{stat}) \pm 0.003(\text{sys})$
Hit	$1.005 \pm 0.002(\text{stat}) \pm 0.009(\text{sys})$
All	$0.982 \pm 0.002(\text{stat}) \pm 0.010(\text{sys})$

Table 4.9: Individual contributions to the overall muon identification correction factor.

4.7.2 Muon Isolation Efficiency

The muon isolation efficiency is also measured using the Tag&Probe method discussed in section 4.7.1. The tag is required to pass all the offline muon selection cuts, whereas the probe is required to pass all except the isolation cut. Then the probability of probe passing the isolation cut is measured. The efficiency is measured to be $(96.9 \pm 0.0)\%$ in MC and $(96.5 \pm 0.1)\%$ in data. Figure 4.13 shows the muon isolation efficiency as a function of muon p_T and η and demonstrates the agreement between data and MC. Most of the inefficiency is limited to the low-p_T region and the cut is fully efficiency in the high-p_T region that is of interest to this analysis, mainly due to the fact that a relative isolation is used. There is also not a strong angular dependence.

As can be seen on Table 4.10, the efficiencies increase both in data and MC as the cut becomes looser for the same cone size and as the cone size gets smaller for the same cut value.

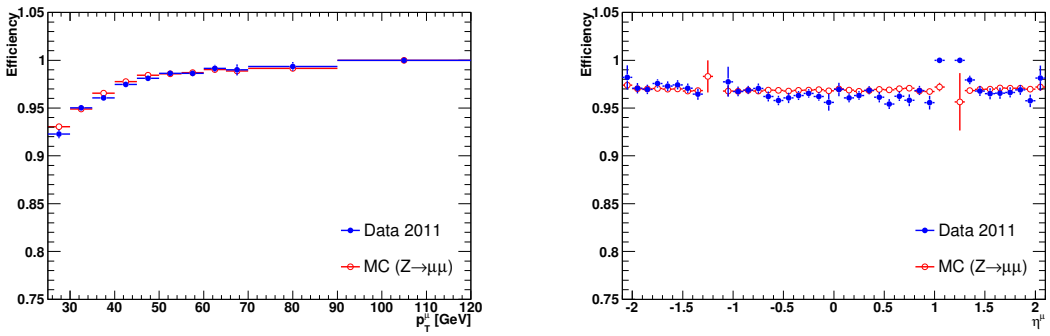

(a) (b)

Figure 4.13: Muon isolation efficiency as a function of muon p_T and η.

Isolation cone size	Isolation cut	ϵ_{Isol}(Data)	ϵ_{Isol}(MC)	Ratio
0.2	0.05	$(98.35 \pm 0.06)\%$	$(98.49 \pm 0.01)\%$	0.999 ± 0.001
0.2	0.15	$(99.70 \pm 0.03)\%$	$(99.72 \pm 0.01)\%$	1.000 ± 0.000
0.3	0.05	$(96.53 \pm 0.09)\%$	$(96.90 \pm 0.02)\%$	0.996 ± 0.001
0.3	0.15	$(99.42 \pm 0.04)\%$	$(99.43 \pm 0.01)\%$	1.000 ± 0.000
0.4	0.05	$(93.79 \pm 0.12)\%$	$(94.59 \pm 0.02)\%$	0.991 ± 0.001
0.4	0.15	$(98.91 \pm 0.05)\%$	$(98.96 \pm 0.01)\%$	1.000 ± 0.001

Table 4.10: ϵ_{Isol} and the correction factor C^{μ}_{Isol} measurements for different isolation cone sizes and cut values.

The correction factor is measured to be $C^{\mu}_{\text{Isol}} = 0.996 \pm 0.001(\text{stat}) \pm 0.004(\text{sys})$, signifying a very good data to MC agreement.

4.7.3 Total Muon Selection Efficiency

The total muon selection efficiency is the combination of the muon identification and isolation efficiencies. The associated correction factors are 0.982 ± 0.010(stat + sys) and 0.996 ± 0.004(stat+sys), respectively, and result in a combined value of 0.978 ± 0.011(stat+sys).

4.7.4 Muon Efficiency Extrapolation to High-p_T

The muon reconstruction efficiency is expected to suffer some loss in the high-p_T region due to increasing radiative losses. Observing this effect in data is impossible due to the lack of very high-p_T muons. Therefore, we rely on MC for this measurement. Another challenge is that as the p_T of the muons get harder, they are more likely to be created around $\eta \sim 0$. This results in a significant drop in the efficiency due to the stringent requirement of having hits in all three layers of the MS. This effect is hard to model precisely in MC and hence might bias such a measurement. Therefore, we limit ourselves to only $0.1 < |\eta| < 1.05$, and measure the total reconstruction efficiency as a function of muon p_T in a high-p_T muon rich ensemble in MC. The result can be seen in Fig. 4.14. The loss is measured to be roughly linear over the relevant p_T range, and is estimated to be $(2.7 \pm 0.5)\%$ TeV^{-1} relative to the efficiency at p_T= 45 GeV.

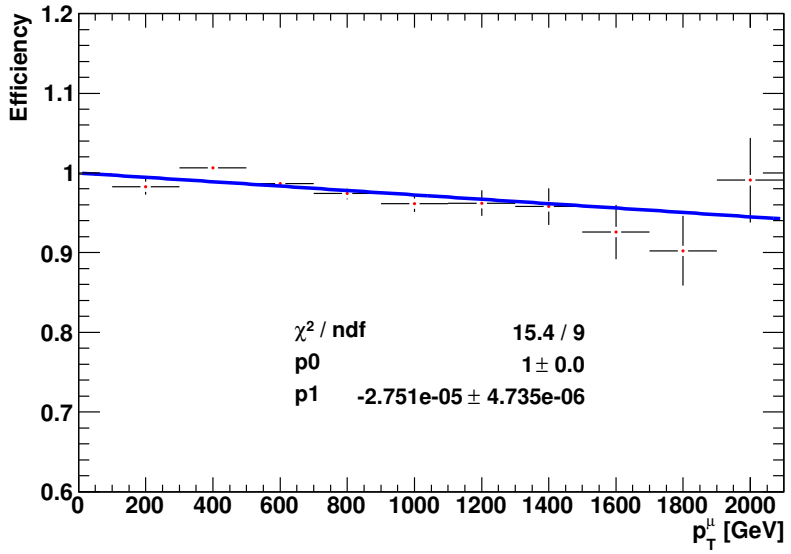

Figure 4.14: Muon reconstruction efficiency as a function of p_T for $0.1 < |\eta| < 1.05$ relative to the muon reconstruction efficiency at p_T= 45 GeV.

To be conservative, the scale factor discussed in section 4.7.3 is assigned an additional uncertainty equal to the efficiency loss measured above. This is parametrized as

$$\Delta\epsilon = 0.000010 m_{W'} \tag{4.9}$$

for the $W' \to \mu\nu$ event selection efficiency and as

$$\Delta\epsilon = 0.000015 m_{Tmin} \tag{4.10}$$

for the $m_T > m_{Tmin}$ background level, where in both cases the mass is measured in GeV.

4.7.5 Muon Trigger Efficiency

The trigger efficiency measurement is also obtained via a Tag&Probe method. Both offline muons are required to pass the selection cuts and the tag is required to match any of the three triggers that are used for the analysis. The probe is investigated to see if it fired any of the triggers listed on Table 4.1 with a $\Delta R < 0.1$ matching criteria. As in the previous cases, the tag and probe are required to have opposite charges, be within the Z mass window of $[75, 105]$ GeV, be back to back by requiring $|\Delta\phi_{\mathrm{tag-probe}}| \geq 2$, and $p_T^{\mathrm{tag-probe}} \leq 65$ GeV. The efficiency is measured to be $(84.5 \pm 0.0)\%$ in MC and $(84.9 \pm 0.1)\%$ in data as summarized in Table 4.11. Figure 4.15 shows the muon trigger efficiency for the offline muon as a function of p_T, η and ϕ. Most of the inefficiency is coming from the feet of the detector which limit the detector coverage. Also the data efficiency is noticeably lower than that of MC in the positive η end of the barrel due to an L1 trigger problem which was present for about half of the data that is considered in this analysis. However, since it is localized to a fairly small area in phase space, it doesn't change the conclusion that MC can successfully regenerate the data performance.

ϵ_{trig}(Data)	ϵ_{trig}(MC)	Ratio
$(84.46 \pm 0.03)\%$	$(84.94 \pm 0.07)\%$	1.006 ± 0.001

Table 4.11: Trigger efficiencies and correction factors for data and MC.

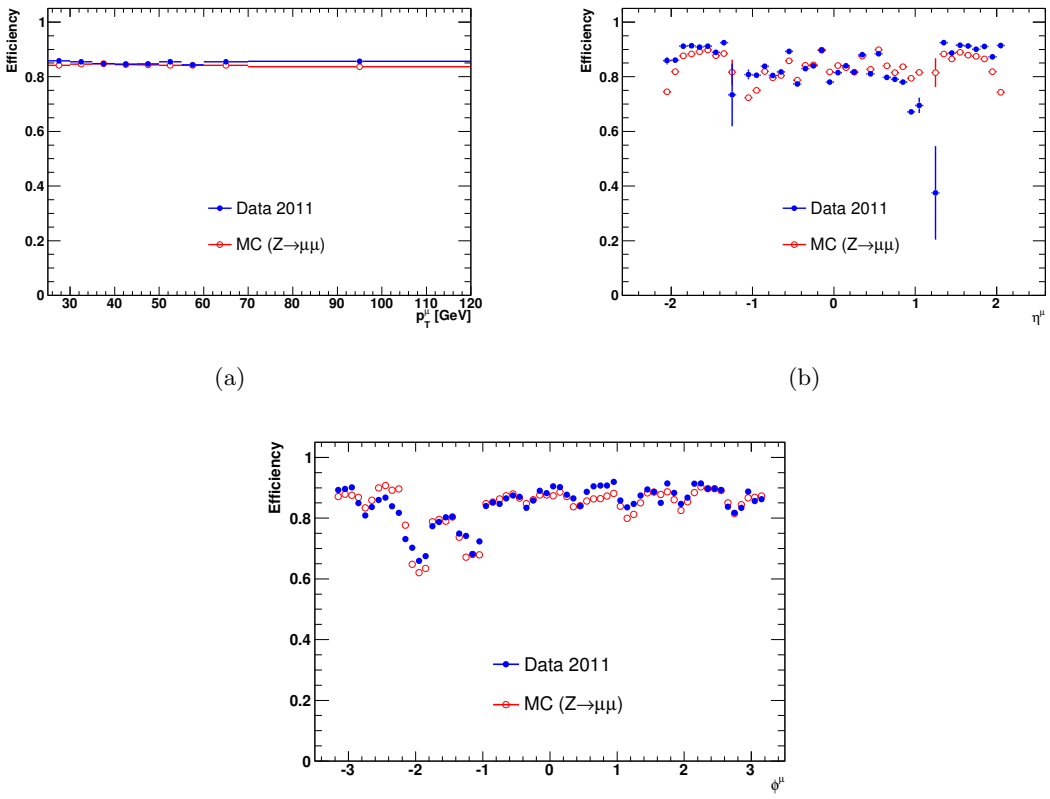

(a) (b)

(c)

Figure 4.15: Muon trigger efficiency as a function of muon p_T, η and ϕ.

As can be seen from the table, the average correction factor obtained with this method is $C^{\mu}_{\text{trig}} = 1.006 \pm 0.001$ where the uncertainty is purely statistical. To estimate the systematic uncertainty the difference in the measurement is determined by varying: a) the matching criteria and b) the mass window. The variation of the measurement due to these changes is $\sim 1\%$, resulting on an overall trigger correction of $C^{\mu}_{\text{trig}} = 1.006 \pm 0.001(\text{stat}) \pm 0.010(\text{sys})$. In order to cover the angular variations and the known L1 problem that affects a substantial part of the data, a flat (and generous) 3% total uncertainty is used for the final calculation.

4.7.6 Muon Momentum Resolution

The understanding of the muon momentum resolution is very important for an analysis like this one as the observable used for the signal search is a function of this variable. Measurements

performed using cosmic rays as well as early collisions show that the resolution in data is worse than the MC simulation used for this analysis. The effect of this is a drop in the signal efficiency as it broadens the W' Jacobian peak and an increase in the background. In order to account for this, the muon momentum is smeared when generating Monte Carlo kinematic distributions and estimating the event selection efficiency and background level.

The deviations in particle trajectories measured by the tracking systems are proportional to the inverse of the momentum and so the intrinsic resolution, i.e. that arising from uncertainties in the position measurements (including alignment), is constant for q/p. Therefore we choose this variable as our smearing parameter. The smearing is performed using Eq. 4.11.

$$q/p = S_0 + [(q/p)_{ini} + S_1 g_1 (q/p)_{ini} + S_2 g_2 sin(\theta)]/S_p, \tag{4.11}$$

where g_1 and g_2 are two random variables chosen from a normal distribution, S_0 is the q/p bias (curvature offset), S_1 is the scale coefficient, S_2 is the intrinsic resolution coefficient, S_p is the momentum scale and θ is the polar angle. The following few section are devoted to the measurement of these parameters, namely S_p,S_1,S_2 and S_0.

4.7.6.1 Muon Momentum Scale

$Z \rightarrow \mu\mu$ events are an excellent sample to measure the muon momentum scaling and smearing performance. Both in data and MC, we choose events with two back to back opposite charge muons, both passing all our selection cuts and coming from the same vertex. Figure 4.16 shows the invariant mass distributions both in data and MC without any extra momentum smearing for the latter. In each case, the unbinned spectrum is fit to a Breit-Wigner whose width is fixed to the natural Z boson width of 2.5 GeV, convoluted with a single Gaussian to mimic the effect of detector resolution and the mean values as well as the standard deviations are quoted on the plots. The asymmetry seen on the distributions are physics motivated and arise from final state radiation. It is possible to obtain better fits using a Crystal Ball type function to account for this effect instead of the Gaussian but this is beyond the scope of this measurement.

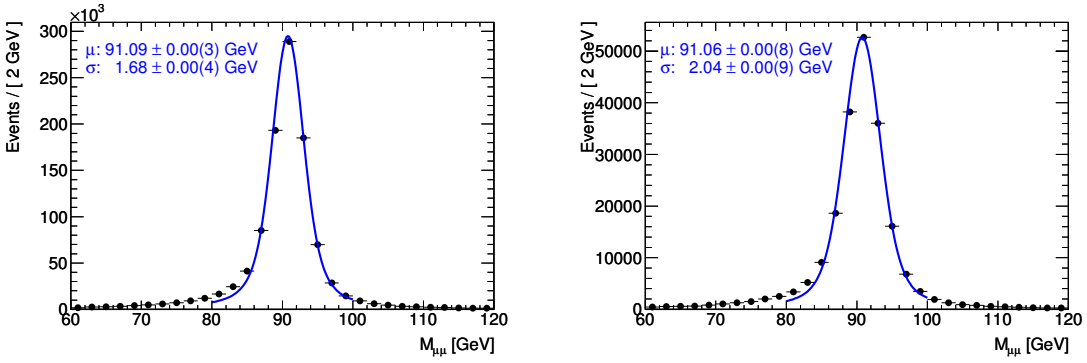

(a) (b)

Figure 4.16: Z peak w/o smearing in MC on left and data on right (filled points). Blue curves are the Gaussian fits in both cases, with the fit parameters given on each plot.

The momentum scale can be measured by directly comparing the mean values of the fits, as they are sensitive to the muon momentum scale. The measured value is 91.09 ± 0.00(stat) GeV in MC, and 91.06 ± 0.01(stat) GeV in data, resulting in a data to MC ratio of $0.999(7) \pm 0.001$(stat). This value is consistent with 1 within its uncertainty, which is also very small. Therefore, no additional correction is applied to the MC for the momentum scale.

Despite the successful simulation of the mean value, the resolution in data, however, is significantly worse than that in MC, as is evident from the widths of the fits. In order to account for this effect, the muon momentum is additionally smeared in the MC to match data, as discussed in the following section.

4.7.6.2 Muon Momentum Smearing

As mentioned in the previous section, the momentum resolution observed in data is worse than that predicted by the MC. We account for this effect by smearing the muon momentum in the MC according to Eq. 4.11. The two relevant coefficients are S_1 and S_2, which are the multiple scattering and intrinsic resolution terms, respectively. The multiple scattering term is more relevant in the low momentum range, whereas the intrinsic resolution dominates the measurement at the high-p_T.

The muon momentum resolution is studied with pp colisions using the di-muon mass distribution in $Z \to \mu\mu$ decays and the comparison of the independent measurements of muons

from $Z \to \mu\mu$ and $W \to \mu\nu$ decays provided by the two tracking systems, the ID and MS, as presented in [43]. These measurements are performed by the Combined Muon Performance (*MCP*) group and mandated to each analysis group within ATLAS. Therefore in this analysis we use those results that are described above and the official tools provided by the MCP group.

As a result, the average momentum resolution for muons used in this analysis is estimated to be around 15% at 1 TeV. This is remarkable in that the design value of 10% is almost reached after only one year of operation. Fig. 4.17 gives the di-muon mass distribution with the extra momentum smearing applied on top of Fig. 4.16a, and as can be seen, it reproduces data, Fig. 4.16b, reasonably well.

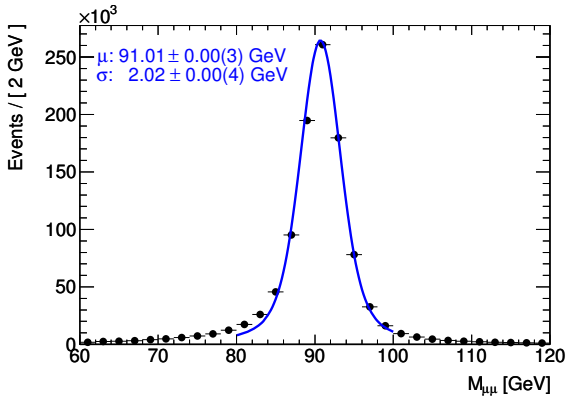

Figure 4.17: Z peak in MC with nominal smearing as mandated by MCP (filled points). Blue curve is the Gaussian fit, with the fit parameters given on the plot.

The tool that is provided by MCP also provides the option to randomly increase or decrease the amount of smearing in the ID or MS by an amount reflecting the uncertainty in the smearing prescription for that system. Fig. 4.18 shows the effect of the baseline and ±1-sigma MCP smearings on the momentum resolution.

The effects of smearing (and thus momentum resolution) uncertainty on this analysis are determined by first evaluating the smearing with the baseline prescription and then with both ID and MS smearing either increased or decreased. The changes in the event selection efficiency and background level are assigned as systematic uncertainties in those parameters, as discussed in section 4.7.9.

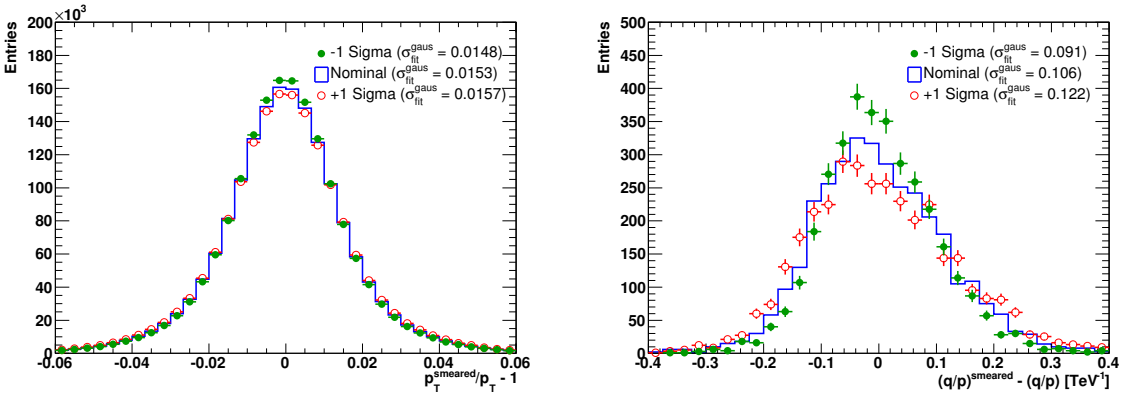

Figure 4.18: Effect of the baseline and ±1-sigma MCP smearings on the momentum resolution in the Monte Carlo. The left plot show the effect in the $W \to \mu\nu$ sample where the multiple scattering term dominates. The right plot shows the effect for $p_T >$ 500 GeV where the measurement term dominates. The integrated luminosity for the data is 0.5 fb^{-1}.

4.7.6.3 Muon Curvature Offset

A possible global curvature offset term, S_0 in Eq. 4.11, that might bias the measurement, is also considered. This effect is studied by the CMP group as well, using the so called toroid-off runs, where the toroidal magnet is turned off to give straight trajectories to the muons within the MS. Prior studies performed with high energy muons from comic rays, as described in [44], were also consulted. These studies conclude that a global curvature offset for the muons is consistent with zero within the measurement error. These studies are verified using Z events and investigate the following asymmetry observable, A:

$$A = \frac{(q/p_T)^{\mu^+} + (q/p_T)^{\mu^-}}{2}. \tag{4.12}$$

A curvature offset will shift the mean of this distribution, which otherwise is expected to be at zero, and will result in a statistically significant asymmetry. The behavior of this observable in data is investigated using the same event selection criteria described in section 4.7.6.1 and the associated distribution is shown in Fig. 4.19. The mean of the distribution is found to be -0.021 ± 0.007 TeV^{-1} for $|A| < 10$ TeV^{-1}.

In light of all the aforementioned studies, $S_0 = 0 \pm 0.035$ TeV^{-1} is used to assess the effect on the signal efficiencies and background levels, and the changes in these observables are

assigned as systematic uncertainties in those parameters in the final calculation, and sumarized in section 4.7.9.

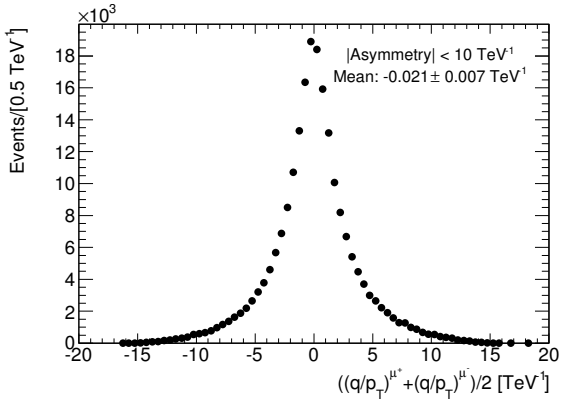

Figure 4.19: Asymmetry distribution in data.

4.7.7 Missing Energy Smearing and Scaling

As discussed in section 4.1, understanding the E_T^{miss} performance is of essence for such a study as this one. In principle E_T^{miss} is a very complicated observable that is strongly correlated to pile-up and the underlying event topology. The MC samples used in this search are the so called *pileup* samples, which means that every event has multiple vertices in addition to the real hard scattering vertex that is of interest. These samples are generated by a statistical combination of the hard scattering events with a random number of events picked from a pool of minimum bias events. The randomness is controlled by the average number of interactions per bunch crossing variable, which is fixed for all the MC samples and shown as the red curve in Fig 4.20. This "guess" was made before the actual data was taken and was therefore designed to span a wide range of possibilities. However, the data distribution, the filled histogram in the same figure, is substantially different than what is in MC. In order to account for this difference, MC events are reweighted using official ATLAS tools, and the result is shown as the green curve in the same figure. This is important for the E_T^{miss} performance because if the MC is not corrected and the higher luminosity profile is kept as is, the E_T^{miss} will be overestimated and will bias the measurement.

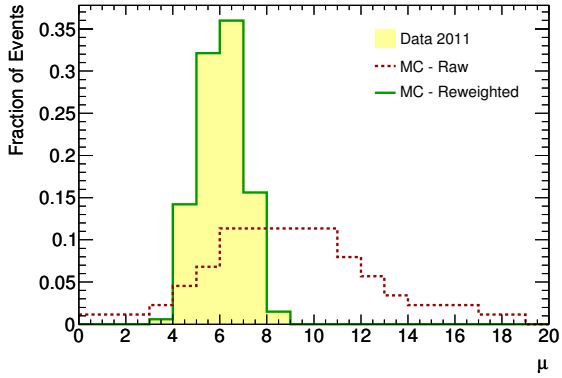

Figure 4.20: Average number of interactions per bunch crossing, μ, in data and MC. The latter is shown before (red) and after (green) reweighting.

It is evident from Eq. 4.2 that there are two distinct components that have to be taken into account while studying the E_T^{miss} systematics. The first is the leptonic part, which comes from the final state muon and is therefore strongly correlated with the measurement of the muon p_T. To properly account for this contribution and the correlation, the E_T^{miss} is varied along with that of the p_T when the latter is varied to study the effect of changing the momentum scale or resolution. Hence, most of the systematic correction and uncertainty arising from the leptonic contribution to the E_T^{miss} is included in the muon momentum systematics.

The second part is the non-leptonic contribution that comes from the calorimetric missing transverse energy measurement. The data vs MC performance of $E_{T,Calo}^{Miss}$ is studied using $Z \to \mu\mu$ events both for resolution and scale. For these studies both muons are required to pass all muon quality cuts, as well as additional event kinematic cuts, as explained in section 4.7.1, to enrich the sample.

Assuming there is no real missing energy in the $Z \to \mu\mu$ events, the perpendicular component to the direction of the di-muon system of the calorimetric missing transverse energy provides a direct handle on the $E_{T,Calo}^{miss}$ resolution. This distribution is shown in Fig. 4.21 both for reweighted MC and data. Fitting both distributions to a Gaussian within $E_{T,Calo\perp}^{Miss} \in [-20, 20]$ GeV yields $\sigma_{MC} = 9.85 \pm 0.02$ GeV and $\sigma_{Data} = 9.57 \pm 0.03$ GeV. The MC reproduces data well, therefore no extra correction factor is applied to the MC for the resolution of the calorimetric transverse missing energy.

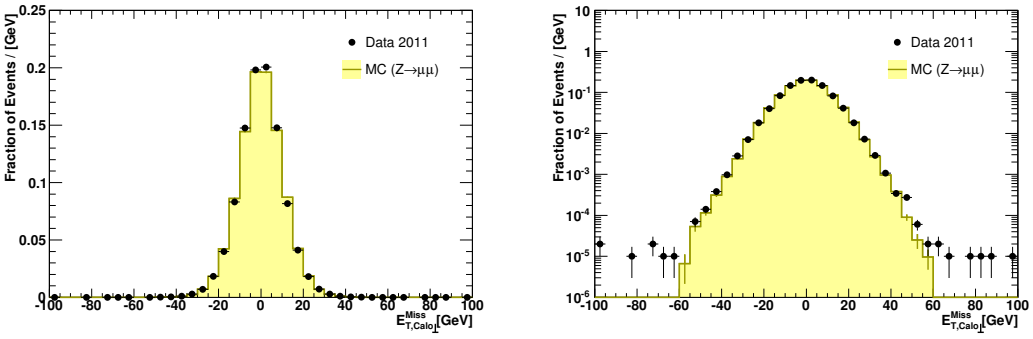

Figure 4.21: Perpendicular component of $E^{Miss}_{T,Calo}$ to the direction of Z. The filled histogram is the reweighted $Z \to \mu\mu$ MC and the circles represent data for the full luminosity. Linear scale is given on left, and log scale on right.

The $E^{miss}_{T,Calo}$ scale is also studied using $Z \to \mu\mu$ events and the component of $E^{miss}_{T,Calo}$ parallel to the direction of the di-muon, which should balance the muon p_T that escapes the calorimeter. The ratio of the E^{miss}_T observed in the calorimeter to the escaping di-muon p_T provides a measure of the E^{miss}_T scale as is demonstrated in Fig. 4.22. The escaping p_T subtracted vectorially from the E_T deposited in the calorimeter. Again the agreement between data and Monte Carlo is good, with only a few percent discrepancy. For this analysis, the systematic uncertainties from the resolution and scale of the non-leptonic E^{miss}_T are estimated to be quite small and are neglected.

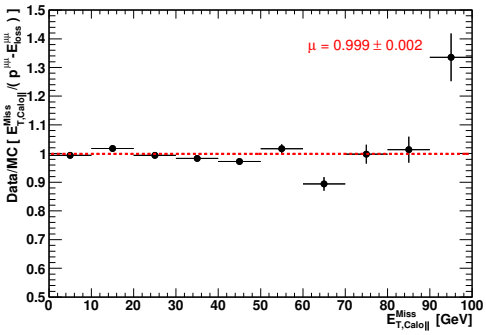

Figure 4.22: The Data/MC ratio of parallel component of $E^{Miss}_{T,Calo}$ to the direction of Z to the transverse momentum of the di-muon system corrected for the muon energy deposition in the calorimeter.

4.7.8 Theory Corrections and Uncertainties

The production of an on-shell W' is suppressed for very large masses by the smallness of the MRST LO* PDFs at large parton momentum fractions as are used for the signal samples considered in this analysis. The effect of this on the invariant mass shapes for different W' mass samples is demonstrated in Fig. 4.23. The shape, in particular the mass-dependence, of the $W' \to \ell\nu$ cross section is corrected to NLO by applying a correction factor, which is also calculated with FEWZ, to the selection efficiencies. Table 4.12 gives the details of the acceptance cuts and presents the correction factors in the last row.

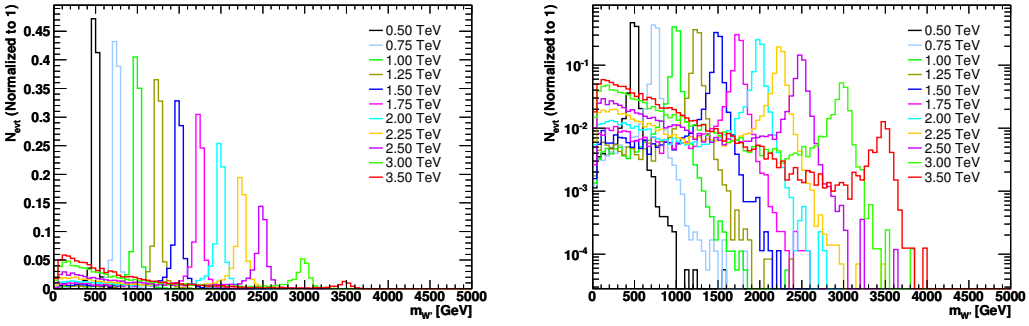

Figure 4.23: Invariant mass shapes of $W' \to \ell\nu$ at generation level. Events are normalized to unity for ease of comparison, linear scale is given on left and log scale on right.

The uncertainty on the W' cross-section is estimated by varying factorization and renormalization scales up and down by a factor of two, using PDF error sets and using the difference between the MSTW PDFs and the CTEQ66 set. These uncertainties were calculated for the 2010 analysis [45], so the same results are used here. The total uncertainty is obtained by adding these in quadrature. This uncertainty can simply be parametrized as a function of $m_{W'}$ as follows:

$$\frac{\sigma(\sigma_{tot})}{\sigma_{tot}} = \begin{cases} 0.07 & m_{W'} \leq 1000 \text{ GeV} \\ 0.07 + 0.000008(m_{W'} - 1000 \text{ GeV}) & m_{W'} > 1000 \text{ GeV} \end{cases} \tag{4.13}$$

Table 4.13 summarizes these uncertainties for all search bins considered in this analysis.

W' mass $[GeV]$	500	600	750	1000	1250	1500	1750	2000	2250	2500
m_{Tmin} $[GeV]$	398	447	562	708	794	891	1000	1122	1122	1122
$W' \to e\nu$ with no kinematic cuts										
$(\sigma B)_{LO}$ [pb]	15.55	7.493	2.931	0.779	0.256	0.0926	0.0362	0.0150	0.00662	0.00314
$(\sigma B)_{NNLO}$ [pb]	17.25	8.270	3.200	0.837	0.261	0.0887	0.0325	0.0126	0.00526	0.00234
$K_{NNLO} = \frac{(\sigma B)_{NNLO}}{(\sigma B)_{LO}}$	1.11	1.10	1.09	1.07	1.02	0.96	0.90	0.84	0.79	0.76
$W' \to e\nu$ with $p_T^e > 25\ GeV$, $\lvert\eta^e\rvert < 2.5$, $p_T^\nu > 25\ GeV$, $m_T > m_{Tmin}$										
$(\sigma B)_{LO}$ [pb]	6.899	3.834	1.466	0.4179	0.1540	0.0574	0.02151	0.0083	0.00351	0.001439
$(\sigma B)_{NNLO}$ [pb]	8.200	4.479	1.679	0.4688	0.1625	0.0575	0.02017	0.0072	0.00269	0.000983
$K_{fid} = \frac{(\sigma B)_{NNLO}}{(\sigma B)_{LO}}$	1.19	1.17	1.15	1.12	1.06	1.00	0.94	0.86	0.77	0.68
W' event selection efficiency correction factor.										
K_{fid}/K_{NNLO}	1.071	1.062	1.050	1.048	1.034	1.042	1.044	1.024	0.975	0.895

Table 4.12: Values for σB for several W' mass points obtained with Pythia (LO) and FEWZ (NNLO) using the central value of the MSTW2008 NNLO PDF. Values are calculated without any kinematic cuts and with kinematic cuts listed below. The last row gives the correction factors for the event selection efficiencies.

W' [GeV]	Scale	Error	Choice	Total	Param
500	1.8%	6.9%	2.0%	7.4%	7.0%
750	2.2%	4.7%	2.8%	5.9%	7.0%
1000	2.1%	6.1%	3.0%	7.1%	7.0%
1250	2.0%	8.0%	2.1%	8.5%	9.0%
1500	3.1%	10.8%	0.2%	11.2%	11.0%
1750	3.5%	12.8%	0.4%	13.3%	13.0%
2000	3.4%	14.7%	3.0%	15.4%	15.0%
2500	4.4%	14.9%	10.0%	18.5%	19.0%

Table 4.13: $W' \to \ell\nu$ cross section uncertainties. The first column is the W' mass and the next three show the uncertainties arising from scale variation, PDF error sets and choice of PDF set. The next column shows the total uncertainty obtained adding these in quadrature. The final column shows the uncertainty obtained with the parametrization in Eq. 4.13.

As discussed in section 4.3, SM W/Z backgrounds are corrected to NNLO using mass dependent k-factors. In principal, the uncertainties in Table 4.13 are also applicable to $W \to \ell\nu$ $d\sigma/d\mathrm{m_T}$. However, it is the integral of this differential cross section over $\mathrm{m_T} > \mathrm{m_{Tmin}}$ that defines the background level. This integral can be estimated by parametrizing the differential cross section as:

$$d\sigma/d\mathrm{m_T} = C\,{\mathrm{m_T}}^{-a} \tag{4.14}$$

with C only weakly dependent on $\mathrm{m_T}$ for the appropriate choice of a. If one chooses $a = 4$, neglects the $\mathrm{m_T}$-dependence, and replaces σ with $d\sigma/d\mathrm{m_T}$ in Eq. 4.13, the integral of this expression using Eq. 4.14 yields:

$$\frac{\sigma(\mathrm{N_{bg}})}{\mathrm{N_{bg}}} = \begin{cases} 0.07 + 0.04 \times 10^{-12}\,{\mathrm{m_{Tmin}}}^4 & \mathrm{m_{Tmin}} \leq 1000\ \mathrm{GeV} \\ -0.01 + 0.12 \times 10^{-3}\,\mathrm{m_{Tmin}} & \mathrm{m_{Tmin}} > 1000\ \mathrm{GeV} \end{cases} \tag{4.15}$$

Table 4.14 shows the resulting uncertainties for the m_T thresholds relevant to this analysis, which is applied to the sum of EW contributions ($W \to \ell\nu$, $Z \to \ell\ell$ and diboson). The total cross section uncertainty (9.5%) is used for the $t\bar{t}$ contribution to the background.

m_{Tmin} [GeV]	$\sigma(N_{bg})/N_{bg}$
398	7.1%
447	7.2%
562	7.4%
708	8.0%
794	8.6%
891	9.5%
1000	11.0%
1122	12.5%

Table 4.14: Background level uncertainties calculated as described in the text.

4.7.9 Summary of Systematic Uncertainties

Various different sources of systematic uncertainties are discussed through sections 4.7.1 to 4.7.7. Only that result in the largest deviations on the signal selection efficiencies and the background levels are considered for the final calculation. The exprimental uncertainties can be summarized as:

- **Selection efficiency:** As discussed from sections 4.7.1 to 4.7.4, the selection efficiency includes the combined muon efficiency, inner detector muon efficiency, muon hit efficiency and isolation efficiency, all of which are measured with Tag&Probe. For each search bin, the high-$p_T$degradation of the reconstruction efficiency is taken into account as discussed in section 4.7.4.

- **Trigger efficiency:** The trigger efficiency is also measured using a Tag&Probe method as discussed in section 4.7.5. Instead of applying an event-by-event correction factor, a flat correction is applied to account for this effect.

- **Momentum resolution and curvature offset:** These sources are discussed in sections 4.7.6.2 and 4.7.6.3, respectively. The baseline numbers are obtained using the nominal values, and the variations are estimated by running the full analysis with $\pm 1\sigma$ errors on each source. Then for each search bin the highest absolute deviation is used as the systematic uncertainty.

In addition to these, the uncertainties due to MC statistics as well as the theory are also taken into account. All these are summarized in Tables 4.15 and 4.16. The former gives the uncertainties on the signal selection efficiencies and the latter on the background levels.

		$m_{W'}$, m_{Tmin} $[GeV]$									
		500	600	750	1000	1250	1500	1750	2000	2250	2500
Source	Section	398	447	562	708	794	891	1000	1000	1000	1122
Selection efficiency	4.7.3 - 4.7.4	2.1%	2.1%	2.1%	2.2%	2.4%	2.5%	2.7%	2.8%	3.0%	3.2%
Trigger efficiency	4.7.5	3.0%	3.0%	3.0%	3.0%	3.0%	3.0%	3.0%	3.0%	3.0%	3.0%
Momentum resolution	4.7.6.2	2.4%	1.4%	1.9%	1.6%	1.3%	2.3%	1.0%	1.7%	2.2%	3.3%
Curvature offset	4.7.6.3	1.4%	0.7%	0.9%	1.6%	1.0%	1.3%	1.1%	1.3%	0.8%	0.8%
All experimental		4.6%	4.0%	4.2%	4.4%	4.2%	4.7%	4.3%	4.6%	4.9%	5.5%
MC statistics	4.6	2.6%	2.7%	2.4%	2.3%	2.7%	3.1%	3.2%	3.3%	2.6%	3.7%
NNLO	4.7.8	3.0%	3.0%	3.0%	3.0%	3.0%	3.0%	3.0%	3.0%	3.0%	3.0%
All		6.0%	5.6%	5.7%	5.7%	5.8%	6.3%	6.1%	6.4%	6.3%	7.5%

Table 4.15: $W' \to \mu\nu$ event selection efficiency uncertainties.

		m_{Tmin} $[GeV]$							
Source	Section	398	447	562	708	794	891	1000	1122
Selection efficiency	4.7.3 - 4.7.4	2.1%	2.1%	2.2%	2.3%	2.3%	2.4%	2.5%	2.6%
Trigger effficiency	4.7.5	3.0%	3.0%	3.0%	3.0%	3.0%	3.0%	3.0%	3.0%
Momentum resolution	4.7.6.2	2.6%	4.2%	0.2%	1.9%	0.9%	0.6%	1.7%	2.3%
Curvature offset	4.7.6.3	2.3%	4.2%	1.9%	2.9%	2.4%	3.0%	4.5%	4.1%
All experimental		5.0%	7.0%	4.2%	5.1%	4.6%	4.9%	6.2%	6.2%
MC statistics	4.6	6.1%	5.9%	4.5%	5.3%	7.1%	9.9%	11.4%	15.0%
EW cross section	4.7.8	6.5%	6.6%	7.3%	8.0%	8.6%	9.5%	11.0%	12.5%
$t\bar{t}$ cross section	4.7.8	0.8%	0.7%	0.2%	0.0%	0.0%	0.0%	0.0%	0.0%
All		10.3%	11.3%	9.5%	10.9%	12.0%	14.6%	17.0%	20.5%

Table 4.16: Background level uncertainties.

4.8 Limit Inputs

Table 4.17 summarizes the inputs to the final limit calculation. The first two columns are the W' mass, and the m_T threshold. The next two are the corrected signal selection efficiency, ϵ_{sig}, and the prediction for the number of signal events, N_{sig}, obtained with this efficiency. The last two columns are the expected number of background events, N_{bg}, and the number of events observed in data, N_{obs}. The uncertainties for N_{sig} and N_{bg} include contributions from the uncertainties in the cross sections but not from the integrated luminosity as this will be accounted for separately. All corrections are applied.

$m_{W'}$ [GeV]	$m_{T\text{min}}$ [GeV]	ϵ_{sig}	N_{sig}	N_{bg}	N_{obs}
500	398	0.252 ± 0.015	4500 ± 430	63.7 ± 6.5	91
600	447	0.286 ± 0.016	2450 ± 220	41.8 ± 4.7	57
750	562	0.293 ± 0.017	970 ± 79	14.3 ± 1.4	20
1000	708	0.326 ± 0.019	282 ± 26	4.98 ± 0.54	4
1250	794	0.367 ± 0.021	99.1 ± 10.2	2.87 ± 0.34	3
1500	891	0.374 ± 0.024	34.4 ± 4.4	1.57 ± 0.23	2
1750	1000	0.338 ± 0.020	11.4 ± 1.7	0.82 ± 0.14	1
2000	1122	0.323 ± 0.021	4.21 ± 0.70	0.440 ± 0.090	1
2250	1122	0.288 ± 0.018	1.97 ± 0.36	0.440 ± 0.090	1
2500	1122	0.221 ± 0.017	0.53 ± 0.11	0.440 ± 0.090	1

Table 4.17: Inputs for the $W' \to \mu\nu$ σB limit calculations.

4.9 Discovery Significance and Limit Calculation

Given Table 4.17, the first question that needs to be answered is the consistency of the observation with the background expectation. For example, in the lowest mass bin, namely $m_T > 398$ GeV, the total expected background is about 64 events, whereas the observation is 91. In order to answer this question from a statistical point of view, a Bayesian approach is adopted.

According to Bayes theorem, one can express the signal strength probability at the value σB, production cross section times branching ratio, as:

$$\mathrm{P_{post}}(\sigma\mathrm{B}) = \mathrm{N} \times \mathcal{L}_{\mathrm{B}}(\sigma\mathrm{B}) \times \mathrm{P_{prior}}(\sigma\mathrm{B}), \tag{4.16}$$

where $\mathcal{L}_{\mathrm{B}}(\sigma\mathrm{B})$ is the likelihood integrated over nuisance parameters, $\mathrm{P_{prior}}(\sigma\mathrm{B})$ is the prior probability and $\mathrm{P_{post}}(\sigma\mathrm{B})$ is the posterior probability and N is the normalization factor that ensures the unitarity of $\mathrm{P_{post}}(\sigma\mathrm{B})$. Now let's look at these in detail.

Using the Poisson statistics, one can define the likelihood as:

$$\mathcal{L}(\sigma\mathrm{B}) = \frac{(\mathrm{L_{tot}} \times \sigma\mathrm{B} \times \epsilon_{\mathrm{sig}} + \mathrm{N_{bg}})^{\mathrm{N_{obs}}}}{\mathrm{N_{obs}}!} \mathrm{e}^{-\mathrm{L_{tot}} \times \sigma\mathrm{B} \times \epsilon_{\mathrm{sig}} + \mathrm{N_{bg}}}, \tag{4.17}$$

which describes the the probability of observing $\mathrm{N_{obs}}$ events given the expectation is:

$$\mathrm{N_{exp}} = \mathrm{N_{sig}} + \mathrm{N_{bg}} = \mathrm{L_{tot}} \times \sigma\mathrm{B} \times \epsilon_{\mathrm{sig}} + \mathrm{N_{bg}}. \tag{4.18}$$

In the last two equations, $\mathrm{L_{tot}}$ is the total integrated luminosity in data, ϵ_{sig} is the signal selection efficiency obtained from MC, and the $\mathrm{N_{bg}}$ is the total number expected background events. These three variables characterize the likelihood defined in Eq. 4.17 and the uncertainties in them can be included by multiplying Eq. 4.17 with the probability density functions (*p.d.f.*) characterizing any particular uncertainty as:

$$\mathcal{L}(\sigma\mathrm{B}, \theta_1, ..., \theta_{\mathrm{N}}) = \mathrm{L}(\sigma\mathrm{B}) \prod g_i(\theta_{\mathrm{i}}), \quad \mathrm{i} \in [1, ..., \mathrm{N}], \tag{4.19}$$

where $\theta_1 ... \theta_N$ are N nuisance parameters and $g_i(\theta_i)$ is the p.d.f. for the parameter θ_i. For convenience, a Gaussian form is assumed for the pdfs, i.e.:

$$g_i(\theta_i) = \frac{1}{\sqrt{2\pi}\sigma_i} e^{-\frac{(\theta_i - \hat{\theta}_i)^2}{2\sigma_i^2}} \tag{4.20}$$

where $\hat{\theta}_i$ is the central value for parameter θ_i and σ_i is the uncertainty assigned to that value. Then one can obtain $\mathcal{L}_{\mathrm{B}}(\sigma\mathrm{B})$ as:

$$\mathcal{L}_{\mathrm{B}}(\sigma\mathrm{B}) = \int \mathrm{d}\theta_1 ... \mathrm{d}\theta_{\mathrm{N}} \mathcal{L}(\sigma\mathrm{B}, \theta_1, ..., \theta_{\mathrm{N}}) \tag{4.21}$$

Using the input values provided in Table 4.17, and choosing an appropriate prior probability, it's possible to numerically calculate the posterior probability rather easily. For this analysis a prior that is flat in σB is used, which is widely used in these type of searches in high energy physics. The posterior probabilities as a function of σB for two mass points, namely $m_{W'} = 500$ GeV and 1000 GeV, are given in Fig. 4.24.

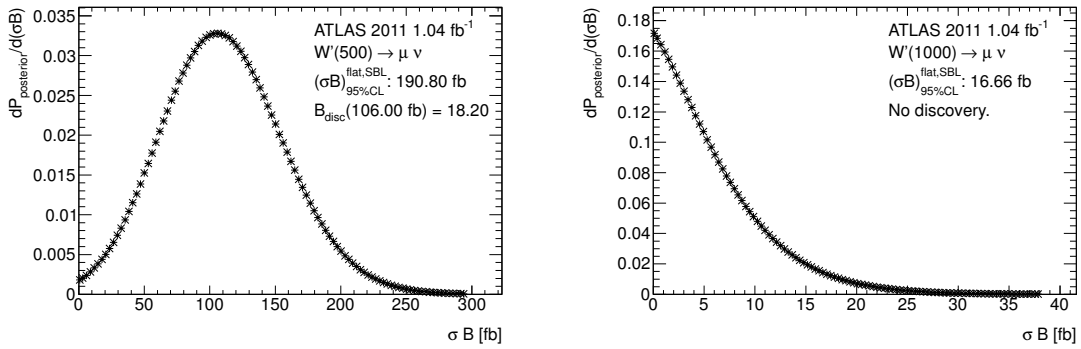

(a) $m_{W'} = 500$ GeV (b) $m_{W'} = 1$ TeV

Figure 4.24: Posterior probabilities for two mass points.

An interpretation of these distributions can be made in the following manner. If the posterior probability peaks at $\sigma\mathrm{B} = 0$ fb, then there is no statistically significant excess in the observation that hints at the possible existence of a signal, hence no discovery. This is the case in Fig. 4.24b, the posterior probability distribution for $m_{W'} = 1$ TeV. But if it peaks at any non-zero value, as in Fig. 4.24a - the posterior probability distribution for $m_{W'} = 500$ GeV, this might be interpreted in two ways: either an upward fluctuation in the background or existence of signal. In order to test this, the following test statistic is used:

$$\mathrm{B_{disc}} = \max(\mathrm{P_{post}})/\mathrm{P_{post}}(0). \tag{4.22}$$

The next step is to generate many $\mathrm{B_{disc}}$ values for background only to obtain a distribution that can be used to compare the observed $\mathrm{B_{disc}}$ value against. This distribution for the $m_{W'} =$ 500 GeV mass point is given in Fig. 4.25. The usual comparison with a Gaussian distribution is made so that a p-value at or below 0.00135 is 3σ evidence of the signal and a p-value at or below 2.9×10^{-7} constitutes a 5σ discovery. As can be seen from Figures 4.24a and 4.25, the

observed $B_{disc} = 18.20$ falls between the 2σ and 3σ thresholds.

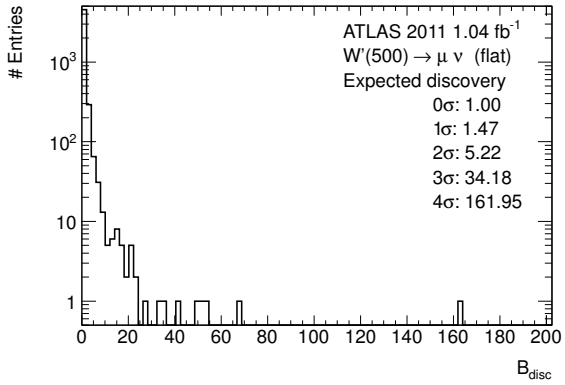

Figure 4.25: B_{disc} distribution for background only for $m_{W'} = 500$ GeV mass point.

This procedure is carried out for all the mass points, and only $m_{W'} = 500$ GeV is found to exceed 2σ, but since it is still lower than 3σ, the observation is said to be statistically consistent with background expectations. Therefore, limits are set on σB for SSM W'.

Given that posterior probabilities are obtained, all one needs to do to get the one-sided σB limits at 95% CL is to calculate the integral in Eq. 4.23 to get the value of σB that gives $CL_{Bayes} = 0.95$.

$$CL_{Bayes} = \int_0^{\sigma B} P_{post}(\xi) d\xi \tag{4.23}$$

For the integration, uncertainties on the signal event selection efficiency and the expected number of background events (excluding the contributions from the integrated luminosity) are handled as uncorrelated nuisance parameters. This is not fully justified, even without the luminosity, since the signal and background uncertainties have common systematic sources. However, there is some cancellation, e.g. efficiency leads to a positive correlation while resolution gives a negative value, and the small size of the signal uncertainties implies the residual correlations are small compared to that from the integrated luminosity. The integrated luminosity is treated as a nuisance parameter with full correlation between signal and background. Fig. 4.26 and Table 4.18 summarize the σB limits obtained as described above.

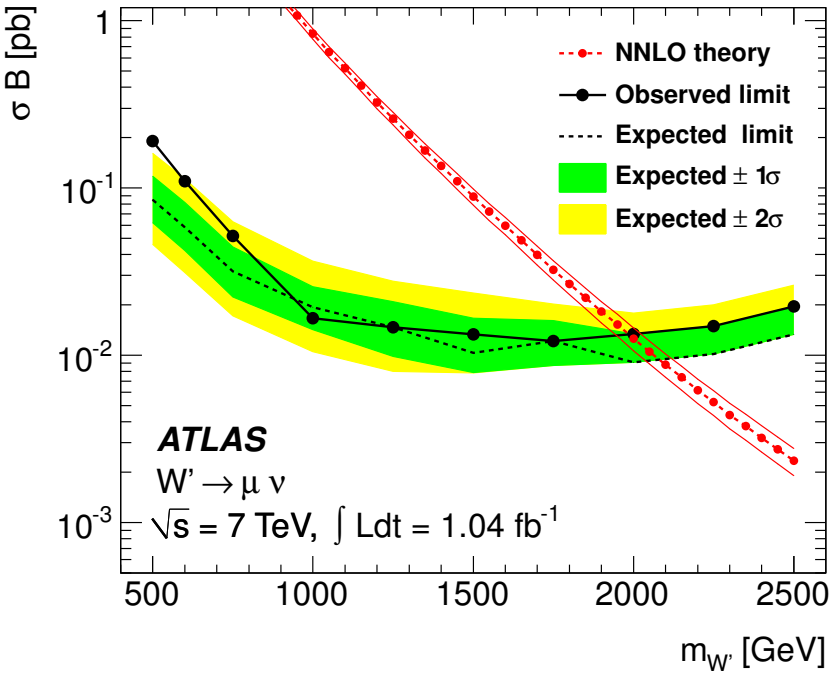

Figure 4.26: Expected and observed limits on σB for $W' \to \mu\nu$. The NNLO calculated cross section and its uncertainty are also shown.

$m_{W'}$	95% CL limit on σB [fb]			
[GeV]	none	S	SB	SBL
500	171.1	173.9	186.0	190.8
600	99.0	100.3	107.6	110.0
750	49.2	49.8	50.9	51.7
1000	16.1	16.3	16.5	16.7
1250	14.4	14.5	14.6	14.7
1500	13.0	13.2	13.2	13.3
1750	12.0	12.1	12.1	12.2
2000	13.2	13.3	13.3	13.4
2250	14.8	14.9	14.9	15.0
2500	19.2	19.5	19.6	19.7

Table 4.18: Bayesian Upper limits on $W' \to \mu\nu$ σB. The first column is the W' mass and the following are the 95% CL limits with headers indicating the nuisance parameters for which uncertainties are included: S for the event selection efficiency (ϵ_{sig}), B for the background level (N_{bg}), and L for the integrated luminosity (L_{int}). The column labeled SBL includes all uncertainties and is used to evaluate mass limits.

The expected and observed lower mass limits in the muon channel are obtained from Fig. 4.26, where the associated curves cut the median NNLO theory cross section. The observed mass limit is found to be 1.98 TeV with the expected limit of 2.08 TeV.

4.10 Combination of Limits with the Electron Channel

It is possible to further extend these limits by combining the results obtained above with an orthogonal channel, in this case $W' \to e\nu$. An identical search is performed in the electron channel, where events are required to pass a set of quality cuts to ensure good background rejection yet high signal selection efficiencies. Here only the results obtained in this channel will be used, however the details of the analysis can be found in [48]. The kinematical distributions after all cuts are shown in Fig. 4.27. The one that is particularly interesting, m_T, shows good data/MC agreement, without any hint for a possible signal, as in the muon channel. The highest-m_T electron event observed in data has m_T= 1334 GeV and the event display is given in Fig. C.1. Table 4.19 summarizes the limit inputs for the electron channel, which is equivalent to Table 4.17 that was discussed and explained in section 4.8 for muons.

$m_{W'}$ [GeV]	m_{Tmin} [GeV]	ϵ_{sig}	N_{sig}	N_{bg}	N_{obs}
500	398	0.388 ± 0.019	6930 ± 620	101.9 ± 10.8	121
600	447	0.456 ± 0.022	3910 ± 330	62.1 ± 7.1	69
750	562	0.429 ± 0.020	1420 ± 110	20.7 ± 3.7	20
1000	708	0.482 ± 0.022	417 ± 35	6.13 ± 0.92	4
1250	794	0.527 ± 0.024	143 ± 14	3.09 ± 0.49	3
1500	891	0.541 ± 0.026	49.6 ± 6.0	1.75 ± 0.32	2
1750	1000	0.515 ± 0.024	17.3 ± 2.4	0.89 ± 0.20	1
2000	1122	0.472 ± 0.023	6.16 ± 0.99	0.48 ± 0.10	1
2250	1122	0.415 ± 0.019	2.84 ± 0.50	0.48 ± 0.10	1
2500	1122	0.333 ± 0.018	0.81 ± 0.16	0.48 ± 0.10	1

Table 4.19: Inputs for the $W' \to e\nu$ σB limit calculations.

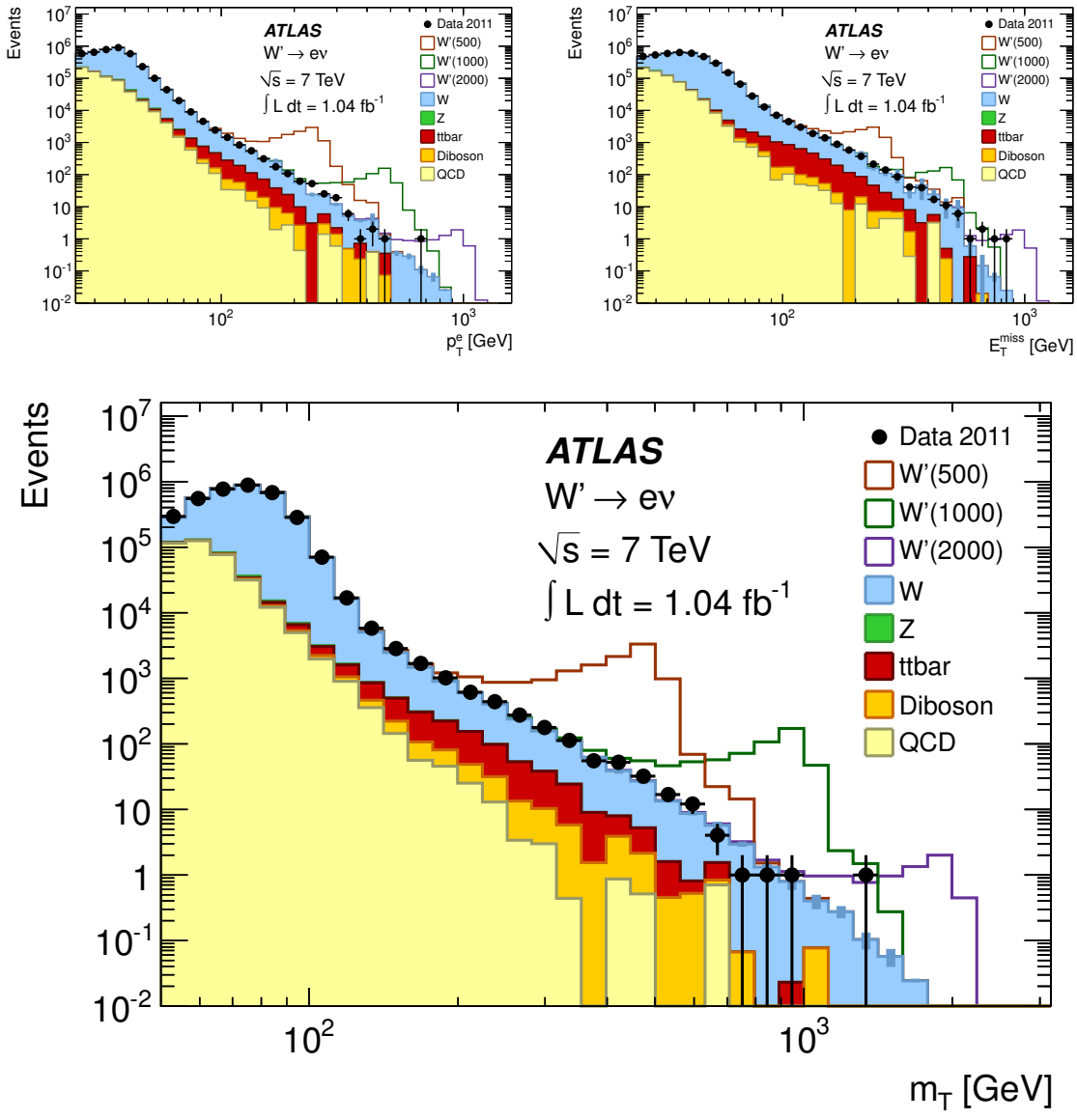

Figure 4.27: Spectra of p_T (top left), E_T^{miss} (top right) and m_T (bottom) for the electron channel after event selection. The points represent data and the filled histograms show the stacked backgrounds. Open histograms are $W' \to e\nu$ signals added to the background with masses in GeV indicated in parentheses in the legend. The QCD backgrounds estimated from data are also shown. The signal and other background samples are normalized using the integrated luminosity of the data and the NNLO (approximate-NNLO for $t\bar{t}$) cross sections listed in Table A.2.

Individual electron limits are calculated in an identical manner to the muon channel, which was discussed in section 4.9. Fig. 4.28 and Table 4.20 summarize the σB limits obtained in the electron channel.

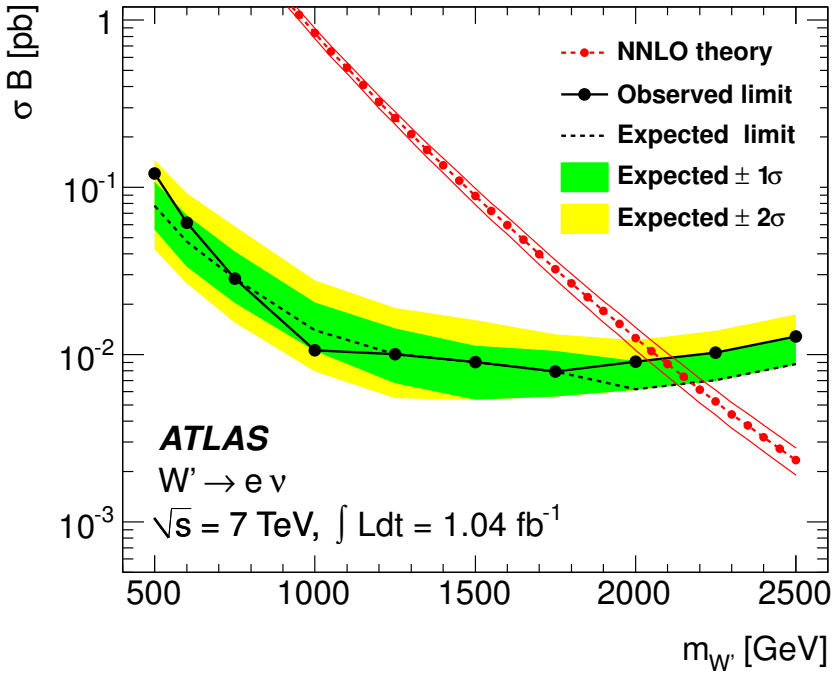

Figure 4.28: Expected and observed limits on σB for $W' \to e\nu$. The NNLO calculated cross section and its uncertainty are also shown.

The expected and observed lower mass limits are again obtained from Fig. 4.28, where the associated curves cut the median NNLO theory cross section. The observed mass limit in the electron channel is found to be 2.08 TeV with the expected limit of 2.17 TeV. As can be seen these limits are more stringent than the muon channel, due primarily to better energy resolution and relatively higher acceptance.

The measurements in the two decay channels, electron and muon, are combined assuming the same branching fraction for each. Equation (4.21) remains valid with the Poisson likelihood replaced by the product of the Poisson likelihoods for the two channels. The electron and muon integrated luminosity measurements are taken to be fully correlated. The selection efficiencies are uncorrelated and the background levels are partly correlated, including only

$m_{W'}$	95% CL limit on σB [fb]			
[GeV]	none	S	SB	SBL
500	97.1	98.0	117.0	121.2
600	48.9	49.2	59.3	61.1
750	23.0	23.1	28.1	28.5
1000	10.1	10.2	10.5	10.6
1250	9.8	9.9	10.0	10.1
1500	7.5	7.7	7.8	7.8
1750	7.8	7.9	7.9	7.9
2000	8.9	9.0	9.0	9.1
2250	10.2	10.2	10.3	10.3
2500	12.7	12.8	12.8	12.9

Table 4.20: Bayesian Upper limits on $W' \to e\nu$ σB. The first column is the W' mass and the following are the 95% CL limits with headers indicating the nuisance parameters for which uncertainties are included: S for the event selection efficiency (ϵ_{sig}), B for the background level (N_{bg}), and L for the integrated luminosity (L_{int}). The column labeled SBL includes all uncertainties and is used to evaluate mass limits.

the full correlation between the cross section uncertainties in the two channels. The effect of this correlation is small: if it is not included, the observed σB limits for the lowest mass points improve by 2% and those for the high-mass points are unchanged. Fig. 4.29 and Table 4.21 summarize the σB limits obtained for the combination of electron and muon channels. The observed combined mass limit is found to be 2.15 TeV with an expected limit of 2.23 TeV.

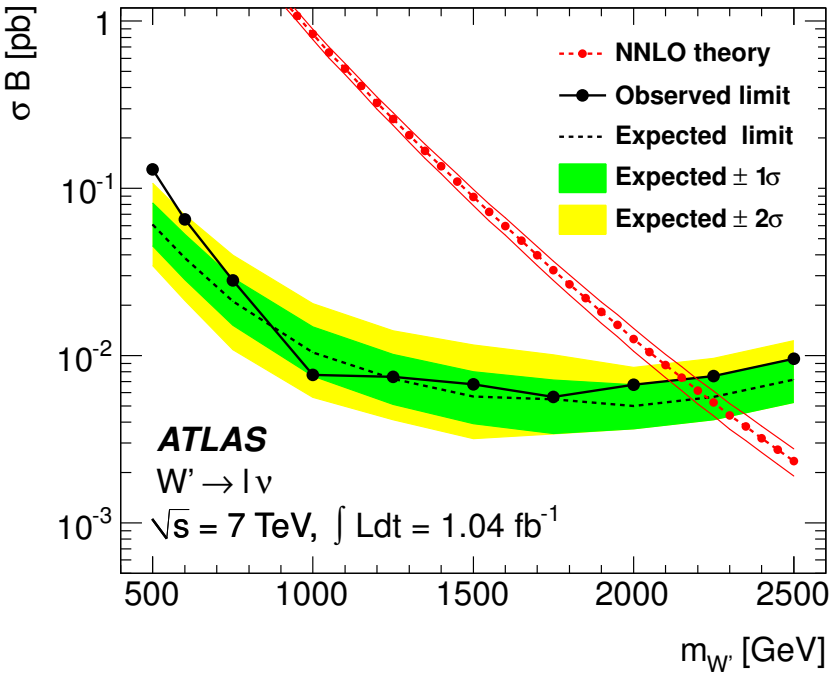

Figure 4.29: Expected and observed limits on σB for $W' \to \ell\nu$. The NNLO calculated cross section and its uncertainty are also shown.

$m_{W'}$	95% CL limit on σB [fb]					
[GeV]	none	S	SB	SBL	SB_c	SB_cL
500	109.1	109.9	123.9	126.9	126.8	129.8
600	54.6	54.6	62.2	63.7	63.8	65.2
750	23.7	23.8	27.4	27.8	27.8	28.1
1000	7.3	7.3	7.6	7.6	7.6	7.8
1250	7.3	7.3	7.4	7.4	7.4	7.5
1500	5.8	5.9	6.0	6.0	6.0	6.0
1750	5.6	5.6	5.7	5.7	5.7	5.7
2000	6.6	6.7	6.7	6.7	6.7	6.7
2250	7.5	7.5	7.6	7.6	7.6	7.6
2500	9.5	9.6	9.6	9.6	9.6	9.6

Table 4.21: Bayesian Upper limits on $W' \to \ell\nu$ σB. The first column is the W' mass and the following are the 95% CL limits with headers indicating the nuisance parameters for which uncertainties are included: S for the event selection efficiency (ϵ_{sig}), B for the background level (N_{bg}), and L for the integrated luminosity (L_{int}). The column labeled SBL includes all uncertainties and is used to evaluate mass limits. Results are also presented for full correlation of the background cross sections between the two channels (SB_c, SB_cL).

4.11 Conclusions

High-mass states in the muon plus missing transverse momentum final state was searched for in 1 fb^{-1} of pp collisions at $\sqrt{s} = 7$ TeV with the ATLAS detector. These results were then combined with the electron channel results to extend the reach to $W' \to \ell\nu$, where $\ell = e/\mu$. No excess beyond Standard Model background expectations is found, hence the Bayesian upper limits on production cross-section times branching fraction, σB, are set. These limits are then converted to mass limits using the NNLO cross-section of the Sequential Standard Model W' and masses up to 2.15 TeV are excluded at 95% CL with an expectation of 2.23 TeV. Fig. 4.30 shows the normalized cross section limits ($\sigma_{\text{limit}}/\sigma_{\text{SSM}}$) for W' as a function of mass for this measurement and those from CDF, CMS and the previous ATLAS search that have been published at the time of this analysis. The limits presented here provide significant improvement for masses above 600 GeV, and were therefore submitted to Physics Letters B in August 2011 and accepted by the journal in September 2011 [48].

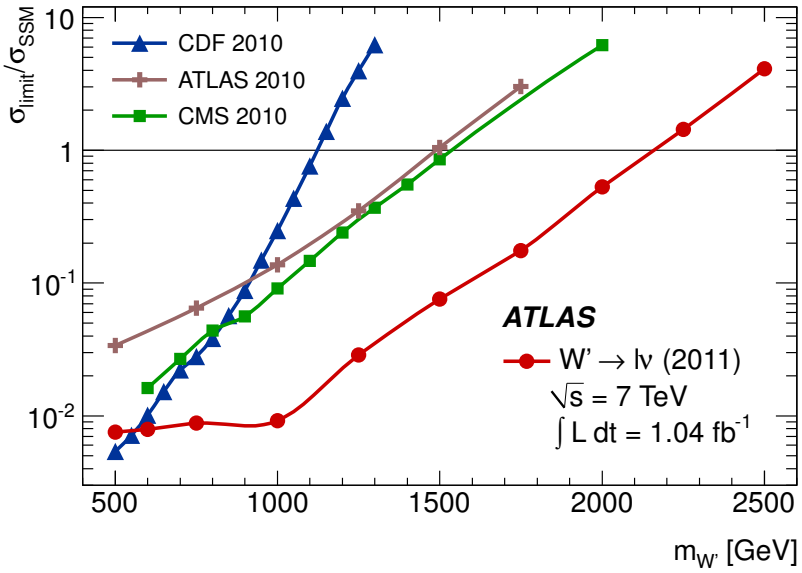

Figure 4.30: Normalized cross section limits ($\sigma_{limit}/\sigma_{SSM}$) for W' as a function of mass for this measurement and those from CDF, CMS and the previous ATLAS search. The cross section calculations assume the W' has the same couplings as the standard model W boson. The region above each curve is excluded at 95% CL.

4.12 Outlook

As mentioned in section 2.3, the analysis presented here is based on 1 fb^{-1} of data collected in March-June 2011. By the end of 2011 the total available luminosity was increased by a factor of five allowing for further reach in m_T for the W' search. Therefore, a natural next step is to add this new data and redo the analysis. Even though this would appear rather easy, it could be quite challenging due to different data taking conditions such as increase in instantaneous luminosity, pile-up etc.

Even though the current analysis is very well established, there are, of course, numerous aspects that can be improved. These include, but are not limited to, development of a model independent search and a more comprehensive search strategy. The prior is a natural path to follow as it will allow theorists to use ATLAS results to test their models in a more straightforward manner. The latter might include the adoption of a template fitting technique for the signal search instead of the current cut and count method. Even though this comes with the price of having to understand the shape systematics more rigorously, a better signal significance would be obtained and hence more stringent limits in the absence of a significant deviation from the background expectation.

All in all, the search for a heavy charged gauge boson will remain one of the benchmark analyses within the ATLAS physics program as it gives us a clean way to test the standard model in the high-p_T regime where the new physics can manifest itself.

APPENDIX A. Signal and Background Monte Carlo Samples

Mass [GeV]	Γ[GeV]	B($W' \to \mu\nu$)	σB [pb] generated	σB [pb] higher order	N_{evt} [k]	L_{int} [pb^{-1}]
500	16.68	0.08520	15.55	17.25	60	1160
600	20.02		7.493	8.270	50	2000
750	25.77	0.08313	2.931	3.200	60	6251
1000	34.75	0.08246	0.7792	0.8366	60	24000
1250	43.70	0.08216	0.2555	0.2606	40	51456
1500	52.65	0.08202	0.09257	0.08870	30	113507
1750	61.60	0.08193	0.03622	0.03246	30	308008
2000	70.55	0.08189	0.01501	0.01260	30	790000
2250	78.75		0.006618	0.005260	50	3200000
2500	88.46	0.08184	0.003142	0.002342	30	4300000

Table A.1: Monte Carlo W' samples used for the study. First column is the mass value of the sample, the second is the simulated W' width, third is the muon channel branching ratio. Forth column gives the generator output for the cross section for the sample, and the column after that is the higher order correction applied to these numbers. The last two columns are the sample size and the total integrated luminosity each sample corresponds to, respectively.

Process	σB [pb] generated	calculated	N_{evt} [k]	L_{int} [pb^{-1}]
W/Z background				
$W \to \mu\nu$	8939	10460	7000	670
$W \to \tau\nu$ ($\lvert\eta_\tau\rvert < 2.8$)	7804	9134	1000	109
$W[\ 200,\ 500] \to \ell\nu$	8.90	10.42	60	5760
$W[\ 500, 1500] \to \ell\nu$	0.242	0.283	60	212000
$W[1500, 2500] \to \ell\nu$	0.00079	0.00092	60	6540000
$W[\ 2500+\ ] \to \ell\nu$	0.0000090	0.0000072	60	830000000
$Z[\ 60+\ ] \to \mu\mu$	856	989	5300	5360
$Z[\ 250,\ 400] \to \mu\mu$	0.416	0.480	20	42000
$Z[\ 400,\ 600] \to \mu\mu$	0.0672	0.0777	20	260000
$Z[\ 600,\ 800] \to \mu\mu$	0.0112	0.0129	20	1550000
$Z[\ 800, 1000] \to \mu\mu$	0.00274	0.0032	20	6300000
$Z[1000, 1250] \to \mu\mu$	0.000918	0.0000	20	21800000
$Z[1250, 1500] \to \mu\mu$	0.000249	0.0000	20	80300000
$Z[1500, 1750] \to \mu\mu$	0.0000769	0.0000	20	260000000
$Z[1750, 2000] \to \mu\mu$	0.0000260	0.0000	20	770000000
Diboson background				
WW	11.49	17.82	250	14000
WZ	3.481	6.07	250	41200
ZZ	0.976	1.387	250	180000
$t\bar{t}$ background				
$t\bar{t} \to \ell X$	80.2	89.4	1000	8650

Table A.2: List of Monte Carlo background samples used for the analysis.

APPENDIX B. List of High-m_T Events in Data

Table B.1: Events passing final selection with $m_T > 398$ GeV for 1.04 fb^{-1}.

Run	LumiBlock	Event	p_T	η	ϕ	d_0	z_0	E_T^{miss}	m_T
178044	164	9886320	192.10	-1.53	-2.18	0.01	-0.30	225.65	416.13
178044	362	34585070	231.05	0.35	1.96	-0.01	-0.11	233.43	464.42
178109	182	4405627	197.23	-1.37	0.18	-0.01	-0.09	207.79	404.80
179804	678	79472072	198.51	-0.23	-0.71	-0.00	0.04	322.49	505.81
179939	322	14478982	403.35	-0.71	-2.66	-0.01	0.01	449.32	851.10
180122	443	37167417	231.08	-0.37	2.76	0.00	0.00	240.77	450.92
180124	526	74068419	218.06	0.43	-0.59	0.00	-0.16	207.06	424.87
180139	173	10051992	292.39	0.32	-2.45	-0.01	0.07	294.89	587.25
180149	86	1386253	252.04	0.18	1.98	0.01	-0.03	162.84	405.17
180149	202	25360846	694.92	0.13	-0.26	0.02	-0.03	679.45	1339.17
180164	843	144514014	195.22	-1.81	-0.22	0.00	-0.01	210.32	405.23
180225	266	50035973	317.43	0.83	0.60	0.01	-0.10	226.34	536.08
180242	216	26294202	281.52	-0.18	-0.36	0.00	-0.09	196.48	470.00
180309	422	68588358	259.48	-0.51	-2.97	-0.01	-0.09	159.35	406.23
180400	437	49367690	260.87	0.61	0.62	0.00	-0.02	255.41	514.30
180400	487	59704798	209.76	0.15	2.11	0.01	-0.10	208.67	418.43
180400	801	117659005	208.64	0.29	1.95	-0.00	0.08	195.58	403.42
180481	496	68971920	203.72	0.04	1.91	0.00	-0.09	224.77	427.98
180636	141	17737928	236.96	0.30	1.15	-0.01	-0.06	215.57	444.69
180636	231	35730995	523.83	-0.84	-1.66	-0.00	0.04	115.08	490.86

Table B.1: Events passing final selection with $m_T > 398$ GeV for 1.04 fb^{-1} (cont.).

Run	LumiBlock	Event	p_T	η	ϕ	d_0	z_0	E_T^{miss}	m_T
180636	868	154077881	301.94	0.52	-2.71	0.00	-0.08	174.34	456.28
182284	612	63150462	388.95	-0.59	0.26	-0.01	-0.08	241.54	598.65
182346	159	11095047	203.77	0.50	1.17	0.00	-0.21	213.73	417.38
182424	199	19644277	240.50	-0.69	2.78	-0.01	-0.06	237.21	475.36
182424	379	61035500	280.53	-1.74	-1.32	0.03	-0.21	280.67	561.17
182424	524	89437409	231.99	-0.70	-2.28	-0.00	0.03	204.23	435.32
182454	393	46350845	201.72	0.61	1.72	0.00	0.05	203.50	401.87
182486	533	90903480	225.38	0.16	0.84	-0.00	-0.12	236.76	461.67
182486	608	108261420	210.68	-0.20	-0.98	-0.00	0.17	197.36	404.29
182486	682	124723696	378.59	1.34	-1.86	0.00	0.13	346.87	724.59
182516	320	10433139	233.53	1.43	-1.96	0.00	0.05	255.56	488.57
182747	182	39664355	222.41	1.51	-2.51	0.00	0.02	199.36	420.80
182747	330	74144949	443.67	0.12	-1.73	0.02	0.09	119.90	460.68
182787	155	8021766	437.49	1.89	2.36	-0.02	0.05	187.86	572.80
182787	319	48159447	261.41	-0.31	-0.48	-0.03	0.51	251.05	512.29
182787	484	82649599	278.09	-1.89	2.37	0.02	-0.35	153.33	412.62
182787	634	120217986	205.52	-0.15	-0.41	-0.00	-0.03	222.82	427.99
182796	256	41598961	697.62	0.12	0.27	-0.01	-0.10	125.90	592.49
182796	351	61441974	318.64	0.77	-0.14	0.00	-0.02	284.98	602.41
182886	50	696103	283.02	-0.89	-2.44	0.00	0.05	312.00	577.20
182886	55	1827995	450.36	-0.64	1.00	-0.00	-0.01	530.72	977.62
183003	369	41337610	148.06	0.06	0.97	0.00	-0.07	294.42	416.20
183003	1041	185635710	299.69	1.34	-1.86	-0.01	0.04	290.48	590.03
183003	1057	188708700	229.27	0.36	-0.40	0.01	-0.08	233.92	463.05
183021	879	70442799	243.21	0.46	-2.99	0.00	-0.06	196.41	435.36
183021	914	79006105	236.11	1.01	2.22	-0.01	-0.09	228.52	464.55

Table B.1: Events passing final selection with $m_T > 398$ GeV for 1.04 fb^{-1} (cont.).

Run	LumiBlock	Event	p_T	η	ϕ	d_0	z_0	E_T^{miss}	m_T
183038	78	3664152	251.11	0.46	2.50	-0.00	-0.18	204.76	453.21
183054	184	17584435	279.89	-0.55	0.96	-0.00	-0.06	276.28	554.88
183054	223	27141250	274.71	-1.03	0.91	-0.01	-0.05	257.25	531.60
183081	788	153880513	245.80	-0.28	-1.42	-0.00	-0.10	209.72	451.59
183081	844	165104609	221.78	0.60	-2.01	0.01	-0.05	230.10	451.74
183130	226	45367479	231.45	0.60	1.41	0.00	-0.01	218.56	448.25
183216	520	110119005	215.96	-0.84	0.07	-0.00	-0.05	195.47	400.13
183216	666	141042097	166.29	0.72	0.50	-0.03	-0.10	245.56	404.09
183286	334	69534093	205.07	0.14	2.67	-0.00	0.11	207.41	412.38
183286	603	131757200	327.84	-0.42	-2.93	-0.01	0.02	306.68	634.17
183347	1001	48520480	246.18	-0.22	-0.15	0.01	-0.02	254.42	488.95
183347	1159	77808865	201.00	-1.60	0.11	0.00	-0.11	207.72	406.95
183391	483	53157721	295.55	-0.78	-0.96	0.01	0.06	307.25	602.57
183407	240	18852204	229.96	-1.73	1.43	-0.01	-0.14	251.21	480.64
183426	91	5790566	207.86	-0.13	1.06	0.00	-0.00	199.37	407.12
183426	161	19236834	216.38	-1.39	0.82	-0.00	0.05	194.90	410.70
183462	457	11222901	264.83	-1.62	2.07	-0.00	-0.22	167.11	419.70
183462	675	52010059	247.68	-0.13	-1.62	0.01	0.01	273.03	518.62
183462	751	66786208	209.42	-0.09	2.82	0.01	0.04	236.07	444.69
183462	854	85048510	140.88	-0.89	-1.66	-0.00	-0.06	295.20	406.75
183462	931	98776243	329.22	0.63	2.06	0.00	-0.10	310.13	636.96
183462	1020	113363684	199.08	1.58	2.42	-0.00	-0.08	206.11	405.12
183544	335	10638729	259.16	-1.57	-1.71	0.01	-0.25	268.88	527.54
183544	363	15588080	274.88	-0.55	1.91	-0.01	0.00	302.85	577.05
183580	309	1557274	252.22	0.68	-1.00	0.00	-0.00	232.26	484.04
183581	240	6207511	308.70	-2.00	0.90	-0.01	-0.17	291.46	599.79

Table B.1: Events passing final selection with $m_T > 398$ GeV for 1.04 fb^{-1} (cont.).

Run	LumiBlock	Event	p_T	η	ϕ	d_0	z_0	E_T^{miss}	m_T
183581	396	35964963	249.27	-0.37	2.96	0.00	-0.03	315.49	560.81
183581	414	39789316	239.06	-1.59	-1.50	0.02	-0.18	237.91	476.73
183581	539	62969282	207.87	-0.19	-2.18	-0.00	0.15	204.75	412.54
183780	476	15932737	252.29	0.69	-0.73	0.02	0.10	240.78	492.94
183780	1117	125756279	188.27	-1.86	-2.52	-0.00	-0.04	215.77	402.81
183780	1119	126008351	236.47	0.26	-0.16	0.01	-0.05	356.88	580.57
183780	1433	175606230	249.21	0.35	-0.53	0.00	-0.06	241.71	485.58
184022	269	9593939	405.10	-1.54	-2.62	0.01	-0.31	131.25	460.94
184022	376	30699822	235.79	0.16	-2.76	0.00	-0.09	194.67	426.35
184022	538	60941166	358.44	0.19	3.06	0.00	0.03	149.40	438.36
184022	541	61577724	353.25	-0.94	-0.15	0.01	-0.07	353.95	707.19
184022	567	67068849	227.40	-0.18	1.89	-0.00	-0.08	227.32	454.54
184022	1007	145038704	324.08	-0.82	2.34	-0.01	0.03	322.82	646.89
184022	1013	146063942	246.67	-0.31	2.38	-0.00	0.03	229.39	475.73
184066	96	1930115	227.60	-0.18	-0.07	-0.00	-0.22	214.05	440.77
184130	252	8446326	210.66	0.55	-2.74	-0.00	0.01	239.51	449.15
184130	755	99604587	296.56	-1.63	0.93	-0.01	-0.08	291.81	588.35
184130	885	123155144	203.33	-0.88	2.26	-0.01	0.02	332.17	517.52
184130	1078	156494408	231.97	0.45	-1.77	-0.00	-0.09	290.78	518.86

APPENDIX C. Highest-m_T Event Display in the Electron Channel

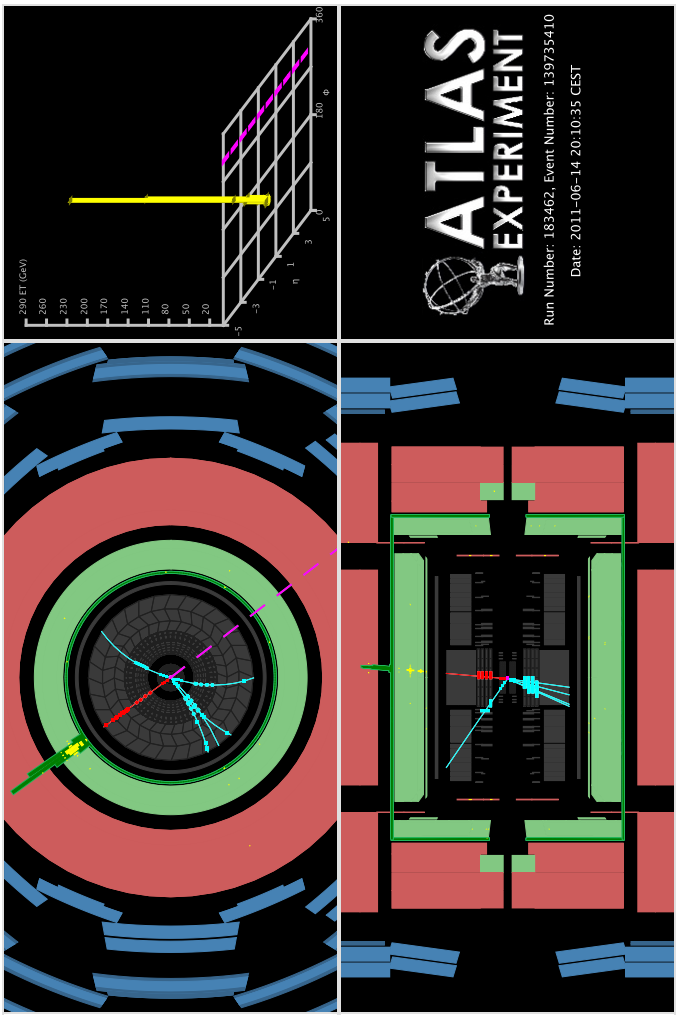

Figure C.1: Highest-m_T event (m_T= 1334 GeV) observed in data for the electron channel. End (top left) and side (top right) views of the event, and an η-ϕ histogram of E_T measured in the calorimeter (top right) are shown. The electron (red) has p_T = 668 GeV and the E_T^{miss} (dashed) is 667 GeV. Inner detector tracks tracks with p_T> 1 GeV are shown. The threshold to display calorimeter energy deposits is E_T > 1 GeV.

BIBLIOGRAPHY

[1] D. J. Griffiths, "Introduction to Elementary Particles", (New York, USA: Wiley, 1987).

[2] I. Newton, "Philosophiæ Naturalis Principia Mathematica", (London: 1687).

[3] A. Einstein, "The basics of general relativity theory", Annalen Der Physik **49**, 769 (1916).

[4] J.C. Maxwell,"On Physical Lines of Force", Philosophical Magazine and Journal of Science **21 & 23**, Series 4, 161 (1861).

[5] E. Fermi, "Radioactivity induced by neutron bombardment", Nature **133**, 757 (1934).

[6] S. L. Glashow, "Partial-Symmetries of weak interactions", Nucl. Phys. **22**, 579 (1961).

[7] S. Weinberg, "A Model of Leptons", Phys. Rev. Lett. **19**, 1264 (1967).

[8] The CDF Collaboration, "Observation of Top Quark Production in $p\bar{p}$ Collisions with the Collider Detector at Fermilab", Phys. Rev. Lett. **74**, 2626 (1995).

[9] The DØ Collaboration, "Observation of the Top Quark", Phys. Rev. Lett. **74**, 2632 (1995).

[10] P. Langacker, R.W. Robinett, J.L. Rosner, "New heavy gauge bosons in pp and $p\bar{p}$ collisions", Phys. Rev. **D30**, 1470 (1984).

[11] B.W. Lee, C. Quigg, H.B. Thacker, " Weak interactions at very high energies: The role of the Higgs-boson mass", Phys. Rev. Lett. **D16**, 1519 (1977).

[12] G. Altarelli, B. Mele, M. Ruiz-Altaba, "Searching for new heavy vector bosons in $p\bar{p}$ colliders", Z. Phys. **C45**, 109 (1989).

[13] L.S. Durkin, P. Langacker, "Neutral-current constraints on heavy Z bosons", Phys. Lett. **B166**, 436 (1986).

[14] H. Georgi, E.E. Jenkins, E.H. Simmons, "Ununifying the standard model", Phys. Rev. Lett. **62**, 2789 (1989).

[15] V. Barger, W.Y. Keung, "Sequential W and Z bosons", Phys. Lett. **B94**, 377 (1980).

[16] CERN (2008). *A global endeavour*. http://public.web.cern.ch/public/en/about/Global-en.html.

[17] CERN (2010). *The Large Hadron Collider*. http://public.web.cern.ch/public/en/lhc/lhc-en.html.

[18] The ATLAS Experiment (2008). *The ATLAS Experiment*. http://atlas.ch/.

[19] The ATLAS Collaboration, "Expected Performance of the ATLAS Experiment - Detector,Trigger and Physics", [arXiv:0901.0512 [hep-ex]].

[20] T. Cornelissen, *et al.*, "Concepts, Design and Implementation of the ATLAS New Tracking (NEWT)", ATL-SOFT-PUB-2007-007 (2007).

[21] The ATLAS Collaboration, "Liquid Argon Calorimeter", Technical Design Report, CERN/LHCC/96-41.

[22] The ATLAS Collaboration, "ATLAS Tile Calorimeter", Technical Design Report, CERN/LHCC/96-42.

[23] The ATLAS Collaboration, "ATLAS Detector and Physics Performance : Technical Design Report", ATLAS TDR 14, CERN/LHCC/99-14.

[24] W. Lampl et al., "Calorimeter Clustering Algorithms: Description and Performance", ATL-LARG-PUB-2008-003 (2008).

[25] The ATLAS Collaboration, G. Aad *et al.*, "Luminosity Determination in pp Collisions at $\sqrt(s) = 7$ TeV Using the ATLAS Detector at the LHC", CERN-PH-EP-2010-069, submitted to EPJC (January 11th 2010).

[26] T.M. Hong, A.S. Mete, J. Stelzer, T. Bold, "Event-loss monitoring for Trigger and DAQ systems", *ATL-COM-DAQ-2011-062*, (2011).

[27] T. Sjostrand, S. Mrenna, and P. Skands, "PYTHIA 6.4 physics and manual", JHEP **05**, 026 (2006).

[28] A. Martin, W. Stirling, R. Thorne, and G. Watt, "Parton distributions for the LHC", Eur. Phys. J. **C63**, (2009) 189285, [arXiv:0901.0002 [hep-ph]].

[29] S. Frixione and B.R. Webber, "Matching NLO QCD computations and parton shower simulations", JHEP **029**, 0206 (2002), [arXiv:0204244 [hep-ph]].

[30] J. M. Butterworth and M. H. Seymour, "Multi-parton interactions in Herwig for the LHC", http://projects.hepforge.org/jimmy, (2007).

[31] G. Corcella, *et al.*, "HERWIG6 : An event generator for hadron emission reactions with interfering gluons (including supersymmetric processes)", JHEP **01**, 010 (2001).

[32] P. M. Nadolsky, *et al.*, "Implications of CTEQ global analysis for collider observables", Phys. Rev. **D78**, (2008).

[33] P. Golonka and Z. Was, "PHOTOS Monte Carlo: A Precision tool for QED corrections in Z and W decays", Eur. Phys. J. **C45** 97107 (2006), [arXiv:0506026 [hep-ph]].

[34] GEANT4 Collaboration, S. Agostinelli *et al.*, "GEANT4: A Simulation toolkit", Nucl. Instr. Meth. **A506**, 250303 (2003).

[35] R. Gavin, Y. Li, F. Petriello *et al.*, "FEWZ 2.0: A code for hadronic Z production at next-to-next-to- leading order", [arXiv:1011.3540 [hep-ph]].

[36] A. Sherstnev and R. S. Thorne, "Parton Distributions for LO Generators", Eur. Phys. J. **C55**, 1287 553-575 (2008).

[37] R. Hamberg, W. L. van Neerven, and T. Matsuura, "A Complete calculation of the order α_s^2 correction to the Drell-Yan K factor", Nucl. Phys. **B359**, 343405 (1991); Erratumibid. **B644**, 403 (2002).

[38] C. Carloni Calame, G. Montagna, O. Nicrosini, and A. Vicini, "Precision electroweak calculation of the charged current Drell-Yan process", JHEP **016**, 0612 (2006), [arXiv:0609170 [hep-ph]].

[39] U. Baur, "Weak boson emission in hadron collider processes", [arXiv:0611241 [hep-ph]].

[40] U. Langenfeld, S. Moch, and P. Uwer, "Measuring the running top-quark mass", Phys. Rev. **D80**, 054009 (2009), [arXiv:0906.5273 [hep-ph]].

[41] S. Hassini, *et al.*, "A muon identification and combined reconstruction procedure for the ATLAS detector at the LHC using the (MUONBOY, STACO, MuTag) reconstruction packages", NIM **A572**, 77-79 (2007).

[42] Th. Lagouri, *et al.*, "A muon identification and combined reconstruction procedure for the ATLAS detector at the LHC at CERN", IEEE Trans. Nucl. Sci. **51**, 3030-3033 (2004).

[43] The ATLAS Collaboration, "ATLAS Muon Momentum Resolution in the First Pass Reconstruction of the 2010 p-p Collision Data at $\sqrt{s} = 7$ TeV", *ATLAS-CONF-2011-047*, (2011).

[44] The ATLAS Collaboration, "Muon momentum resolution from pp collisions", shed, PLHC, 1343 (2010).

[45] The ATLAS Collaboration, "Search for high-mass states with lepton plus missing transverse momentum in proton-proton collisions at $\sqrt{s} = 7$ TeV with the ATLAS detector", Phys. Lett. B **701**, 50 (2011).

[46] https://twiki.cern.ch/twiki/bin/view/AtlasProtected/HowToCleanJets

[47] CDF Collaboration, T. Aaltonen *et al.*,"Search for a New Heavy Gauge Boson W' with Electron + missing ET Event Signature in $p\bar{p}$ collisions at $\sqrt{s} = 1.96$ TeV", Phys. Rev. **D83**, 031102 (2011).

[48] The ATLAS Collaboration, "Search for a heavy gauge boson decaying to a charged lepton and a neutrino in 1 fb^{-1} of pp collisions at $\sqrt{s} = 7$ TeV using the ATLAS detector", Phys. Lett. **B705**, 28 (2011).